Aspects of suspension design for the development of advanced gravitational wave detectors

Rahul Kumar, M.Sc. (Research)
School of Physics and Astronomy
College of Science and Engineering
University of Glasgow

Presented as a thesis for the degree of
Doctor of Philosophy
in the University of Glasgow, University Avenue, Glasgow,
G12 8QQ

June 2013

Contents

List of figures

List of tables

Acknowledgements

It has been a privilege to work in a group full of thoroughly supportive and inspirational people and I would like to take this opportunity to express my gratitude towards them.

Firstly, I would like to express my sincere gratitude to my academic supervisors, Dr. Giles Hammond and Professor Sheila Rowan for giving me this opportunity to work along with them. Their guidance, patience and constant support has been remarkable, without which it would not have been possible to conduct this research. I would like to thank Professor Jim Hough for his guidance and for providing me the opportunity to work in this wonderful group (IGR). I would also like to thank the School of Physics and Astronomy, University of Glasgow for providing me the funding to carry out my PhD research.

I would like to thank Dr. Kirill Tokmakov for being a great colleague and it was a pleasure to work with him. A special thanks goes to Russell Jones for his excellent support in providing Solidworks drawing and other engineering solutions. I would also like to thank Dr. Liam Cunningham, Dr. Alan Cumming and Dr. Angus Bell for providing valuable help every time I needed. I would like to thank Dr. Jamie Scott for providing excellent IT support. Excellent support was also provided by the research group technicians, Colin Craig and Steven Craig and I am thankful for their help. I would also like to thank Dr. Marielle van Veggel, Dr. Ronny Nawrodt, Dr. Alastair Heptonstall and Dr. Iain Martin for their help and support on various aspects of my work. A special thanks goes to Dr. Borja Sorazu for his friendship, our long conversations were always refreshing. I would also like to thank my colleagues in the group, Dr. Matt Abernathy, Dr. Nicola Beveridge, Chris Bell, Dr. Ricardo Bassiri, Dr. Paul Campsie, Kieran Craig, Rebecca Douglas, Keith Evans, Dr. Karen Haughian, Martin Hart, Dr. Peter Murray and Richard Middlemiss.

On a personal front I would like to especially thank my Mum and Dad, and my sister Aditi for their unconditional love and support throughout my education. A special thanks goes to my fiancée Kalyani, whose love and support has been phenomenal. Finally, I would like to thank my friends in Glasgow as well as in India for enriching my life with their companionship.

Preface

This thesis is an account of work carried out in the Institute for Gravitational Research (IGR) at the University of Glasgow, between May 2010 and December 2012, on aspects of suspension design for the development of gravitational wave detectors.

In chapter 1, the introduction to gravitational waves, their sources and production is discussed. The techniques for their detection and the status of the current and future detectors have been described here. The information provided in this chapter has been derived from published literature.

In chapter 2, thermal noise issues and their sources in the gravitational wave detectors are discussed. The methods to estimate the mechanical loss and suspension thermal noise and ways to reduce them are also presented. The information given in this chapter has been derived from published literature.

In chapter 3, the thermal noise performance and suspension repair scenario for the GEO-HF detector has been discussed. The focus of this research was to design and investigate the performance of new suspension fibres, and to develop a procedure for the repair scenario of the suspension system. The designs of the fibres were investigated by the author with the help of Dr. Giles Hammond. The FEA modelling along with the calculation of dissipation dilution factor, mechanical loss and thermal noise was performed by the author. Also the fabrication of the fused silica fibres and the measurement of their breaking stress were performed by the author. Dr. Kirill Tokmakov with the help of the author carried out the tooling development works, and the fabrication of the monolithic fused silica suspension. The fibre transport tube was designed by Russell Jones and Dr. Kirill Tokmakov in consultation with Dr. Giles Hammond. The original GEO fused silica fibre was shipped to Glasgow by Dr. Stefan Goßler from Max Planck Institute for Gravitational Physics (Albert Einstein Institute) at Hannover (Germany). The dimensions of the GEO fibres were profiled by Dr. Kirill Tokmakov. The hydroxide catalysis bonding of the fused silica ears to the silica test mass was performed by Dr. Marielle van Veggel.

Chapter 4 of this thesis gives an introduction to photoelastic birefringence techniques. Different forms of polarized light, their production and use have been discussed. Methods to measure the retardation and relative stress in a sample through different compensation techniques have also been presented. The work discussed in this chapter has been derived from published literature.

In chapter 5, the experiments investigating the mechanical and thermal stress in fused silica samples are discussed. The experimental results were obtained by the author and Dr. Giles Hammond. The FEA modelling was performed by the author in consultation with Dr. Liam Cunningham. The welding of fused silica sample was performed by Dr. Alan Cumming and the author.

In chapter 6, a study of suspension thermal noise for applying incremental upgrades to the aLIGO detector is discussed. Methods to reduce the total diluted mechanical loss and the suspension thermal noise by studying the strain energy distribution and by increasing the dissipation dilution factor have been discussed. The FEA modelling was performed by the author. The designs for the upgrade scenario were jointly studied by the author and Dr. Giles Hammond.

Chapter 7 finally discusses the conclusions of the results presented in this thesis.

Summary

Gravitational waves are considered as ripples in the curvature of space-time and were predicted by Einstein in his general theory of relativity. Gravitational waves interact very weakly with matter which makes them very difficult to detect. However, research groups around the world are engaged in building a network of ultra sensitive ground and space based interferometers for the first detection of these signals. Their detection will open a new window in the field of astronomy and astrophysics.

The nature of gravitational waves is such that when incident on a particle, they stretch and squeeze the particle orthogonally thus producing a tidal strain. The strain amplitude expected for gravitational waves which may be detected on earth are of the order of h_{rms} ~10^{-22} to 10^{-23} (over a frequency range from few Hz to a few kHz). A network of instruments based on the Michelson interferometer design currently exists around the world. These detectors are undergoing a major upgrade and once online by 2015-16 the improved sensitivity and increased sky coverage may lead to the first detection of the gravitational waves signals.

The Institute for Gravitational Research in the University of Glasgow in collaboration with the Albert Einstein Institute in Hannover, Golm and the University of Cardiff has been actively involved in the research for the development of instruments and data analysis techniques to detect gravitational waves. This includes construction of a long ground based interferometer in Germany called GEO 600 (upgraded to GEO-HF) having an arm length 600 m and strong involvement in the larger detectors of the LIGO (Laser interferometer gravitational wave observatory) project in USA having arm lengths of 4 km (Operated by MIT, Boston and CALTECH, Pasadena). An upgrade to LIGO called Advanced LIGO (aLIGO) is currently under construction with significant input from the University of Glasgow.

Thermal noise is one of the most significant noise sources affecting the sensitivity of the detector at a range of frequencies. Thermal noise arises due to the random fluctuations of atoms and molecules in the materials of the test mass mirrors and suspension elements, and is related to mechanical loss in these materials.

The work presented in chapter 3 of this thesis is devoted to the analysis of aspects of mechanical loss and thermal noise in the final stages of the GEO suspension. GEO-600 is currently undergoing an upgrade to GEO-HF targeting sensitivity improvements in the kiloHertz region. However, the planned upgrade requires access to the vacuum tanks enclosing the fused silica suspension system. There is a risk of damaging the suspension, which has led to a repair scenario being developed in Glasgow, to reduce the downtime of the detector. An optimised design of the fused silica fibre has been proposed. A study of mechanical loss has been undertaken through Finite Element Analysis (FEA) modeling techniques. The mechanical loss of the optimised fibre is estimated to be lower than the original GEO fibre by a factor of ~4. In terms of thermal noise performance the optimised fibre gives an improvement of ~1.8.
The repair scenario of the monolithic suspension has led to the development of tools and welding procedures. Three prototype suspensions involving metal masses were successfully built, before fabricating the monolithic fused silica suspension in Glasgow.

The work in chapter 4 focuses on the theory of photoelasticty and birefringence techniques. The production and use of various forms of polarised light has been discussed. A setup of plane and a circular polariscope using two polarisers and two-quarter wave plates has been shown. The retardation of light due to the birefringence in the sample can be measured using the Tardy method of compensation and a Babinet-Soleil compensator. Finally a discussion on the stress-optic law has shown that the relative stress in a sample can be measured once the retardance is known.

The silica fibres in the aLIGO detector would be laser welded using a 100 W CO_2 laser. The laser welding would lead to high temperature and development of thermal gradients. This could result in residual thermal stress in fused silica, which could lead to an additional mechanical loss. A study of mechanical and thermal stress induced in fused silica has been discussed in chapter 5 of this thesis. To understand the working of photoelastic techniques learned in chapter 4, a study of mechanical stress was undertaken by applying a load on the sample to induce temporary birefringence. The estimated values of stress showed a good agreement when compared with the theoretical predictions and FEA modelling. Thermal

stress was induced in fused silica by applying a 25 W CO_2 laser beam for 10 seconds and the relative stress was measured using photoelastic birefringence techniques. Thermal modelling of the stressed sample was performed using the techniques developed in FEA. The experimental values show a good agreement with the estimated 1st principal stress (FEA model) and equivalent stress. A study of thermal stress in fused silica welds has also been presented in chapter 5. Two fused silica samples were welded using CO_2 laser welding and the relative stress at different points were measured. The stress in the weld region was measured to be relatively lower than other areas. At a distance of 3 mm away from the weld line the maximum stress was measured which was greater than the stress in the weld region by a factor of ~5.

The work discussed in chapter 6 focuses on the study of the suspension thermal noise in aLIGO detector for applying incremental upgrades. To further enhance the sensitivity of the aLIGO detector, incremental upgrades could be applied to the suspension system to improve the thermal noise. The incremental upgrades focused on two aspects: improving the dissipation dilution factor, and obtaining a lower mechanical loss than the aLIGO baseline. Based on the results from FEA, two designs were compared, each having a suspension of length 100 cm but different stock diameter - 3mm and 5 mm. A comparison with the aLIGO baseline showed that these two models obtained a lower mechanical loss by a factor of 3.4 to 6.8. In terms of suspension thermal noise there was an improvement by factor of 2.5 to 3.7, which could lead to rise in the sensitivity of the detector by a factor of 2.5.

Chapter 1 Gravitational waves, sources and their detection

1.1 Introduction

Albert Einstein, in his 'General Theory of Relativity' proposed the existence of gravitational waves in 1916 [1]. Gravitational waves can be described as ripples in the curvature of space-time and perceived as fluctuating tidal forces on the masses in their path. Theoretically, the 'Linearised Einstein Field Equations' show that gravity propagates as a wave in the universe at the speed of light [2].

Work on the detection of gravitational waves was started in 1960 with Joseph Weber [3, 4]. His experiments with resonant bar detectors were not successful in directly detecting gravitational waves; however they stimulated other researchers to build more sensitive detectors and research in this area is still ongoing [5, 6].

Strong evidence for the existence of gravitational waves was provided by work from Hulse [7] and Taylor [8] who were awarded the Nobel Prize for Physics in 1993 for their discovery of the binary pulsar PSR 1913+16 and their subsequent interpretation of the evolution of the orbit of this system. The observation showed the decay of orbital period with time, and the corresponding loss of the angular momentum and energy of the system were consistent with the predictions of general relativity for a system radiating gravitational waves, as shown in figure 1.1. Thus the observations provided indirect evidence for the existence of gravitational waves [9].

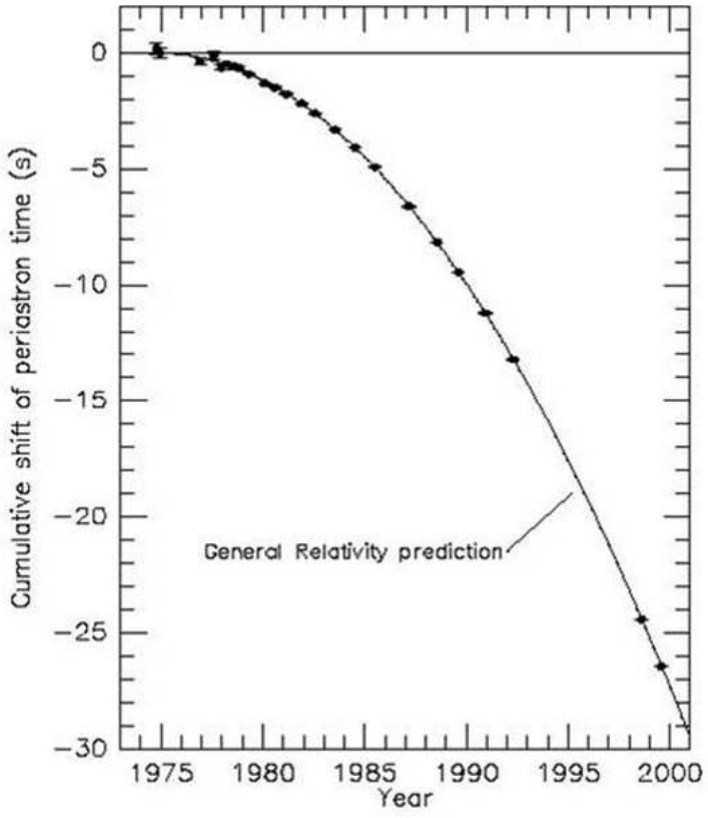

Figure 1.1 Decay of the orbital period of binary pulsar PSR1913+16 with time. The solid line shows the prediction from general relativity[8].

At present many groups around the world are working in close collaboration to realise the goal of detecting gravitational waves. The detection of these waves is highly important from an astrophysical point of view. Their detection will provide unique and exciting information about the Universe. Complex phenomena such as the birth, nature and interactions of black holes will be revealed and useful insights will be gained into the collapse mechanism of stars. Overall, detection of gravitational waves will open a new window in astronomy and astrophysics. The design of a gravitational wave detector offering a high sensitivity over a wide range of frequencies consists of test masses suspended as pendulums whose relative positions are sensed using laser interferometric techniques.

This chapter will discuss the nature of gravitational waves (section 1.2), sources (section 1.3) and some of the techniques for their detection (section

1.4). Finally the noise sources limiting the sensitivity of detectors will be covered in section 1.5.

1.2 The nature of gravitational waves

The gravitational force is the weakest among all the forces in nature. Gravitational waves are produced when matter is accelerated in an asymmetrical way. However due to the weak nature they only reach a level where detection should be possible when very large masses are accelerated in a very strong gravitational field.

In electromagnetism the acceleration of positive and negative charge oscillating about their equilibrium position produces dipole radiation. However, due to the conservation of total linear momentum and total angular momentum of the system, there can be no mass dipole gravitational radiation from any source. The lowest order gravitational radiation is quadrupole in nature which means only non-axisymmetric acceleration (i.e. varying moment of inertia) of mass will produce gravitational waves [10]. The amplitude 'h' of the gravitational wave can be defined as the strain it produces in space due to a 'tidal force', given by,

$$h = \frac{2\Delta L}{L}, \tag{1.1}$$

where $\frac{\Delta L}{L}$ is the strain.

Gravitational waves reaching the earth from distant sources have two independent polarizations of amplitude h_+ and $h_\times$. Figure 1.2 shows the effect of the resulting strain on a ring of test particles of diameter L for both polarisations. The diameter of the ring increases by ΔL in one direction and decreases by ΔL in the other direction once a wave propagating perpendicular to the page is incident on it. The angle between the two polarization forms of the gravitational waves, i.e. h_+ and $h_\times$ is $\pi/4$ unlike the electromagnetic wave, which is $\pi/2$. However the motion of the test particles acted upon by the gravitational waves is orthogonal [11].

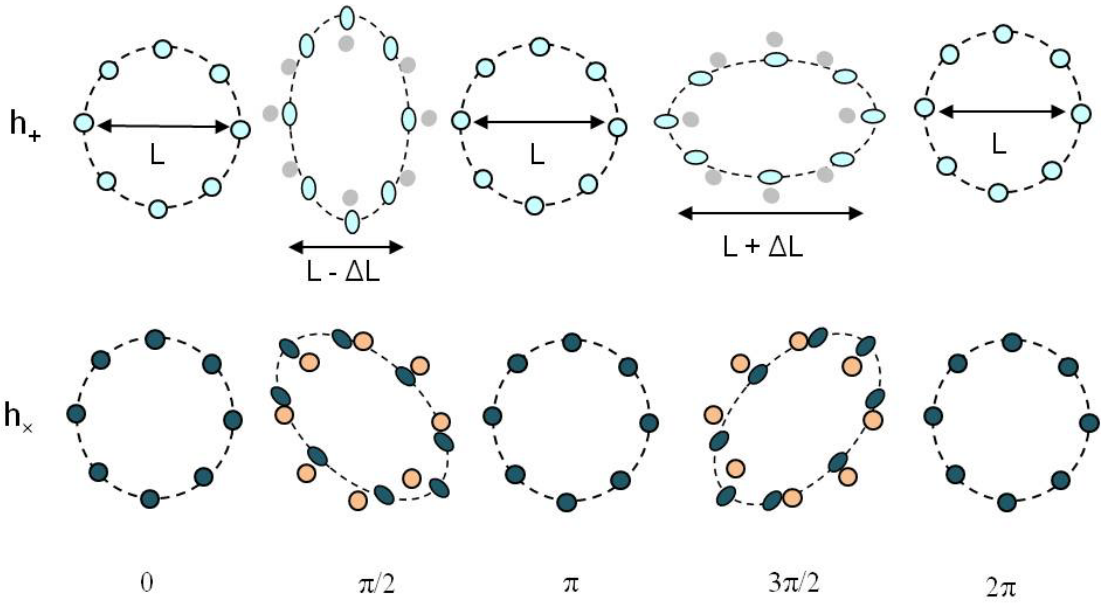

Figure 1.2 The effect of the two polarisations of gravitational waves on a ring of test particles, the direction of propagation of wave is perpendicular to the page. The particles are stretched and squeezed in the orthogonal direction.

1.3 Sources of gravitational waves

The frequencies of the ground-based detectors expecting to detect gravitational waves are in the range of a few Hz to few kilo Hz. There are various sources through which the gravitational waves may be detectable; some of them are outlined in the following subsections.

1.3.1 Burst sources

Supernovae

A supernova is an explosion of a star causing an extremely luminous burst of radiation, thus bringing an end to the life of the star. The life of a star is dependent upon the inward pressure due to the force of the gravity, and is balanced by an outward pressure due to the thermal radiation. The thermal radiation comes from the fusion reactions taking place in the core of the star.

A white dwarf star is formed when a star having a mass of less than 5 solar masses begins to collapse, as it is no longer supported by electron degeneracy pressure and thermal radiation. The star would slowly cool down and lose mass by blowing the outer layer off to get from 5 M_Θ (solar mass)

to less than 1.4 $M_{\odot}$ reaching the Chandrasekhar limit [12]. However, if it has a companion star it may start accreting mass from the companion or even merge with it. The companion may be a larger star which does not have a strong enough gravitational force to tightly bind the outer-most layers. The collapse of the core of a white dwarf star due to further accretion of mass leads to Type Ia supernova as shown in figure 1.3. If the collapse is asymmetric, having significant angular momentum, then it will result in emission of gravitational radiation. However if the deformation were symmetric then no gravitational radiation would be emitted. A larger star may also form an iron core, which shrinks continuously and is supported by electron degeneracy pressure until their mass exceeds the Chandrasekhar limit. The core of the star would collapse once the electron degeneracy pressure is no longer able to sustain it. If the mass is sufficiently high then the collapse of the core would lead to the formation of a black hole. The collapse of the cores of these larger stars is classified as Type II supernovae, shown in figure 1.3. Once again if the collapse is asymmetric then gravitational waves would be produced.

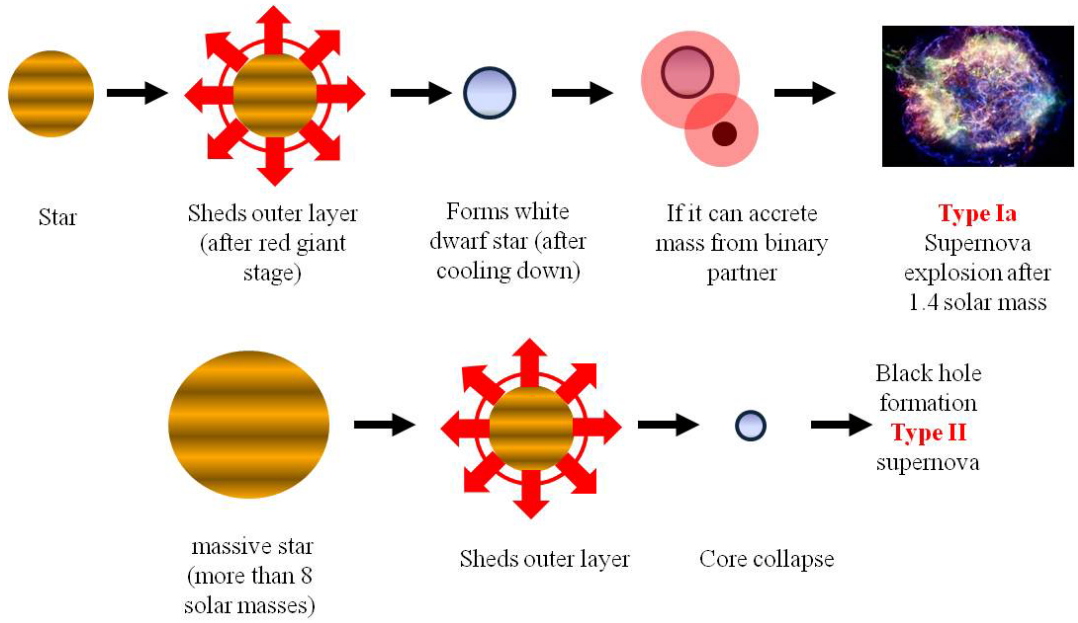

Figure 1.3 Schematic of the death of two stars (having different masses), leading to supernova explosion of Type Ia and Type II.

The strain amplitude "*h*" as expected from supernovae was given by Schutz [13], and is as follows,

$$h \approx 5 \times 10^{-22} \left(\frac{E}{10^{-3} M_{\Theta} c^2}\right) \left(\frac{15Mpc}{r}\right) \left(\frac{1kHz}{f}\right) \left(\frac{1ms}{\tau}\right)^{\frac{1}{2}}, \quad (1.2)$$

where E is the total energy radiated in the form of gravitational waves, M_{Θ} is the mass of the sun, c is the speed of light, f is the frequency of the gravitational waves, τ is the time for the collapse to occur and r is the distance from the source.

From the fifth science run of the LIGO (*Laser Interferometer Gravitational-wave Observatory*) detectors no gravitational wave signals are detected, this results in an upper limit of less than 0.015 events per day at signal level $\geq 5\times10^{-21}$ $Hz^{-1/2}$ [14] (since the unit of power spectral density is 1/Hz, the unit of strain sensitivity is $1/\sqrt{Hz}$.).

Coalescing compact binaries

A compact binary system can be defined as a combination of two compact stars (e.g. neutron stars or black holes) orbiting around a common centre of mass. Compact binary systems exist in the following forms: neutron / neutron star (NS/NS), black hole / black hole (BH/BH) and neutron star / black hole (NS/BH) combinations. In a binary system like PSR 1913+16, the orbital period decreases because of the loss of energy in the form of gravitational waves. As the distance between the two stars decreases, the amplitude and frequency of gravitational radiation increases. In the last few seconds, before the coalescence of the two stars, the amplitude and frequency values will increase such that it will be observable with the ground based detectors. According to Schutz [13] the estimated strain amplitude for a coalescing neutron star will be,

$$h \approx 1 \times 10^{-23} \left(\frac{100Mpc}{r}\right) \left(\frac{M_b}{1.2M_{\Theta}}\right)^{\frac{5}{3}} \left(\frac{f}{200Hz}\right)^{\frac{2}{3}}, \quad (1.3)$$

where $M_b = (M_1 M_2)^{3/5}/(M_1 + M_2)^{1/5}$ is the "chirp" reduced mass parameter of the binary system, M_1 and M_2 are the masses of the two stars. The other symbols are as defined in equation (1.2).

The population of binary systems having black holes is smaller than for neutron stars; however the higher density and mass will lead to larger

amplitudes of gravitational radiation, which will increase the chances of detection. In the data taken by the LIGO-VIRGO and GEO detectors no evidence has been observed for a neutron star within a distance of 14 Mpc [15, 16].

1.3.2 Periodic sources

Pulsars

Pulsars are rotating neutron stars and a possible source of continuous gravitational waves. Gravitational waves are expected to be emitted as a result of the non-axisymmetric spin of a pulsar from residual crustal deformation. This could be due to cracking of the crust in the strong magnetic field of the star. The waves emitted from such a pulsar are expected to have a frequency of twice the pulsar rotational frequency, f_{rot}. The strain amplitude of the radiation from such a source can be estimated to be [17],

$$h = 6 \times 10^{-25} \left(\frac{f_{rot}}{500Hz}\right)\left(\frac{1kpc}{r}\right)\left(\frac{\varepsilon}{10^{-6}}\right). \quad (1.4)$$

The measure of the degree of non-symmetry in the star is given by *"ε"*, the equatorial ellipticity.

In 1054, Chinese astronomers recorded the remnant of a supernova in the Crab nebula, this object has an expected source of gravitational waves at around 60 Hz with an estimated strain amplitude of $h \sim 10^{-24}$, $\varepsilon \sim 7 \times 10^{-4}$, $r = 1.8$ kpc and $f_{rot} = 30$ Hz [17]. From the fifth science run of the LIGO detectors, the ellipticity of the Crab Pulsar must be smaller than 1.8×10^{-4} [18].

1.3.3 Stochastic sources

The superposition of signals from many sources may lead to the existence of a background of gravitational waves, which is similar to coalescing compact binaries (CMB), whose amplitude may be high enough to be detected as a stochastic background. A single detector will not be able to distinguish these stochastic backgrounds from the presence of noise. Hence a combination of several detectors can be used to cross-correlate the data and separate the stochastic background from the random noise [19].

Assuming the cosmic string scenario for the formation of the structure in the universe, a level of background radiation can be predicted whose amplitude is given by [20],

$$h \approx 2.4 \times 10^{-25} \left(\frac{H_0}{75\ kms^{-1}Mpc^{-1}}\right)\left(\frac{\Omega_{gw}}{10^{-8}}\right)^{\frac{1}{2}}\left(\frac{f}{100Hz}\right)^{\frac{-3}{2}}\left(\frac{B}{2Hz}\right)^{\frac{1}{2}}, \qquad (1.5)$$

for a bandwidth B, about a frequency f, where Ω_{gw} is the energy density per logarithmic frequency interval required to close the universe and H_o is the Hubble constant. From the fifth science run the amplitude of a stochastic background of gravitational waves must be less than 6.5×10^{-25} [21]. The results were used to explore the parameter space of some models of the stochastic background, including the cosmic strings models and pre-big bang models.

1.4 Gravitational wave detectors

Gravitational waves cause a very small strain '$h_{rms}=10^{-23}$', in space-time. In order to detect these signals ultra sensitive detectors are required. Designs currently being developed include resonant bar detectors and laser interferometers. These two designs are ground based detectors targeted at sources emitting at frequencies above 10 Hz. A space based detector aimed at lower frequency signals is also planned and will be discussed in section 1.6.

1.4.1 Resonant bar detectors

The bar-type detectors were the first ground based detectors and were initially developed by Joseph Weber at University of Maryland about 45 years ago [22]. Each bar consisted of a large aluminium cylinder with a mass of several tons which was well isolated from ground vibrations and acoustic noise in the laboratory [3, 4]. The bars had a resonant mode at ~ 1600 Hz such that a gravitational wave of the same frequency incident on the bar would lead to vibration of the cylinder, thus causing a mechanical strain which would be measured by a transducer and amplifier.

Weber placed his detectors 1000 km apart and searched for coincident excitations, claiming some success. However similar experiments carried out at other laboratories in USA, Germany, UK and Russia could not duplicate

Weber's results and expected amplitudes of gravitational wave signals were at a level that was below the sensitivity of the Weber-type detectors. The development of the resonant bar types of detector continued and strain sensitivity levels of around 10^{-20} for millisecond pulses have been achieved. Mini GRAIL [23] and Mario Schenberg Detector [24] have measured strains of $h \sim 10^{-21}$ at 3 kHz . However the bar detectors have a narrow frequency bandwidth and are sensitive only to signals that have significant spectral energy within this bandwidth. To overcome this limitation, gravitational wave detectors based on laser interferometry have been designed and developed and will be discussed in the next section.

1.4.2 Laser interferometer

In 1970, Forward [25] and Weiss [26] started work on laser interferometers for the detection of gravitational waves. A gravitational wave detector based on the technique of laser interferometry offers high sensitivity over a wide range of frequency. These detectors look for the effects of gravitational waves on the position of the test masses, suspended as pendulums, which are widely separated from each other and isolated against seismic noise. This technique is based on the principle of a "Michelson interferometer" as shown in figure 1.4.

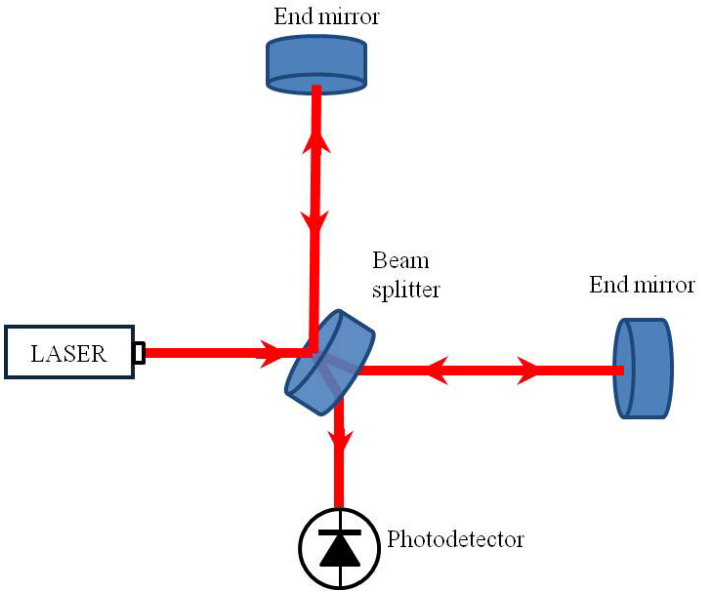

Figure 1.4 Schematic of a simple Michelson interferometer.

In a Michelson interferometer light from a laser is incident on a beam splitter where the light is partially reflected and partially transmitted into the orthogonal arms. The light is then reflected back from the end mirrors to the beam splitter where the light is recombined and interference occurs. The interference fringes are then sensed via a photodiode. Any motion of the mirrors changes the relative arm length and thus causes a change in the intensity of the interference pattern. The mirrors are suspended as pendulums and under vacuum so as to isolate them from seismic noise, pressure fluctuation and other sources such as thermal noise, and gas damping.

When a gravitational wave is propagating in a direction perpendicular to the plane of the arms of the interferometer, it produces a fractional change in the arm length, such that one arm will increase by an amount ΔL and the other will decrease by ΔL. Hence it can be realised that the detectable signal strength is directly proportional to the length of the arm. The optimum arm length for a wave of frequency 1 kHz can be calculated [10],

$$L_{optimum} = \frac{c}{4f} \approx 75\ km. \tag{1.6}$$

Arm lengths for the ground-based interferometer are currently limited to around 4 km, due to practical considerations such as curvature of earth and ease of construction. However a delay line arrangement [26] or a Fabry-Perot cavity in each arm of the instrument [27] can be used to effectively increase the arm length by reflecting the light as shown in figures 1.5 and 1.6.

Delay line interferometer

Proposed by Weiss [26] in the 1970's, the design consists of two additional "inboard mirrors" in between the "beamsplitter" and the "outboard mirrors", as shown in figure 1.5. The reflected or transmitted light from the beamsplitter enters the inboard mirror through a hole. The light then undergoes multiple reflections between the two curved mirrors and thus increases the optical path length. The light then exits the delay line through the same hole. However delay line interferometers are susceptible to noise from scattered light.

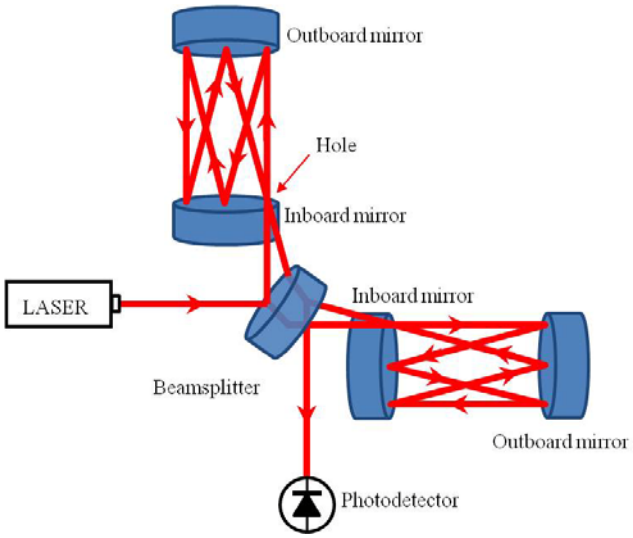

Figure 1.5 Schematic of a delay-line interferometer

Fabry-Perot interferometer

The Fabry-Perot interferometer uses Fabry-Perot cavities in the arms of the interferometer so as to increase the storage time as shown in figure 1.6. This technique was initially developed in Glasgow in the early 1980's [27]. The cavities are held to resonate with the carrier frequency of the laser light using electronic feedback and actuation systems such that multiple reflections of the light lie on the same spatial path. One advantage in using this technique rather than the delay-line arrangement is the reduction of noise introduced through scattering of light. However an additional complexity is introduced through the necessity of adding control systems to hold the cavities on resonance. A typical power gain in the cavities of the LIGO detector is from 10 W to 10 kW.

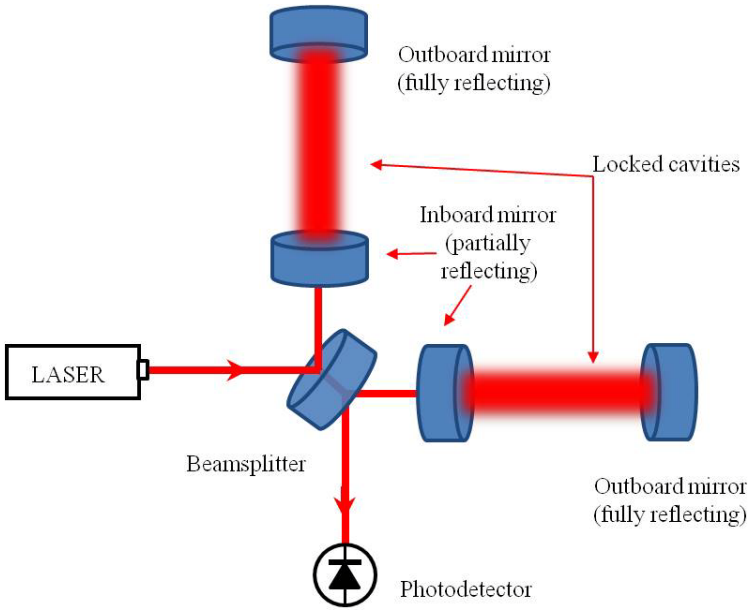

Figure 1.6 Schematic of a Fabry-Perot interferometer

Power and signal recycling

The Power recycling technique requires an additional mirror placed before the beam splitter with the intention of re-using the laser light which is coming back from the interferometer, as shown in figure 1.7(a). Since the interferometer is operated just off the dark fringes at the output photodiode, the majority of light exits the interferometer towards the laser. By placing a partially reflecting mirror in between the laser and the beam splitter a resonant cavity can be formed where the interferometer will act as the second mirror [28]. This is done to increase the laser power and enhance the sensitivity of the instrument. The power build up inside the interferometer is high enough to create the required kilowatts of laser power at the beamsplitter [29].

Similarly, through signal recycling one can reuse the laser light produced by the effect of a gravitational wave signal at the output port to increase the sensitivity of the interferometer [30]. The laser light coming out of the interferometer at the photodiode may be recycled back into the interferometer by placing a partially transmitting mirror in between the beam splitter and the photo diode. This will lead to the formation of an optical cavity between the signal recycling mirror and the interferometer [31]

and will result in an enhancement of the signal produced by an incoming gravitational wave (in a narrow band allowing specific tuning) for sources such as continuous waves from neutron stars.

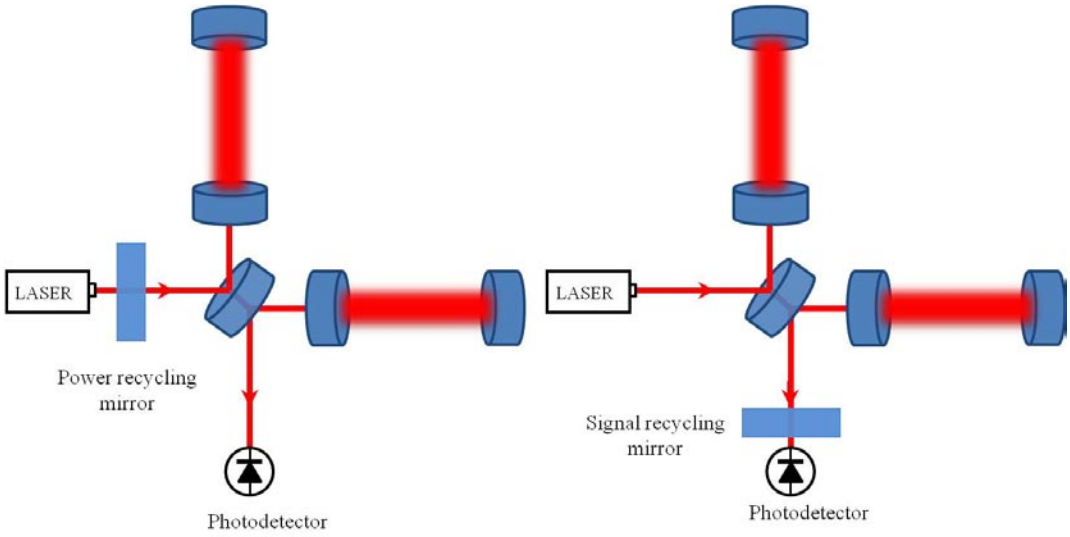

Figure 1.7 Schematic of a Fabry-Perot interferometer, (a) – picture on the left shows the addition of a power recycling mirror and (b) – on the right the addition of a signal recycling mirror.

1.5 Noise sources

The sensitivity of an interferometric gravitational wave detector is affected by a number of noise sources. In this section some of the common noise sources will be discussed.

1.5.1 Seismic noise

Seismic noise arises from natural phenomena such as earthquakes, ocean waves beating on the shore or from man-made sources like movement of traffic. The level of seismic noise depends upon the location of a site and may vary with time. However at a reasonably quiet site on the earth the seismic noise could be around $10^{-7}f^{-2}m/\sqrt{Hz}$ [32]. The pendulum suspensions used in gravitational wave detectors have been specifically designed as active and passive isolation system for seismic isolation over the range of frequencies in which the detectors operate. For the horizontal and vertical direction the pendulum attenuates the displacement by a factor of

$\left(\frac{f_0}{f}\right)^2$ where f_0 is the resonant frequency and f is the frequency at which it is driven [10, 33].

1.5.2 Gravitational gradient noise

Gravity gradient noise, also called Newtonian noise, results from the mirrors directly coupling with local fluctuations in the gravitational field [34]. This is caused by the changing mass distribution of the surrounding area and is likely to limit the sensitivity of the detectors at a frequency less than 10 Hz. Building a detector underground (future detectors like the Einstein Telescope) or in space like NGO is one of the possible solutions to reduce gravity gradient noise through active subtraction techniques with seismometers [35].

1.5.3 Thermal noise

Thermal noise in an interferometer results from the thermal energy of atoms and molecules in the test masses, coatings and the suspension system [36]. It is one of the important noise sources, which affects the sensitivity of the detector from few Hz to several 100 Hz [37, 38]. The suspension thermal noise arises from the Brownian motion of the atoms and molecules and dissipation in the different parts of the system such as the suspension elements, including the test mass, fibres and ears. Hence the materials used for the suspensions should be of low mechanical loss, such as fused silica. Such a material reduces the effects of Brownian noise. The aspects of suspension thermal noise will be further discussed in chapter 2.

Coating thermal noise is one the other significant noise sources, which arises from the mechanical loss of the mirror coatings applied to the test masses for high reflectivity. Ta_2O_5 is a highly dielectric coating material [39], which has low optical loss properties and is also used in the optical industry. These coatings are applied on the test mass surface as alternating layers of varying refractive index. The thermal noise associated with the multilayer dielectric coating will limit the sensitivity of the second generation of detectors at their most sensitive frequency band. In order to reduce the thermal noise arising from the test masses, the design of the test masses should be such that they have very high internal resonant mode frequencies and their size should be large enough to accommodate the laser beam spot [40].

1.5.4 Quantum noise

Quantum noise comprises of photon shot noise at high frequency and radiation pressure noise at low frequency. Photon shot noise occurs due to the fluctuations in the number of photons at the output of an interferometer. According to Poisson statistics if N photons reach the output of the interferometer then the uncertainty associated with counting the photons is $\sqrt{N}$. This leads to noise at the photodiode, which in turn decreases the sensitivity of the detector. The shot noise limited sensitivity for a simple Michelson interferometer type interferometer is given by [41],

$$h_{shot}(f) = \left(\frac{1}{L}\right)\left(\frac{\hbar c\lambda}{2\pi P_{in}}\right)^{\frac{1}{2}}, 1/\sqrt{Hz}\,, \tag{1.7}$$

where $\hbar$ is Planck's constant, λ is the wavelength of light, L is the length of the interferometer arm, c is the speed of light and P_{in} is the laser power. It should be noted that increasing the laser power helps to improve the shot noise limited sensitivity; however it can also lead to an increase in the radiation pressure noise in the instrument. Radiation pressure noise results from the transfer of momentum to the test mass mirrors from photons reflecting off the surface of the test mass.

The power spectral density of the fluctuation due to radiation pressure noise at frequency f is given by [42],

$$h_{rp}(f) = \frac{N}{mf^2L}\sqrt{\frac{2\hbar P_{in}}{\pi^3\lambda c}}, 1/\sqrt{Hz} \tag{1.8}$$

where N is the number of reflections of light in a cavity and m is the mass of the mirror. In a simple Michelson type interferometer at a particular frequency the shot noise can be made equal to the radiation pressure noise, however this requires optimization of the input laser power. This is known as the 'standard quantum limit' [43]. Advanced LIGO is likely to be limited by quantum noise between 10 Hz and 50 Hz [44]. Increasing the mass of the mirrors or by using a lower laser power can reduce the effects of radiation pressure noise. However, lowering the laser power degrades the sensitivity at higher frequencies.

1.6 Status of interferometric gravitational wave detectors

A network of laser interferometers for detecting gravitational waves is currently being built around the world. The sites of the laser interferometers are shown in figure 1.8.

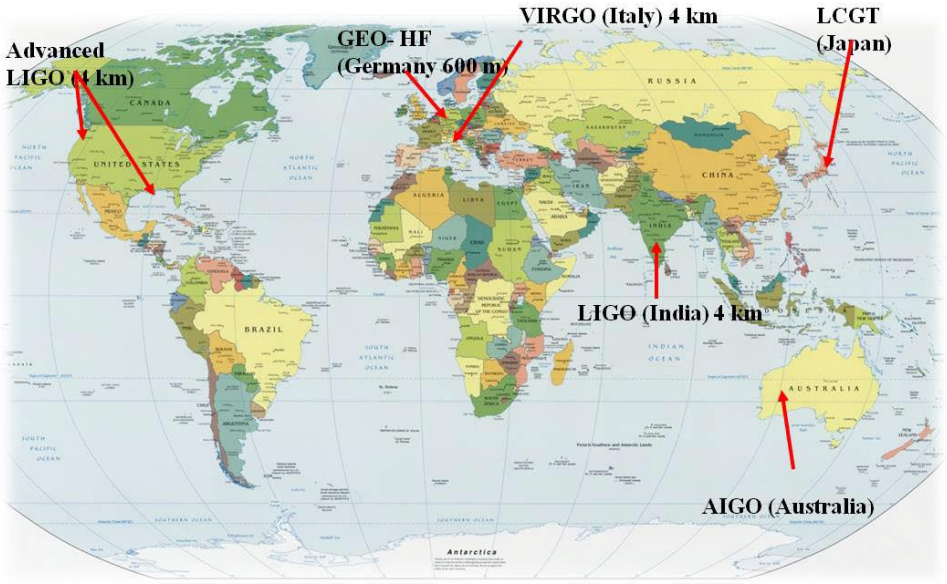

Figure 1.8 The network of major detectors built around the world for the detection of gravitational waves signals.

LIGO and Advanced LIGO detectors

The LIGO project operated detectors located at two different sites in USA [45], one at Hanford (WA) and the other at Livingston (LA), shown in figure 1.9. These detectors were conducting science runs until 2011. The arm length of these detectors is 4 km. There is a second instrument installed in the Hanford vacuum enclosure, which will be shipped to India for the LIGO India (4 km) detector. The test masses in the interferometer were constructed out of 10.7 kg silica mirrors and each one was suspended in a single wire loop wire suspension, operating with a 10 kW laser power in the Fabry-Perot cavity.

Figure 1.9 Arial photographs of the two LIGO detector sites in the USA, on the left is the LIGO Livingston in Louisiana and the image on the right is the LIGO Hanford in Washington.

Figure 1.10 shows the strain sensitivity (amplitude spectral density) of the LIGO detector for the different science runs made from 2002 till the fifth science run S5 (2007). The best strain sensitivity of $h \approx 3 \times 10^{-23}\sqrt{Hz}$ over a frequency range of 100 Hz to 200 Hz was achieved in the year 2007 from the fifth science run [46]. The LIGO detector ceased operation in 2011.

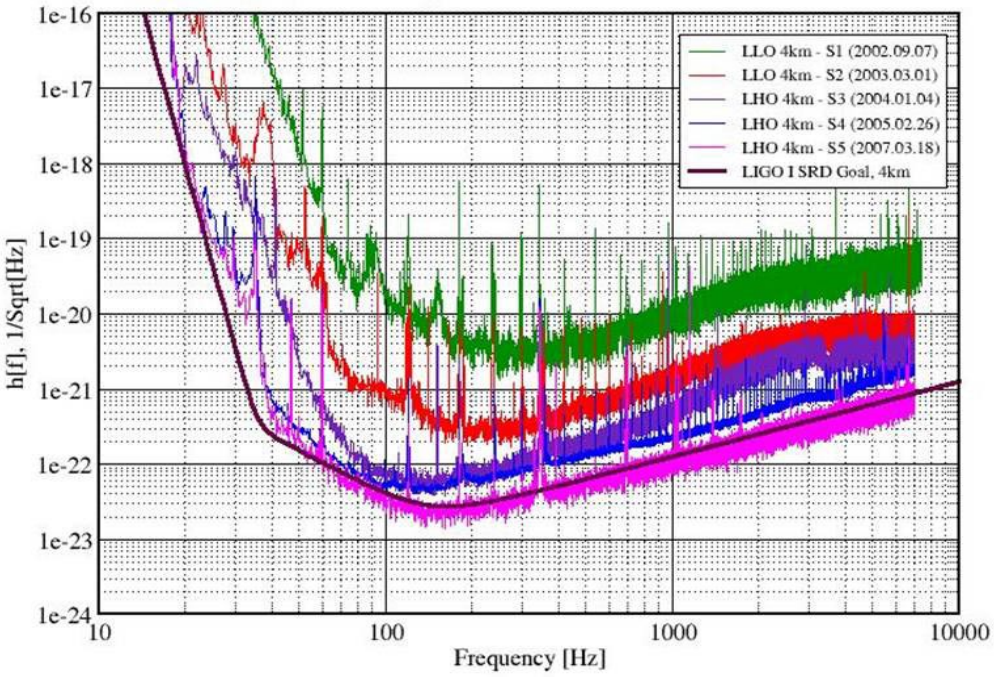

Figure 1.10 Strain sensitivity of the LIGO detectors for different science runs; the most recent data shown is from the fifth science run, S5, in 2007 [47].

An upgrade to LIGO, Advanced LIGO (aLIGO), is currently under installation/fabrication phase and is expected to be online by 2015-16 at the two sites in the USA [44]. Advanced LIGO will employ a quadruple pendulum fused silica suspension system, increased laser power and improved coatings applied to the test mass mirrors [48]. The quasi monolithic fused silica suspension mirrors will employ four silica fibres of diameter 400 microns, suspending a 40 kg silica test mass. A steel wire in a loop will suspend the intermediate mass. The seismic noise will be minimised down to 10 Hz due to an improved suspension isolation system thus giving a broader detection bandwidth. Power and signal recycling as well as light squeezing techniques used in the GEO 600 will also be employed in the Advanced LIGO detector. Figure 1.11 shows the individual and total noise budget projected for the Advanced LIGO detector. The plot shows that the suspension thermal noise is dominated by quantum noise above 12 Hz. The proposed sensitivity for Advanced LIGO is expected to exceed that of LIGO by a factor of ten. This may expand the volume of space observed by detectors by ~ 1000 times, which may lead to the detection of several 10's of events per year [49]. The binary neutron star detection rates for the aLIGO-Virgo network is 40 events per years, with a range of 0.4 to 400 per year [50, 51]. The event rate for the supernovae out to the VIRGO super cluster at a distance of ~ 15 Mpc, is estimated to be several per month [52] for the aLIGO detector.

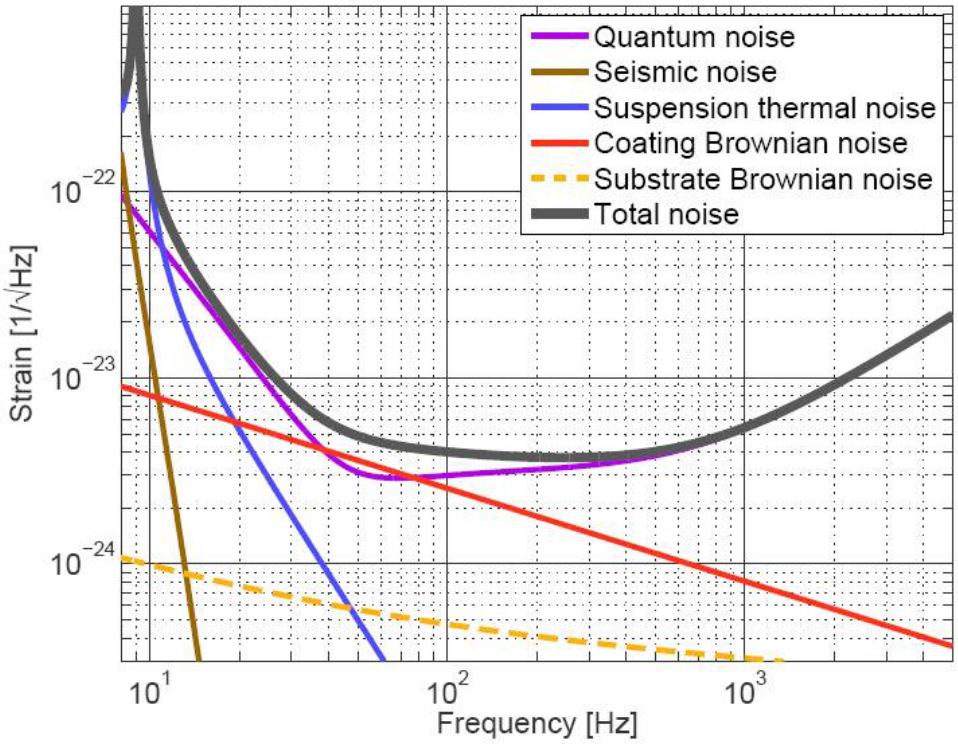

Figure 1.11 The projected noise budget of the aLIGO detector.

A third LIGO detector is planned to be located in India, which will be a 4 km interferometer and will use the components from the second half length arm of the Hanford site. Initially AIGO (Australia) was proposed for the third LIGO detector site, while India was the second option. Australia being in the southern hemisphere of the globe would have greatly improved the network. However the funding for this third detector was approved by CSIR, India. This third detector will help in triangulation of the gravitational wave signals. The installation of the detector is expected to start around 2017-18.

GEO 600 detector

The German-British GEO 600 detector is an interferometric gravitational wave detector near Ruthe outside Hannover in Germany. The overall design sensitivity of the detector in terms of amplitude is $2\times10^{-22}/\sqrt{\text{Hz}}$ at 50 Hz [53-55]. In order to achieve this sensitivity, a significant degree of seismic isolation has to be provided to the test mass in the horizontal and vertical direction. This is accomplished by using a triple pendulum system suspended from cantilever springs [56] including a lower stage of fused silica.

The details of the suspension system of GEO 600 detector can be found in the literature [57]. It should be noted that the suspension system for Advanced LIGO is developed from GEO 600 detector's design.

Figure 1.12 shows the site of the GEO 600 detector in Germany, having an arm length of 600 m. Figure 1.13 shows the best strain sensitivity measured for the GEO 600 detector which is compared to the sensitivity of the LIGO and VIRGO detector.

Figure 1.12 Figure on the left shows the GEO 600 site at Ruthe near Hannover, the central building for the laser can be seen, the figure on the right shows one of the arm which is a 600 m long vacuum tube.

GEO 600 is currently being upgraded to GEO-HF status. GEO-HF will employ squeezed light technology [58] and install an output mode cleaner to improve its high frequency performance above 1 kHz. The major upgrade includes a change of the read out scheme from a heterodyne RF (radio frequency) read out to a DC read-out (Homodyne detection scheme) system. The input laser power will also be increased to 35 W. Details of the GEO-HF detector upgrade are discussed in chapter 3 of this thesis. The GEO detector is currently the only detector among the LSC community, which is online and taking data till the Advanced LIGO detector comes online in 2015~16.

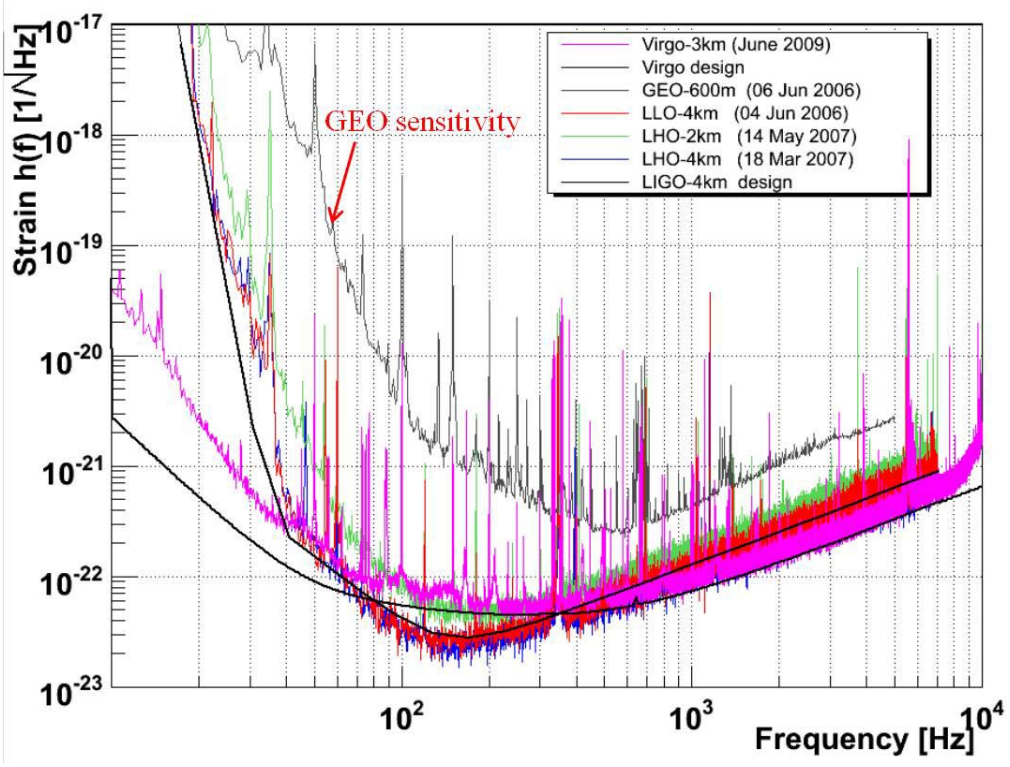

Figure 1.13 Comparison of the best strain sensitivity measured for GEO 600, the LIGO and VIRGO detectors [32].

Virgo+ and Advanced Virgo detector

Virgo is a 3 km, French/Italian detector situated at Cascina, near Pisa, which started its first science run in the year 2004 achieving a strain sensitivity of 6×10^{-22} $/\sqrt{Hz}$ at 300 Hz [59]. The Virgo detector was upgraded to Virgo+ in 2011. The upgrade includes Fabry-Perot cavities, increased laser power (25 W), thermal compensation system on the mirrors, improved control electronics, installation of new mode cleaners and injection optics. The mirrors are suspended from a multistage pendulum system. The details of the suspension system can be found in the literature [60, 61]. The Virgo+ detector will be further upgraded to advanced Virgo, which will include higher finesse arm cavities. The advanced VIRGO will employ a fused silica suspension (silica fibres and mirrors) at the lower-most stage. The sensitivity of the detector is aimed to be increased by a factor of ~10.

KAGRA detector (LCGT)

The KAGRA detector, previously called the '*Large-scale Cryogenic Gravitational wave Telescope (LCGT)*', is currently under construction in Japan, located underground in the Kamioka mine [62]. The arm length of this detector will be 3 km. KAGRA will be operating at cryogenic temperature (20 K) and will employ sapphire as the material for the suspension elements. The sensitivity of the KAGRA detector will be similar to the advanced LIGO detector [63]. A small prototype detector already exists in Tokyo, called TAMA detector with an arm length of 300 m. The details of this detector can be found in the literature [64].

Space based interferometric detectors

The new gravitational wave observatory NGO which was earlier known as Laser Interferometer Space Antenna (LISA) [65] is an ESA (European Space Agency) project [66]. The arm length of the proposed design is 1×10^{9} metres, with three arms forming an equilateral triangle with test masses placed in three separate spacecraft. The strain sensitivity of NGO will be $h \sim 10^{-21}$ / √Hz at 1 mHz. The LISA pathfinder is scheduled to be launched in 2015 to demonstrate the feasibility and endurance of the different instruments and to validate new measurement technologies necessary for the success of any future mission. This space-based interferometer will complement the ground based detector network by studying gravitational waves from astrophysical sources emitting at frequencies (0.1 mHz to 1 Hz) in a band inaccessible to detectors based on earth.

1.7 Conclusions

The first direct detection of gravitational waves is one of the most important aspects in the field of gravitational physics astronomy and is highly awaited ever since it was first proposed in the general theory of relativity. Studies have shown that several sources such as black holes, neutron stars, and coalescing compact binaries will be emitting the gravitational waves signals and are within the reach of ground-based detectors. A network of gravitational wave detectors has been built and is operating around the world. Significant progress has been made in recent years regarding the development and upgrade of the current and future

detectors. With improving sensitivities made possible by employing new technologies, the direct detection of gravitational waves is coming closer. Once this is achieved, it will open a new window for observing the universe via the gravitational signals and form a new branch of astronomy.

The work presented in this thesis focuses on the development of current and future detectors by studying the suspension thermal noise and mechanical loss of the materials limiting the sensitivity of the detectors.

Chapter 2 Thermal noise

2.1 Introduction

Thermal noise is one of the most significant noise sources affecting the sensitivity of gravitational wave detectors at frequencies below 100 Hz. Thermal noise in the system reveals itself in two ways: through the random motions of individual atoms (Brownian motion) [67, 68], and temperature fluctuations of different parts of the system. These temperature fluctuations can result in random displacement in the system if the materials have a finite coefficient of thermal expansion or if the system is under stress and the modulus of elasticity (Young's modulus) is a function of temperature (Thermoelastic loss).

In a long baseline gravitational wave detector the study of thermal noise is important in the suspension elements of the test mass mirrors where it causes random movement of the mirrors at the pendulum modes and also the violin mode frequencies of the suspension fibres. Thermal noise also leads to fluctuations in the position of the mirror face of the test masses due to random fluctuations of the molecules in the test masses and their dielectric mirror coatings.

This chapter focuses on the theoretical description of thermal noise associated with the suspension elements in gravitational wave detectors.

2.2 Fluctuation-Dissipation theorem

The fluctuation-dissipation theorem states that in thermal equilibrium any linear system with dissipation has fluctuations [69, 70]. The power spectral density of the thermal driving force $S_F(\omega)$ is related to the dissipative (real) part of the mechanical impedance $Z(\omega)$ by the equation,

$$S_F(\omega) = 4k_B T\Re[Z(\omega)]. \tag{2.1}$$

The mechanical impedance can be defined as $Z(\omega) = \frac{F}{v} = \frac{F}{i\omega x}$, where F is the external force acting on the system and v is the velocity. Using the definition of impedance the fluctuation dissipation theorem can be written in terms of power spectrum density of thermal displacement $S_x(\omega)$,

$$S_x(\omega) = \frac{4k_B T}{\omega^2}\Re[Y(\omega)] \tag{2.2}$$

where $Y(\omega)$ is the mechanical admittance, which is inverse of impedance $\left(Y(\omega) = \frac{1}{Z(\omega)}\right)$. The equation of motion of a gas damped pendulum excluding the fluctuating forces is given by,

$$F = m\ddot{x} + b\dot{x} + kx. \tag{2.3}$$

where k is the spring constant. For a harmonic solution, $\dot{x} = i\omega x$ and $\ddot{x} = i\omega\dot{x}$, hence the above equation can be written as,

$$F = i\omega m\dot{x} + b\dot{x} + \frac{k\dot{x}}{i\omega} \tag{2.4}$$

or

$$F = \dot{x}\left[i\omega m + b - \frac{ik}{\omega}\right] \tag{2.5}$$

The mechanical impedance can now be rewritten as,

$$Z(\omega) = b + i\left[m\omega - \frac{k}{\omega}\right]. \tag{2.6}$$

The real part of Z(ω) is b and so we have,

$$S_f(\omega) = 4k_B Tb, \tag{2.7}$$

The admittance can be written as,

$$Y(f) = \frac{1}{b + i\left[2\pi fm - \frac{k}{2\pi f}\right]} \tag{2.8}$$

Rationalising the denominator and taking the real part of the admittance, the power spectral density can be written from equation (2.2) as,

$$S_x(\omega) = \frac{4k_B Tb}{\pi^2 f^2\left(b^2 + \left(\omega m - {}^{k}/_{\omega}\right)^2\right)}. \tag{2.9}$$

The calculation of suspension thermal noise in gravitational wave detectors is based on models in which the resonant modes of the test masses and suspensions are modelled as damped harmonic oscillators [71]. Damping due to internal friction introduces a phase lag ϕ (which is the loss angle), such that $b = \phi$. However for viscous damping, $b = \phi(\omega)$, where $\phi(\omega)$ represents the phase lag in radians and is frequency dependent, can be used in equation (2.3), assuming $\phi(\omega) \ll 1$. Hence in terms of power spectral density of displacement, $S_x(\omega)$, the fluctuation-dissipation theorem can be expressed as [36],

$$S_x(\omega) = \frac{4k_B T\omega_0\phi(\omega)}{2\pi^3\omega m[(\omega_0^2 - \omega^2)^2 + \omega_0^4\phi^2(\omega)]} \tag{2.10}$$

where $\phi(\omega)$ is the mechanical dissipation or loss factor of the oscillator of mass m at temperature T, $\omega_0 = \sqrt{k/m}$ is the angular resonant frequency and k_B is Boltzmann constant. Thus to minimise thermal noise we require ultra low loss materials used for the test masses and suspensions in interferometric gravitational wave detectors. In turn these material result in suspension with high quality factor Q, where $Q = \frac{1}{\phi(\omega_0)}$.

The amplitude spectral density of the thermally-induced displacement for a single pendulum of length 0.28 m, mass 5.6 kg and varying Q is shown in figure 2.1. A system having high Q puts more energy into the resonant modes while the root mean square (*rms*) is equal to equation (2.7). Gravitational wave detectors operate with high Q suspensions, which exhibit low off-resonance thermal noise.

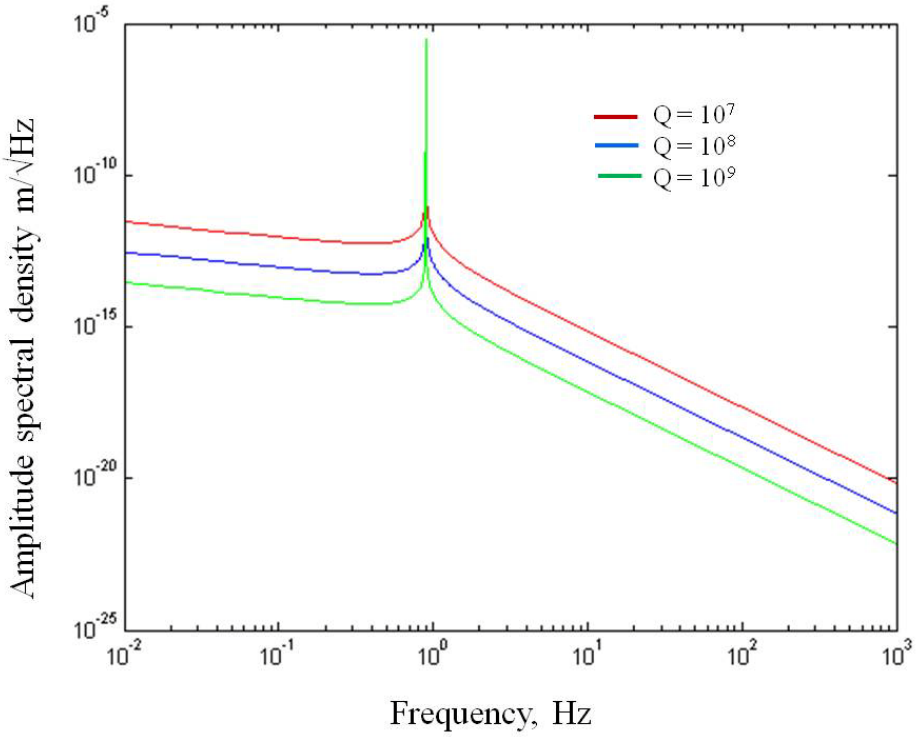

Figure 2.1 Amplitude spectral density estimated using different values of mechanical loss.

2.3 Sources of dissipation

In the mirror suspension of a laser interferometer there are many sources of dissipation which need to be minimised in order to achieve low levels of thermal noise [72, 73]. These include thermoelastic loss, surface loss, bulk loss and weld loss. In addition, the loss can be reduced by storing energy in the lossless gravity which is known as the dissipation dilution factor.

2.3.1 Dissipation dilution factor

The reason for choosing multiple pendulum suspensions is to improve the low frequency thermal noise by storing most of the energy in gravity. However, they also provide low frequency (~10Hz in aLIGO) seismic isolation to the test mass mirror. The mechanical loss of a pendulum results mostly from flexing at the ends of the fibre where maximum bending occurs. In other words, the loss is concentrated at the bending points of the fibre. Using thin fibres, helps to reduce thermal noise by storing most of the

energy in the non-dissipative gravitational field [36, 74]. To understand this effect, consider a simple pendulum suspending a mass *m*. Once the mass is suspended the tension in the wire is equivalent to '*mg*' and the wire will elongate until the elastic restoring force equals the tension in the wire.

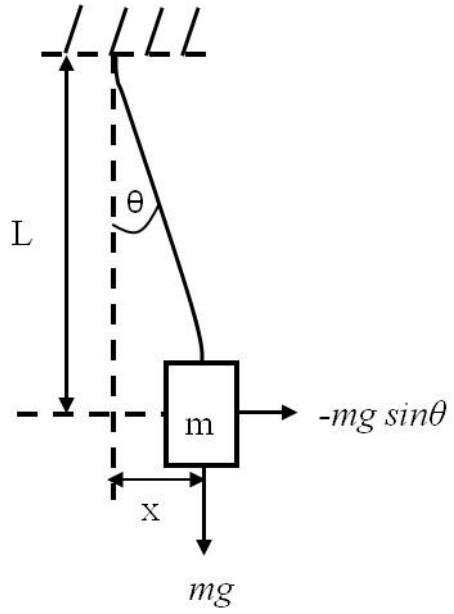

Figure 2.2 A simple pendulum system displaced horizontally, with gravity as a restoring force.

On displacing the pendulum horizontally, as shown in figure 2.2, a restoring force will be developed due to the effect of gravity on the mass and also from the spring constant of the wire. The restoring force for the gravitational field gives the equivalent spring constant of,

$$k_{grav} = \frac{mg}{L}. \tag{2.11}$$

This equation can be used to estimate the effect of the loss for such a pendulum system. The energy stored in the bending of the wire is given by,

$$E_{stored_{wire}} = \frac{1}{2} k_{wire} x^2, \tag{2.12}$$

where k_{wire} is the spring constant of the wire. If some fraction (χ) of energy is lost per cycle then it can be represented as,

$$E_{lostpercycle} = \frac{1}{2} \chi k_{wire} x^2 \tag{2.13}$$

and using the definition of loss,

$$\phi_{mat}(\omega_0) = \frac{1}{Q} = \frac{E_{lost\ per\ cycle}}{2\pi E_{stored}} = \frac{\frac{1}{2}\chi k_{wire}x^2}{2\pi(\frac{1}{2}k_{wire}x^2)} = \frac{\chi}{2\pi}. \quad (2.14)$$

Adding in the energy stored in the gravitational field,

$$E_{stored_{pendulum}} = \frac{1}{2}(k_{wire} + k_{grav})x^2. \quad (2.15)$$

Hence,

$$\phi_{pendulum}(\omega_0) = \frac{\frac{1}{2}\chi k_{wire}x^2}{2\pi\frac{1}{2}(k_{wire} + k_{grav})x^2} = \frac{\chi k_{wire}}{2\pi(k_{wire} + k_{grav})}. \quad (2.16)$$

Now from equation (2.14),

$$\frac{\phi_{pendulum}(\omega_0)}{\phi_{mat}(\omega_0)} = \frac{\frac{\chi k_{wire}}{2\pi(k_{wire} + k_{grav})}}{\frac{\chi}{2\pi}} = \frac{k_{wire}}{k_{wire} + k_{grav}}. \quad (2.17)$$

If $k_{grav} >> k_{wire}$ then,

$$\phi_{pendulum}(\omega_0) \approx \phi_{mat}(\omega_0)\frac{k_{wire}}{k_{grav}}. \quad (2.18)$$

Hence, since $k_{grav} \gg k_{wire,}$ the loss in the pendulum is reduced by the factor known as the 'dilution factor' defined as $D \equiv \frac{k_{grav}}{k_{wire}} \gg 1$.

If there are n wires suspending the mass (wires attached in a plane through the centre of mass perpendicular to the direction of swing) instead of just one wire, then the elastic spring constant is given by [36],

$$k_{wire} = \frac{n\sqrt{TYI}}{2L^2}, \quad (2.19)$$

where T is the tension in each wire, Y is the Young's modulus of the wire material, I is the second area moment of inertia, defined as $I = \int y^2 dA$, with y the distance to x-axis and dA the unit element of area. For a circular cross section wire $I = \frac{\pi r^4}{4}$ [75], where r is the radius of the wire. Hence the total pendulum loss is given by,

$$\phi_{pendulum}(\omega_0) \approx \phi_{mat}(\omega_0)\frac{n\sqrt{TYI}}{2mgL} \tag{2.20}$$

The loss in the pendulum is directly proportional to the loss of the material used for its suspension fibres but reduced by the dilution factor. Since the dilution factor can be expressed as $\frac{1}{D} = \frac{\phi_{pendulum}}{\phi_{material}}$, substituting for the term per wire, '$mg=nT$' gives,

$$\frac{1}{D} = \frac{\sqrt{YI}}{2L\sqrt{T}}. \tag{2.21}$$

Hence the dilution factor can be defined as the ratio of total gravitational energy of the suspension pendulum motion to the elastic energy stored in the wires.

2.3.2 Thermoelastic dissipation

Thermoelastic loss describes heat flow across thin flexing beams or fibres and was studied by Zener [76] and Norwick [77]. Thermoelastic loss arises in the fibres and mirrors [78] of the suspension system. In order to understand this phenomenon, consider a thin wire that is deflected; in such a system one side would be in a state of compression and the other in tension. This will lead to a rise in temperature on the side that is under compression while the other side under tension will cool due to the change in the internal energy. The thermal gradients developed will in turn lead to heat flow across the wire until thermal equilibrium is reached. The heat flow results in a loss which is frequency dependent and is related to the relaxation time (thermal time constant). In an un-deflected wire the local temperature fluctuation will cause motion of the wire. This is due to expansion or contraction resulting from the finite thermal expansion coefficient of the wire material. The expansion coefficient α can be expressed as,

$$\alpha = \frac{1}{L}\frac{dL}{dT}. \tag{2.22}$$

where L is the original length of the wire and dL/dT is the change in length with respect to temperature. The dimensions of the body, the thermal conductivity and specific heat capacity defines the characteristic frequency for the heat transfer. The characteristic frequency of a wire of circular cross section and diameter d, is given by [77, 79],

$$f_{char} = \frac{1}{2\pi\tau} = 2.16\frac{\kappa}{\rho C d^2}\ Hz. \tag{2.23}$$

Here κ is the thermal conductivity, C is the specific heat capacity, τ is the characteristic time, and ρ is the density of the wire material. The loss associated with the thermoelastic dissipation is given by,

$$\phi(\omega) = \Delta\frac{\omega\tau}{1+(\omega\tau)^2}, \tag{2.24}$$

where,

$$\Delta = \frac{Y\alpha^2 T}{\rho C}. \tag{2.25}$$

This assumes that the Young's modulus, Y, is temperature independent but this is not true for any material. Hence a parameter, β, called the elastic thermal coefficient, which is analogous to the thermal expansion coefficient, can be introduced,

$$\beta = \frac{1}{Y}\frac{dY}{dT}. \tag{2.26}$$

This elastic thermal coefficient will not lead to any contribution to thermal noise unless there is a static stress, σ (defined as T/area,where T is the tension), in the beam. To understand what happens in a situation where there is a static stress the case of a simple pendulum is considered. For a pendulum of length L the extension dL due to the thermal expansion coefficient is given by equation 2.22 as $dL = \alpha L dT$. However there is an equivalent change in length dL which results from the change in Young's modulus with temperature when the pendulum suspension fibre is under tension. The stress is related to the Young's modulus by,

$$\sigma = Y\left(\frac{dL}{L}\right) \tag{2.27}$$

or

$$dL = \left(\frac{\sigma L}{Y}\right). \tag{2.28}$$

Hence we can write,

$$\frac{dL}{dT} = \frac{-\sigma L}{Y^2}\frac{dY}{dT}, \tag{2.29}$$

or

$$\frac{1}{L}\frac{dL}{dT} = \frac{-\sigma}{Y^2}\frac{dY}{dT} \tag{2.30}$$

Thus for a temperature change dT, the extension due to the temperature coefficient of Young's modulus is,

$$dL = \frac{-\sigma L}{Y^2}\frac{dY}{dT}dT. \tag{2.31}$$

Thus the total extension for a temperature change dT, is,

$$dL_{total} = \alpha L dT - \frac{\sigma L}{Y^2}\frac{dY}{dT}dT. \tag{2.32}$$

Thus there is an effective 'coefficient of expansion' $\alpha' = \frac{1}{L}\frac{dL_{total}}{dT} = \left(\alpha - \frac{\sigma}{Y^2}\frac{dY}{dT}\right) = \left(\alpha - \frac{\sigma\beta}{Y}\right)$ and when thermoelastic noise is calculated this effective 'coefficient of expansion' should be used. Hence when considering the loss factor of suspension materials, the thermoelastic loss is finally given by,

$$\phi_{thermoelastic}(\omega) = \frac{YT}{\rho C}\left(\alpha - \frac{\sigma\beta}{Y}\right)^2 \frac{\omega\tau}{1+(\omega\tau)^2}, \tag{2.33}$$

where,

$$\Delta = \frac{YT}{\rho C}\left[\alpha - \frac{\sigma}{Y^2}\frac{dY}{dT}\right]^2 = \frac{YT}{\rho C}\left(\alpha - \frac{\sigma\beta}{Y}\right)^2. \tag{2.34}$$

The suspension fibres used in the aLIGO detector are 60 cm long, suspending a 40 kg silica test mass on four silica fibres. The fibres start from a stock of diameter 3 mm. The stock tapers down to 800 μm, which is the thermoelastic noise cancellation region estimated using $\left(\alpha - \frac{\sigma\beta}{Y}\right)$, as previously discussed. The diameter of the thermoelastic noise cancellation region is based on the static stress of 800 MPa in each fibre (load on each fibre is 10 kg). The 800 μm section finally tapers down to the thinnest section of the fibre which is 400 μm in diameter [48].

2.3.3 Surface loss, bulk loss and weld loss

The remaining loss terms are a combination of bulk loss [80], surface loss [81] and weld loss [12],

$$\phi_{fibre}(\omega) = \phi_{bulk}(\omega) + \phi_{surface} + \phi_{weld}, \tag{2.35}$$

where $\phi_{bulk\,loss}(\omega)$ is the frequency dependent loss in the body of the material, $\phi_{surface\,loss}$ is the frequency independent loss associated with any surface damage of fused silica samples due to absorbed contaminants or surface welds and $\phi_{weld\,loss}$ is the loss of the weld region of the fibres. The surface loss term can be described as [12, 81],

$$\phi_{surface} = \mu h \phi_s \frac{S}{V} = \mu h \phi_s \frac{2\pi r l}{\pi r^2 l} = \mu h \phi_s \frac{4}{d}, \tag{2.36}$$

where μ is a coefficient dependent of the geometry of the fibre (for a circular fibre $\mu \cong 2$), ϕ_s is the mechanical loss of the material surface and h is the depth over which surface loss occurs. The value of $h\phi_s$ is taken as 6.15×10^{-12} m from [81]. S is the surface area and V the volume. Hence for fibres of circular cross section and diameter d the surface loss is given by,

$$\phi_{surface} = \frac{8h\phi_s}{d}. \tag{2.37}$$

The bulk loss [80] and weld loss [12] terms are derived from measurements and are given by,

$$\phi_{bulk} = 7.6 \times 10^{-12} \left(\frac{\omega}{2\pi}\right)^{0.77}, \tag{2.38}$$

$$\phi_{weld} = 5.8 \times 10^{-7} \frac{E_i}{E_{total}}, \tag{2.39}$$

where ω is the angular frequency in equation (2.38) and E_i/E_{total} is the elastic energy ratio estimated from FEA, which is discussed in detail in the next section.

2.3.4 Estimating the mechanical loss using FEA

The total diluted mechanical loss along with the individual loss terms (thermoelastic, surface, bulk and weld loss) can be predicted using the Finite Element Analysis (FEA) package - ANSYS. This involves creating a FEA model of the suspension design, which is then solved to obtain the elastic (strain) energy due to bending of the fibre. A fibre is built a using certain numbers of elements (typical element density of 4 per mm for the

convergence of values). The schematic of a real fibre model, which is approximated to FEA model divided into number of elements, is shown in figure 2.3. In the FEA model, the strain energy stored in each element *i* of the fibre (while bending), is used to calculate the thermoelastic loss, surface loss, weld loss and the dilution factor. The estimation of the dilution factor requires additional information of the total kinetic energy stored in the pendulum (for the respective mode). The information from the FEA model is used to run a MATLAB script for estimating the individual loss term in each i^{th} element, which is then summed to give the total loss value as a function of frequency [82]. The details of the FEA modelling technique is discussed in the literature [83, 84].

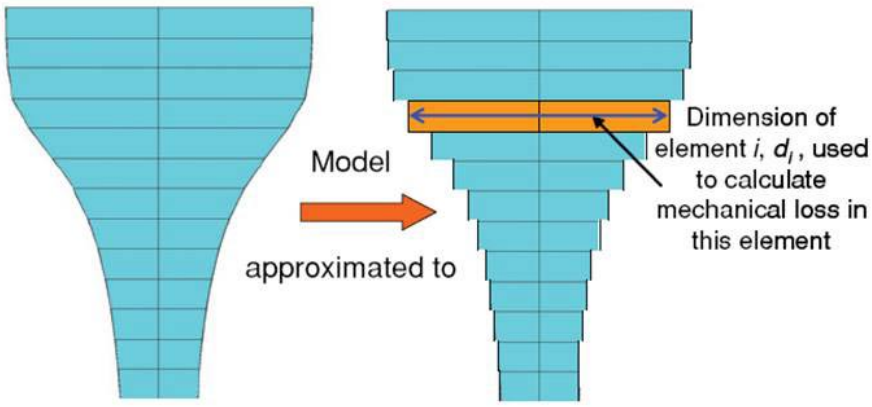

Figure 2.3 *FEA model of a fibre neck design divided into number of elements. The individual loss terms are estimated by integrating the values from each element i (figure courtesy of [84]).*

The mechanical loss for each element *i* in the fibre can be represented as,

$$\phi_i(\omega) = \frac{8h\phi_s}{d_i} + 7.6\times10^{-12}\left(\frac{\omega}{2\pi}\right)^{0.77} + \frac{YT}{\rho C}\left(\alpha - \sigma_i\frac{\beta}{Y}\right)^2\left(\frac{\omega\tau_i}{1+\omega^2\tau_i^2}\right) + 5.8\times10^{-7}\,\frac{E_i}{E_{total}}, \tag{2.40}$$

where E_i is the elastic energy stored in each element of the fibre, E_{total} is the total elastic energy, d_i is the average diameter of the fibre in the *i*th element. τ_i is the characteristic time for the heat to flow over diameter d_i and σ_i is the

static stress in the *i*th element. The total mechanical loss in the entire fibre can be calculated by using,

$$\phi_{total}(\omega) = \frac{1}{D}\left(\frac{E_1}{E_{total}}\phi_1(\omega) + \frac{E_2}{E_{total}}\phi_2(\omega) + \cdots + \frac{E_n}{E_{total}}\phi_n(\omega)\right), \qquad (2.41)$$

where and ϕ_i is mechanical loss in the i^{th} element of the fibre and there are n elements in the model: $i = 1,\ldots,n$. The FEA modelling techniques have been used to design and estimate the mechanical loss and suspension thermal noise of the GEO-HF and aLIGO suspension system, which is discussed ahead in chapter 3 and chapter 6 of this thesis.

2.4 Interferometer suspension thermal noise sources

In a low loss oscillator most of the thermal noise is located in the resonant modes: pendulum and violin modes. There are other resonant modes in a suspension that do not contribute significantly to the suspension thermal noise, for example: pitch mode, tilt mode and bounce mode.

2.4.1 Pendulum mode thermal noise

The pendulum mode thermal noise is due to the mechanical loss of the suspension material which suspends the test mass. The loss in the pendulum is related to the loss of the suspension material (fibre in this case) such that in general [36],

$$\phi_{pendulum}(\omega) \approx \phi_{fibre}(\omega)\frac{\xi n\sqrt{TYI}}{2mgL}. \qquad (2.42)$$

ξ equals 1 for a single fibre pendulum where the fibre is bending at the top [85]. If the fibres are constrained in such a way that allows bending at the top and bottom then ξ equals 2. The pendulum mode frequency is below the detection band of the instrument (due to seismic isolation) and this can be done by keeping the wires long and thin. The loss in the pendulum can be minimized via the effect of the dilution factor as the majority of energy is stored in the gravitational field and very little in wires. The thermal noise from the suspension system then depends on the loss factor arising from Brownian motion, thermoelastic dissipation and the dilution factor.

2.4.2 Violin mode thermal noise

The violin modes, also known as the transverse vibrational modes, of the suspension fibres form a harmonic series and lie within the detection band. The first violin mode will have a loss that is twice the loss associated with the pendulum mode [85, 86] because the dissipation dilution is half of the pendulum mode. The first violin mode loss can be expressed as,

$$\phi_{violin}(\omega) = 2\phi_{pendulum}(\omega). \tag{2.43}$$

As the suspension system is made up of low loss material, the thermal noise will be concentrated within a range of narrow frequencies around the resonance. This has motivated designs such as those used in the GEO 600 detector and the design for the Advanced LIGO detector.

2.5 Conclusions

Thermal noise is one of the most important areas limiting the sensitivity of the detectors and there are important issues with the designs of the suspension elements that require further study. This will help us to understand and optimise the designs of suspension elements of the future detectors. Using the fluctuation dissipation theorem one can estimate the thermal noise levels from the mechanical loss of the suspension elements. The mechanical loss is the inverse of the quality factor Q. The design of the gravitational wave detectors is such that it operates with a very high Q factor and low off-resonance thermal noise.

However, there are various sources of dissipation and need to be minimised to obtain a very high Q and low levels of thermal noise. The mirrors in the gravitational wave detector are in the form of multiple pendulums. The loss in the pendulum comes from the flexing of the wires and the material used for construction. Using a multiple pendulum system reduces seismic noise at low frequency, however using thin wires also helps in lowering the thermal noise by storing most of the energy in the non-dissipative gravitational field, which has been described as the dilution factor.

It is also important to design and optimise a system to lower the thermoelastic loss which arises from the flexing of the suspension fibres. This

is possible by choosing the value of stress in the suspension elements such that the overall thermoelastic loss is significantly reduced.

There are other loss terms such as bulk loss, surface loss and weld loss, which contribute to the total diluted mechanical loss. Using the techniques developed in FEA, these individual loss terms along with thermoelastic loss and the dilution factor can be predicted by estimating the elastic energy in each element of the fibre.

For improving the sensitivity of the detector it is possible to design a system where the thermal noise peaks are at a frequency away from the detection band. The work in this thesis involves evaluation of the mechanical loss and expected thermal noise of the suspension system.

Chapter 3 Thermal noise performance of a potential suspension upgrade for the GEO-HF detector

3.1 Introduction

A network of long baseline ground based interferometers has been built around the world for the first detection of gravitational waves signals. The German British GEO detector located near Hannover in Germany is one among the four interferometers used within the LSC (LIGO scientific collaboration) searching for gravitational waves [20, 87]. It has a shorter arm length (600 meters) as compared to the two LIGO detectors (4 km) in the USA and the VIRGO detector (3 km) in Pisa, Italy. KAGRA (3 km) in Japan is a cryogenic temperature detector and is currently under construction. The work in this chapter discusses the mechanical loss and thermal noise performance estimated for the suspension system of the GEO detector. Using new techniques, an optimised fibre design has been worked out for a possible repair scenario of the suspension system of the GEO detector. The procedure for the fabrication and welding of the monolithic fused silica suspension is also discussed.

3.2 GEO 600 monolithic suspension

The GEO 600 detector is based on a Michelson interferometer having an orthogonal arm length of 600 meters, which is folded once to obtain an effective arm length of 1200 meters. A 14 W Nd:YAG laser system is used as a light source and the interferometer employs power and signal recycling techniques [28]. The suspension mirror of the detector comprises of a triple pendulum system enclosed in an ultra-high vacuum system. The sensitivity

of the detector in terms of amplitude is 6.5×10^{-18} /√Hz at 50 Hz [88]. To achieve this sensitivity, a significant degree of seismic isolation has to be provided to the test mass in the horizontal and vertical direction. The vertical isolation is achieved by employing cantilever springs. The horizontal isolation is achieved through a triple pendulum system, which was designed to obtain a displacement sensitivity of ~2.4×10^{-20} m/√Hz at 50 Hz [55]. Figure 3.1 shows the quasi-monolithic fused silica suspension system consisting of a metal 'upper-mass' followed by a fused silica intermediate-mass and finally the lowermost fused silica test-mass. The intermediate mass hangs from the upper mass through a metal wire in a loop. The test mass is suspended using four silica fibres (two at each side) which are welded onto the fused silica ears (bonded to the sides of the test mass). Fused silica is an ideal suspension material because of an intrinsic mechanical loss of very low value (and hence high *Q)*. Fused silica can also be welded and pulled into thin fibres.

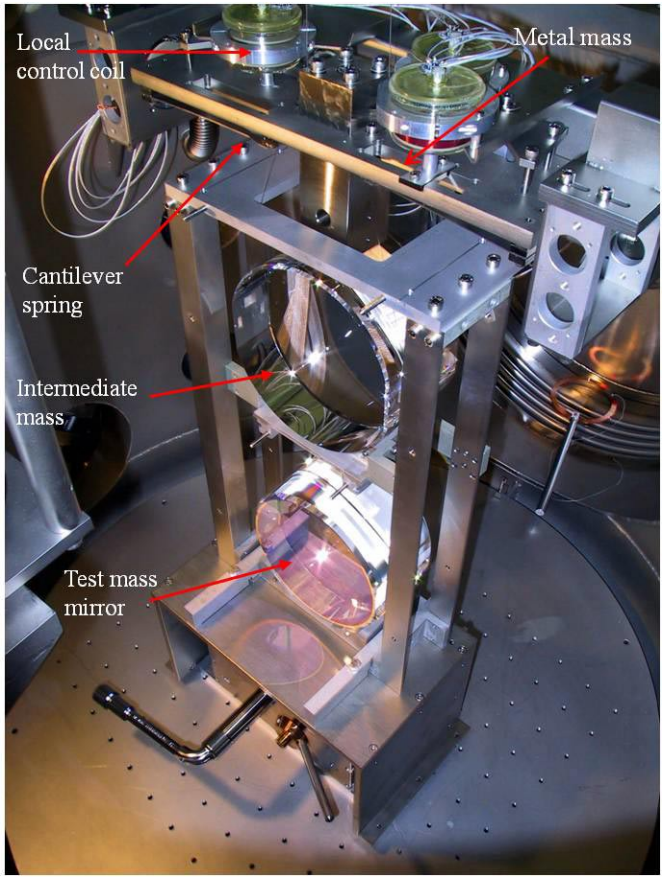

Figure 3.1 Monolithic suspension system of GEO 600 inside the vacuum tank [55]*. The fused silica intermediate mass is suspended from steel wire in a*

loop which is supported by metal cantilever springs, the silica test mass hangs on four fused silica fibres.

The schematic of the suspension system inside the vacuum tank is shown in figure 3.2. The triple pendulum system is suspended from cantilever blades made from maraging steel. To control the suspension a reaction mass is suspended as shown in the figure 3.2. An active and passive layer of a vibration isolation system helps in cancelling the seismic noise.

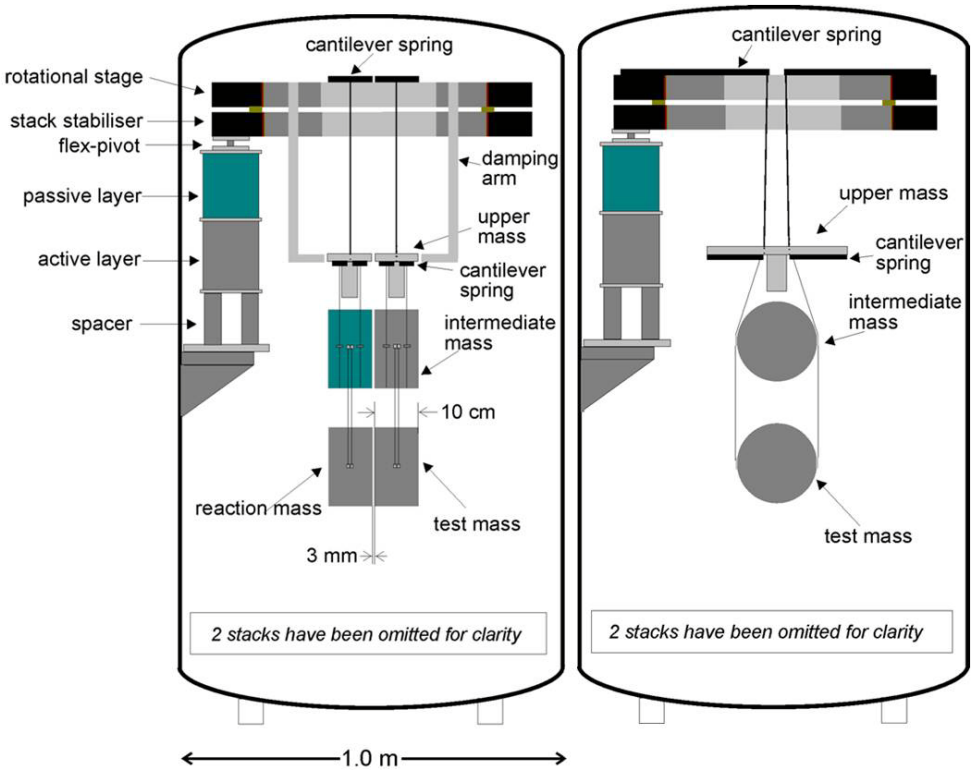

Figure 3.2 Schematic of the vibration-isolation of the suspension system used in the GEO detector. The triple pendulum is suspended from the cantilever springs [54].

The advanced technologies like signal recycling and the use of monolithic fused silica suspensions enables the GEO detector to achieve sensitivity close to the LIGO and VIRGO detectors. However the LIGO detectors are currently undergoing a major upgrade to Advanced LIGO, which includes a quadruple pendulum suspension system having monolithic fused silica at the lower most stage. The strategy thought out for the GEO detector has been to optimise it for higher frequencies to compliment the sensitivities of the Advanced LIGO and Advanced VIRGO detectors. Due to the limited

infrastructure in the case of GEO (shorter arm length), improvement in the sensitivity can only be achieved through the use of better optics and also by incorporating some new technologies [89], including squeezed light to reach the standard quantum limit [58]. The GEO 600 detector is undergoing an upgrade to make it a high frequency detector and has hence been named as the GEO–HF (high frequency) project [90]. Seismic noise is the dominant noise source below 50 Hz and currently there are no plans for further improvement. The planned upgrade of the GEO detector requires access to the vacuum tanks enclosing the triple pendulum suspension system. As a result there is a possibility that there could be damage to the suspension fibres suspending the test mass, hence a repair scenario has been worked out in Glasgow. This will reduce the downtime of the detector in case the suspension fibre breaks. The possible repair scenario also gives us the opportunity to re-design the suspension fibres, incorporating up to date technologies developed for aLIGO. The new suspension fibres are designed to improve the control of the suspension by ensuring better constrained modal frequencies and suspension dynamics. The new fibres will also give a better control over the violin mode frequency as the original GEO fibres have a violin mode frequency spread of around 20 Hz. The new fibres will be laser-pulled and will be highly reproducible with a precise control over their geometry.

3.2.1 Original GEO fibre design

The fused silica fibres used in the GEO suspension were originally designed by considering the pendulum mode, vertical bounce mode and the fundamental violin mode frequency. The design specification required the pendulum mode to be 1 Hz and the bounce mode frequency around 15 Hz. The resonant frequency for the fundamental violin mode was kept around 650 Hz. Hence very thin fused silica fibres of diameter 220 micron and length 280 mm were thought to be suitable [53]. Figure 3.3 shows the schematic of the original fibre design along with the photograph of the original fused silica fibre. To characterise the dimensions of the original fibre, a fused silica fibre was shipped in a fibre transport tube from the GEO site in Germany to Glasgow. The silica fibres were originally fabricated by heating a silica rod (5 mm in diameter) using a hydrogen-oxygen flame-pulling machine. These fibres have a longer neck due to the flame pulling technique, ranging from 3 cm to 4 cm in length as shown in figure 3.3. The

fabricated fibres have an excess stock region for clamping purposes. The excess stock (~5 mm section), is chopped off using diamond tip cutters roughly at a point where the cross sectional diameter of the tapering neck is 2 mm. The fibres are welded to the silica ears using the hydrogen-oxygen flame welding technique. To fabricate a suspension, four silica fibres suspend a 5.6 kg silica test mass. The test mass has silica ears bonded [91] to the flat surface on both the sides. The original GEO fibres have low reproducibility due to the flame pulling technique, which lacks precise control. Flame pulling requires several 10's of silica fibres to be fabricated before selecting the right fibre based on the measured violin mode frequencies [57]. However, even then they have significant variation in the neck geometry and bending point thus making it difficult to control the suspension as it suffers from internal mode coupling and a wide spread in the violin mode frequencies.

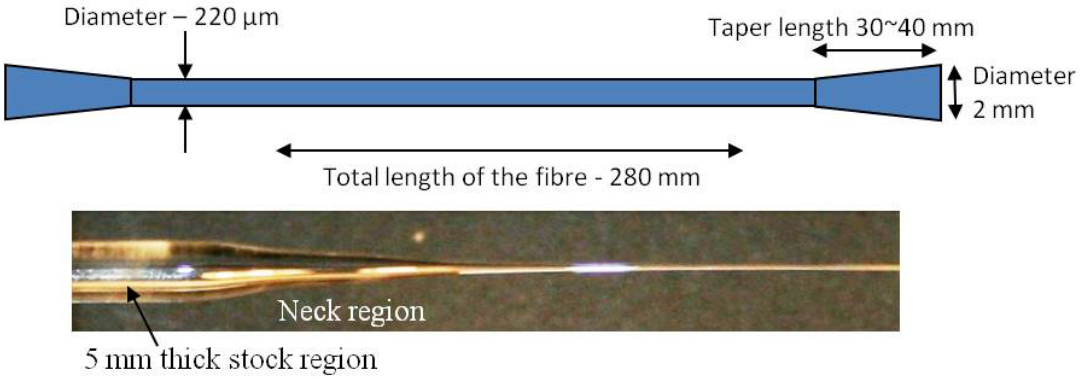

Figure 3.3 Schematic of the original fibre design used in the GEO 600 suspension. The photograph at the bottom shows the original GEO fibre (flame pulled) used in the suspension.

3.2.2 Suspension fibre re-design

The new silica fibres for a possible repair scenario were designed for the fundamental violin mode to resonate above 1 kHz and to include thermoelastic noise cancellation properties (discussed in chapter 2) as utilised in the advanced LIGO dumbbell fibres [92]. Since the load on each silica fibre will be 1.4 kg (5.6 kg for four fibres), the resulting stress of 800 MPa will be identical to the stress in the advanced LIGO fibres [93].
The new fibre design will be referred to as an optimised GEO fibre in this thesis. Figure 3.4 shows a schematic of the 280 mm long silica fibre design

having varying cross sections. A silica rod (also called stock) of diameter 2 mm will be used to fabricate the fibre, using the CO_2 laser pulling machine setup in Glasgow. The fabrication of silica fibres is discussed in section 3.5. The 2 mm stock will be 10 mm long and will taper down to a diameter of 300 μm thermoelastic noise [92] cancellation region. The diameter of thermoelastic noise cancellation is estimated using the following equation,

$$d_{null} = 2 \times \sqrt{\frac{T\beta}{\pi Y \alpha}} = 2 \times \sqrt{\frac{13.75 \times 1.52 \times 10^{-4}}{\pi \times 7.2 \times 10^{10} \times 3.90 \times 10^{-7}}} \approx 300 \times 10^{-6} m,$$

where T is the tension in the fibre, β is the elastic thermal coefficient, Y is the Young's modulus and α is the coefficient of thermal expansion. The 300 μm will then transition to 150 μm, and form the thinnest section of the fibre. These silica fibres will have very short necks as shown in the figure 3.4. The neck length can vary between 5 mm to 10 mm. Short neck length is vital for keeping the bending point of the fibre close to the centre of gravity of the suspended test mass. This results in better control of the suspension by reducing the mode frequency coupling. The new fibres will give a violin mode spread of less than 1 Hz and this is possible due to the precise geometry and reproducibility of the fibres.

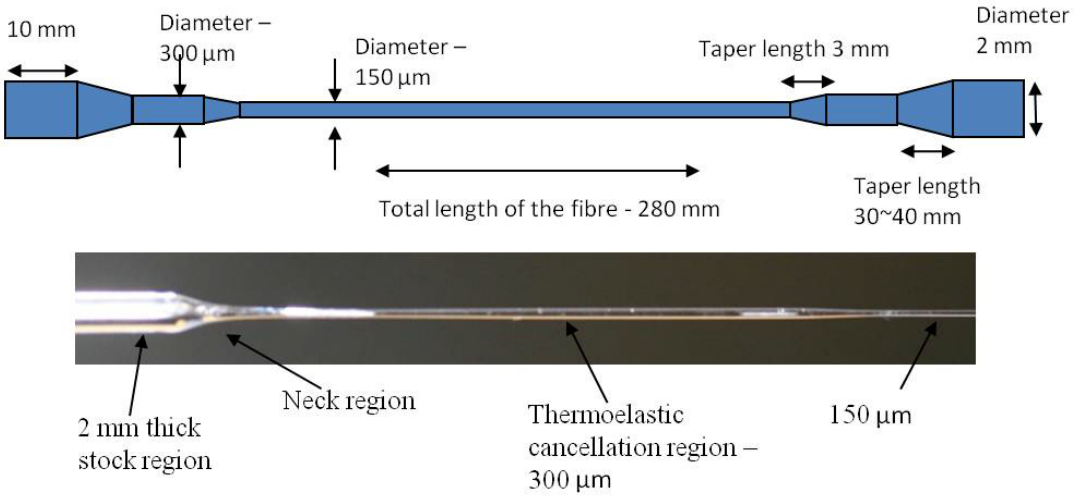

Figure 3.4 Schematic of the optimised fibre for the GEO suspension. The photograph is a real silica fibre fabricated using the CO_2 laser pulling machine set-up in Glasgow.

3.3 Finite element analysis (FEA)

Finite Element Analysis (ANSYS) was used to study the distribution of elastic energy in the fibres and ultimately the thermal noise performance of the GEO suspension. The FEA model is a dense mesh of elements. A typical mesh density in a fibre design is 4 elements per mm to obtain convergence to a level within 1% of difference. Energy is stored in each element as an elastic potential energy as the fibre bends and the swinging of the pendulum gives the total kinetic energy. The dissipation dilution factor can be estimated by taking the ratio of the total elastic energy and the total kinetic energy in the system. The thermoelastic loss, surface loss and weld loss calculations can also be determined using the elastic energy distribution in the system [82].

The ANSYS model of the lowermost stage of the GEO suspension is shown in figure 3.5. The model consists of four silica fibres suspending a 5.6 kg silica test mass and bonded silica ears. Material properties of fused silica are as follows: a density of 2202 kg/m^3, a Young's modulus of 7.2×10^{10} N/m^2 and a Poisson's ratio of 0.17 [94]. To analyse the performance of the fibres three different ANSYS model were built. The first model had four original GEO fibres (as described in section 3.2.1) suspending the 5.6 kg test mass. Figure 3.6(a) shows the ANSYS model of the original GEO fibre having a linear tapered neck. The linear tapered neck replicates the neck region as seen in the real fibre (figure 3.3). The second model consisted of four optimised fibres (as discussed in section 3.2.2) suspending the silica test mass. The third model was a special case of the second model, where an ideal design was built using the optimised fibres. The ANSYS model of the optimised GEO fibre is shown in figure 3.6(b).

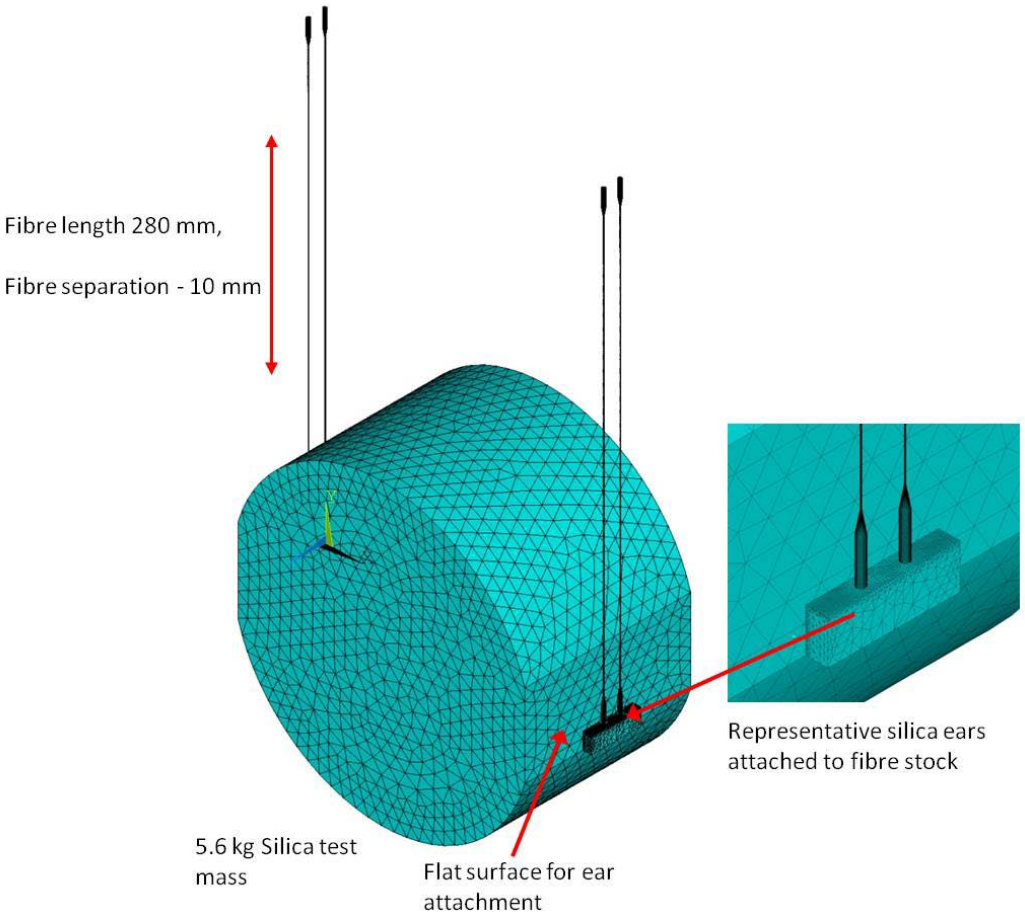

Figure 3.5 ANSYS model of the final stage of the monolithic GEO suspension system. The finely meshed solid mass is suspended from four fused silica fibres, The FEA model used beam elements for designing the silica fibres and solid elements for the test mass/ears.

The position of the ears on the flat surface of the mass was kept 1 mm below the centre of gravity of the test mass. This is in accordance with the original baseline design used for the GEO suspension in Germany. The free end of the fibres is constrained for rotational and translational degrees of freedom. Inertial conditions such as gravity were applied and the model was solved for a *static* analysis. A static analysis takes into account the loading conditions applied and then estimates the static displacement values. The pre-stress effect from the static analysis is then used for solving the modal analysis to obtain the resonant mode frequencies [83]. Table 3.1 shows the pendulum mode, bounce mode and fundamental violin mode frequencies estimated using FEA for the original fibre and the optimised fibre design. By reducing the thickness of the fibre in the optimised design, the stress is

increased and this helps to achieve a lower vertical bounce mode frequency and higher violin mode frequencies.

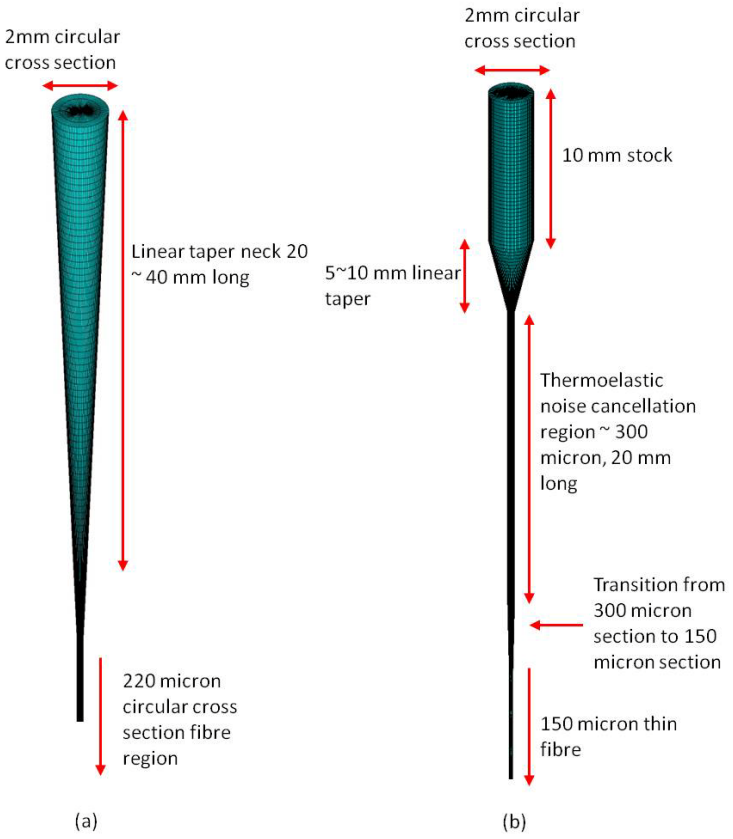

Figure 3.6 (a) ANSYS model of the original GEO fibre, (b) ANSYS model of the optimised GEO fibre.

Mode shape	Original fibre (FEA), Hz	Optimised fibre (FEA), Hz.
Pendulum mode	0.983	0.971
Bounce mode	14.02	10.427
Fundamental violin mode	657	1161

Table 3.1 Resonant mode frequencies estimated using FEA models for the final stage of the GEO suspension system.

3.3.1 Elastic energy in the fibre

Original GEO fibre

The elastic energy (referred to as strain energy in ANSYS) stored in each element of the fibre is obtained from FEA (as discussed in chapter 2, section 2.3.4) and is plotted as function of length. The strain energy values measured in ANSYS is of arbitrary units and the values are normalised by dividing them with the total strain energy in the body or the total kinetic energy. This normalised value can then be used for the estimation of dissipation dilution or mechanical loss. Figure 3.7 shows the energy distribution in the original GEO fibre for the pendulum mode frequency. The elastic energy peaks at the tapered neck region and the fibre bends more at the top end and less at the bottom. The top neck contains 23% of the total energy whereas 8% is stored in the bottom neck. The thinnest section (220 micron) of the fibre contains 58% of the total energy, which is high when compared to the energy in the neck region. Such a scenario will negatively affect the value of the dissipation dilution factor of the suspension. An essential feature of the suspension design is to have most of the energy stored in the neck region to achieve a higher dilution, resulting in a lower mechanical loss.

Due to the use of longer neck in the original GEO fibre the flexure point of the fibre, estimated from FEA is 14 mm above the centre of gravity of the test mass. This results in the pendulum mode strongly coupling with the pitch mode leading to an unequal distribution of energy at the ends of the fibre. The test mass contains 11% of the total energy. The dual effect of mode coupling and unequal distribution of energy in the fibre have a profound effect on the dissipation dilution factor of the pendulum, which is calculated to be 32.23.

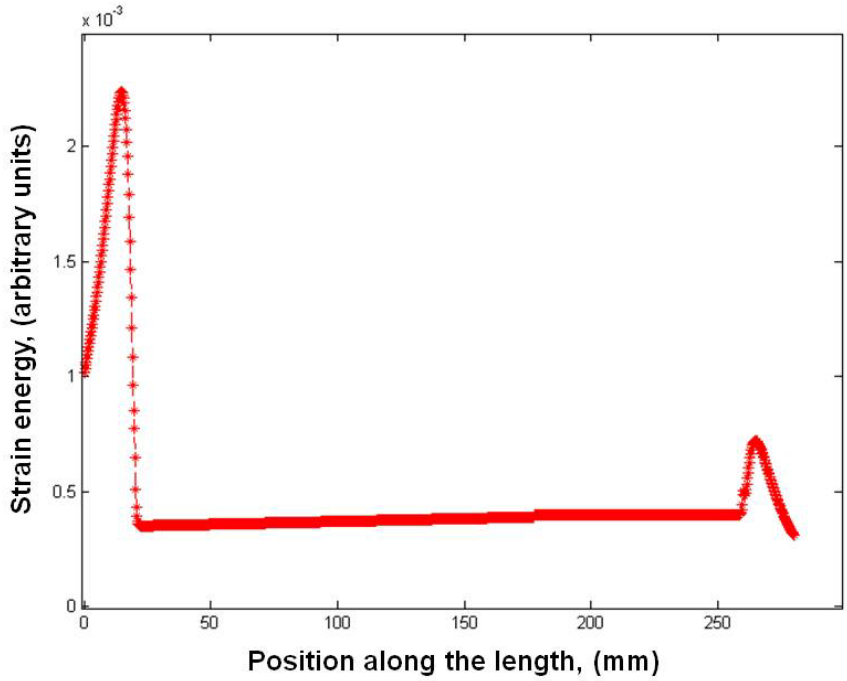

Figure 3.7 Energy distribution in the pendulum mode of the original GEO suspension fibres.

Optimised GEO fibre

The energy distribution in the optimised fibre is shown in the figure 3.8(a). The reader should be careful before comparing the absolute values of the strain energy given in figure 3.6 and figure 3.7. As mentioned before, since the values needs to be normalised hence initially they are only compared for their distribution along the length of the fibre. The flexure point of the optimised fibre is 16 mm above the centre of gravity of the test mass. The flexure point of the optimised fibre is higher than the original fibre due to the resistance offered by the stiffer stock (3 mm) while bending, as seen in the figure 3.8(a). Hence most of the bending starts after the 10 mm long stock region. The strain energy distribution in the fibre shows that most of the bending occurs only at the top neck region, while the bottom end does not show any form of bending. This is due to the incorrect position of the flexure point of the fibre due to the fixed ear position, which is causing only the top neck to bend. A significant amount of energy is distributed along the length of the optimised fibre, which was also seen in the original fibre case. Since the flexure point of the fibre is away from the centre of gravity

of the mass, it leads to mode coupling and the test mass tends to pitch (tilt) and this effect is discussed further in the document [83, 95]. To ameliorate this effect a third FEA model was designed where the flexure point is correctly positioned and is discussed next in an ideal design scenario case.

Ideal scenario for the optimised fibre

A third FEA model was built using the optimised fibre to envisage an ideal design scenario. The thermoelastic loss cancellation region in this fibre is 5 mm longer than the optimised fibre (while the total length of the fibre still being 280 mm). This case will be further referred as '*ideal design*' in this thesis. The reason behind calling this as an ideal design is because of the ear position in this model which has been changed such that the 'flexure point' of the fibre is brought nearer to the centre of gravity of the test mass. However in a real scenario the ear position cannot be changed as they are permanently bonded to the test mass. FEA modelling gives us an option to envisage a best possible design, which can be used as reference for future detectors.

The strain energy distribution for the ideal design is shown in figure 3.8(b). This design gives a better stability to the entire system as the mode frequency coupling is now reduced and the suspension fibres are bending as desired. The two ends of the fibre contain almost equal amounts of the elastic energy and the energy in the thinnest section (centre) is almost negligible. If the energy in the top cross section of the fibre is studied then we find that the stock contains 15% of the total energy, the neck has 12% and the thermoelastic region contains 22% of the energy.

Together the top and bottom end of the fibre contains 98% of the total strain energy while the remaining energy is distributed uniformly along the length of the fibre. The dissipation dilution factor D was then estimated using the ratio of the total strain energy and the kinetic energy of the system [82, 83]. Table 3.2 shows the dissipation dilution estimated for all the three cases modelled for the GEO suspension. For the ideal design, keeping the fibre flexure point position closer to the centre of gravity of the test mass helps the fibre to bend at both the ends almost equally and hence improves the dissipation dilution by more than a factor of ~4.

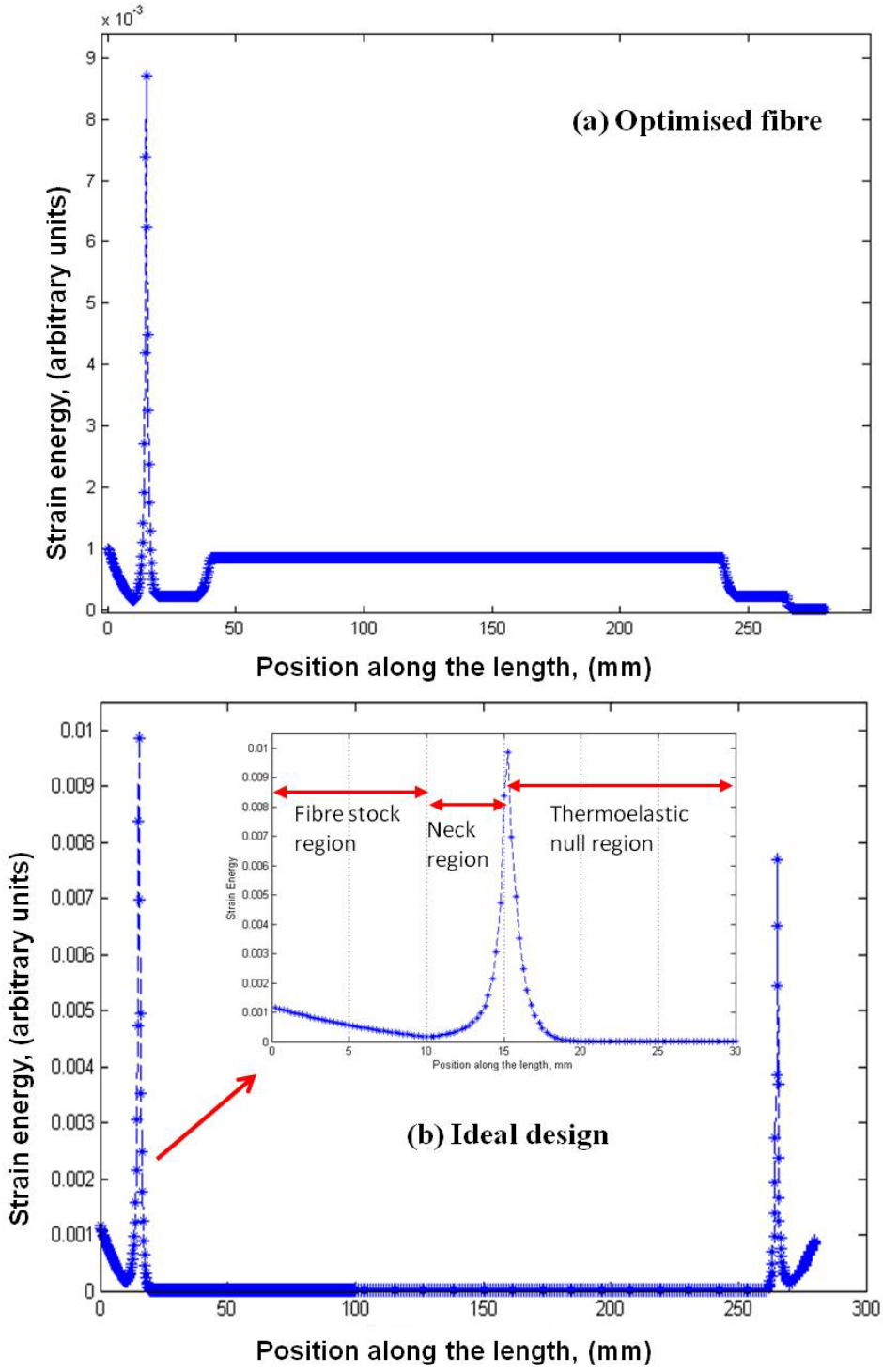

Figure 3.8 Comparison of the energy distribution between the optimised fibre and the ideal design. (a) Optimised fibre having the flexure point 16 mm above the centre of gravity of the test mass. (b) Ideal design having flexure point 1 mm above the cog of the test mass.

FEA Model	Dissipation Dilution
GEO fibre (original design)	32.23
Optimised GEO fibre	22.5
Ideal design	95.74

Table 3.2 Comparison of the dissipation dilution estimated using FEA for the GEO suspension.

3.4 Estimation of the mechanical loss and thermal noise

The mechanical loss as a function of frequency was estimated using the elastic energy distribution from the FEA model of the final stage of the GEO suspension, as outlined in chapter 2. Figure 3.9 shows the thermoelastic, bulk, surface and weld loss individually over a range of frequencies for the three FEA models. In the original GEO fibre the thermoelastic loss dominates (peaks value of ~ 2.32×10^{-8} at 40 Hz) the other loss terms over the entire spectrum of frequency as shown in figure 3.9(a). Comparing the original fibre with the performance of the optimised fibre, we find that the thermoelastic loss (peak ~1×10^{-8}) is cancelled above 5 Hz and is then dominated by the surface loss, as shown in figure 3.9(b). This is due to the 300 μm section of the optimised fibre which causes the thermoelastic peak at ~0.5 Hz. However for the ideal design in figure 3.9(c), the thermoelastic loss peak is lower (~3.5×10^{-9}) and is dominated by the surface loss at ~10 Hz. The total mechanical loss for all the above three cases is shown in figure 3.9(d) which includes the dissipation dilution factor, given in table 3.2. The bump seen for all the three cases signifies the thermoelastic loss peak. The mechanical loss in the original GEO fibre peaks at ~40 Hz whereas for the optimised fibre and the ideal design case the peak is seen at ~0.5 Hz.

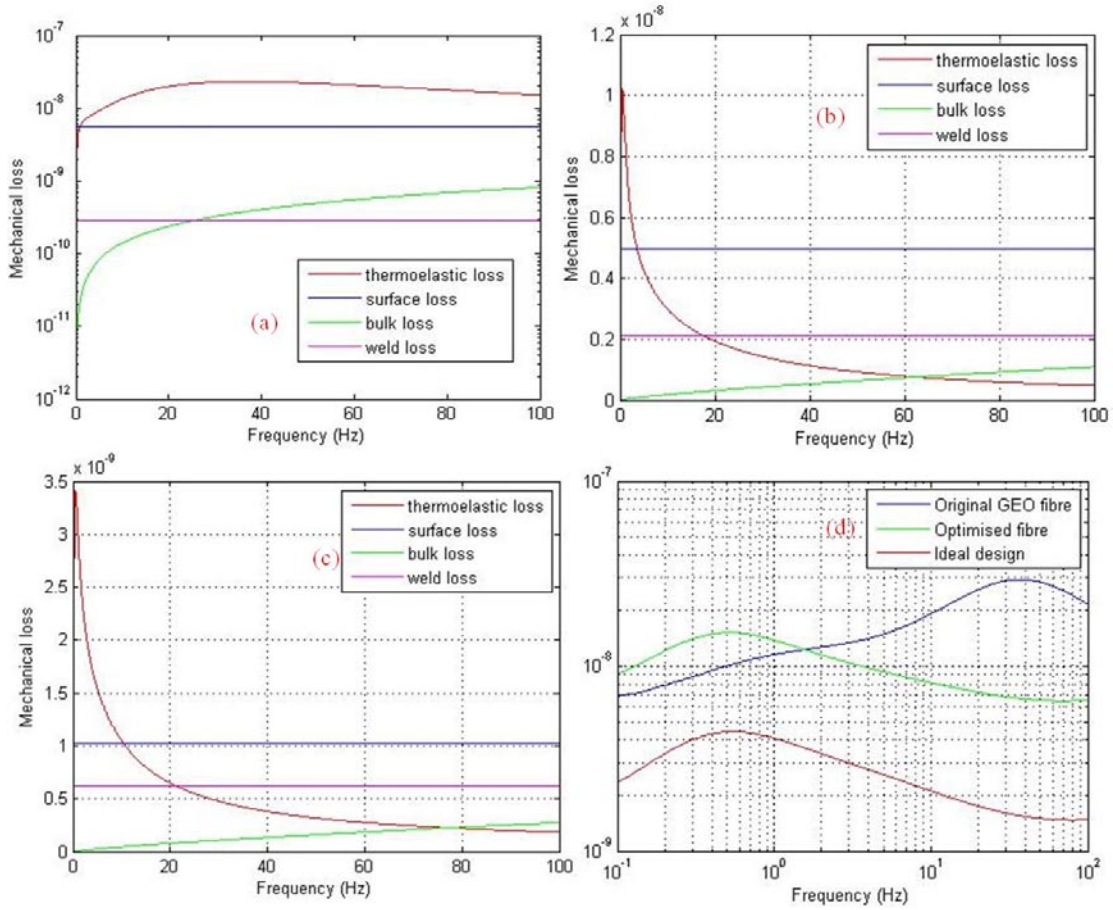

Figure 3.9 Plot of Mechanical loss as a function of frequency for the pendulum mode of the GEO suspension. (a) original GEO fibre, (b) optimised fibre, (c) Ideal design, (d) total (includes dilution factor) mechanical loss comparison.

The working frequency of the GEO detector is above 50 Hz as it is dominated by seismic noise below this frequency. The mechanical loss for the suspension having the original fibre design is estimated to be 2.84×10^{-8} at 50 Hz. At the same frequency the mechnical loss for the optimised fibre is 6.55×10^{-9} which is a factor of four improvement. However maximum gain may be obtained in the case of the ideal design which has the estimated mechanical loss of 1.50×10^{-9}.

Using the mechanical loss values, the suspension thermal noise was estimated using the power spectral displacement equation discussed in chapter 2. Figure 3.10 shows the thermal displacement noise as a function of

frequency, estimated for the GEO suspension comparing the performance of three different designs having: original GEO fibre, optimised fibre, ideal design.

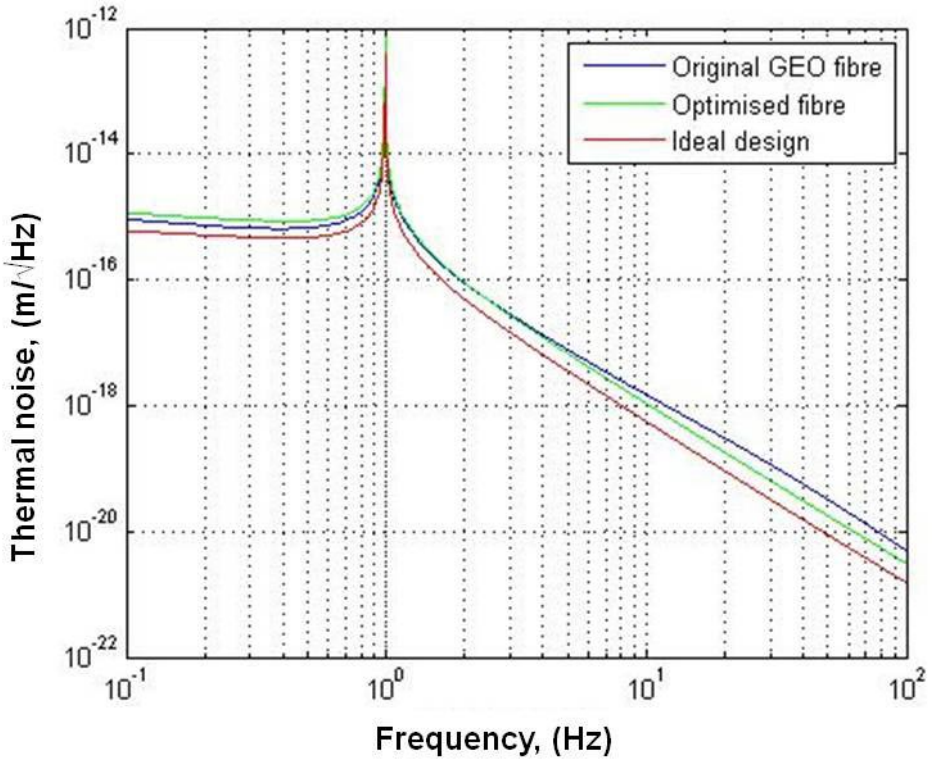

Figure 3.10 Thermal displacement noise as a function of frequency estimated for the GEO suspension. The noise is comapred for three suspension designs having: the original GEO fibre, the optimised fibre and the ideal design case.

At 50 Hz. the original fibre gives a thermal displacement noise of 3.28×10^{-20} m/√Hz. The optimised fibre design gives a factor of ~1.8 improvement, having a thermal displacement noise of 1.80×10^{-20} m/√Hz. The ideal design case shows an improvement by a factor of ~3.67 with an estimated thermal noise of 8.938×10^{-21} m/√Hz. The strain sensitivity (estimated by dividing the thermal noise by 1200, which is the length of the interferometer) calculated for the GEO suspension and the measured sensitivity of the GEO detector during the 5th science run is shown in figure 3.11. At 50 Hz the calculated strain sensitivity is 2.73×10^{-23} /√Hz which is much lower than the measured

sensitivity of 6.52×10^{-18} /√Hz [96], which suggests that it is being dominated by other non-thermal noise sources such as noise from the electronics or from the cross coupling of resonant modes from non-uniform bending points of the fibre. Other noise sources such as coating thermal noise and Quantum noise could also be dominating the suspension thermal noise at frequencies above 50 Hz.

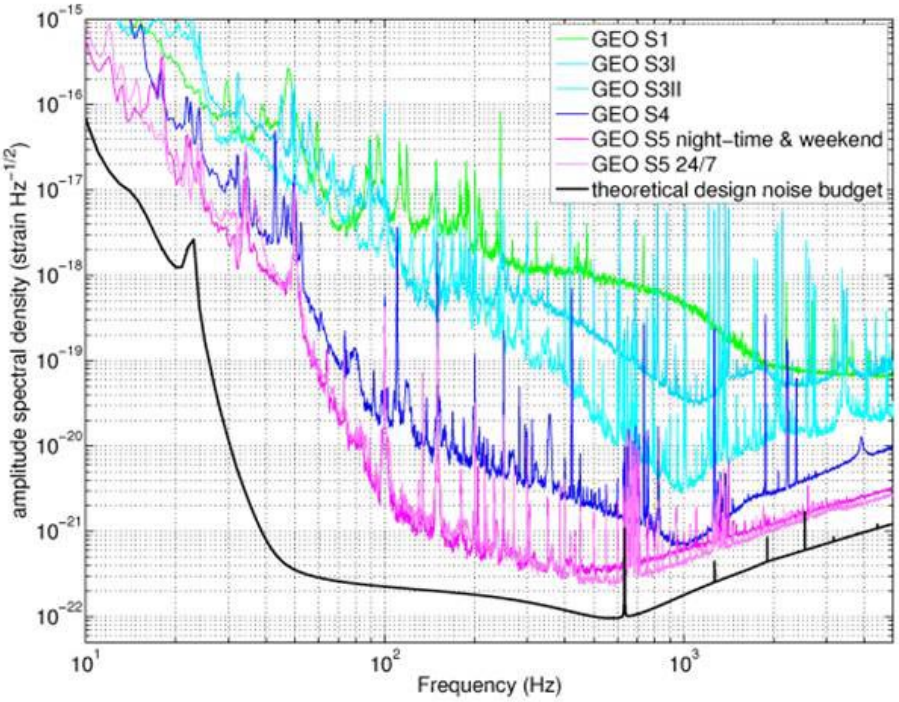

Figure 3.11 Amplitude spectral density of the GEO detector showing the sensitivity improvements over various science runs.

3.5 Fabrication of the GEO-HF monolithic silica suspension

3.5.1 Fabrication of fused silica fibres

The fibres for the redesigned GEO silica suspension will be fabricated using the 100 W CO_2 laser pulling machine set up in Glasgow as shown in figure 3.12. The CO_2 laser pulling machine works on the concept of feed and pull. The design and performance of the pulling machine is discussed in [97]. A fibre is fabricated from a silica rod (stock) of diameter 2 mm and 10 cm long. The ratio of feed and pull speed controls the diameter ratio between

the drawn silica fibre and the stock material. By accurately varying the feed pull ratio, precisely controlled fibre/neck shapes can be produced.

Before clamping the silica rod in the pulling machine it is first cleaned with methanol and then acetone to remove any surface impurities. Another wipe of methanol is given once the rod is clamped in the machine. The rod then undergoes laser polishing, which increases the strength of the fabricated fibre by healing surface cracks. Laser polishing involves heating up of the rod until it softens which is then recast once cooled. This process removes any micro cracks present in the stock and thus improves the strength of the fibre. The fabrication procedure is discussed in detail in the literature [98].

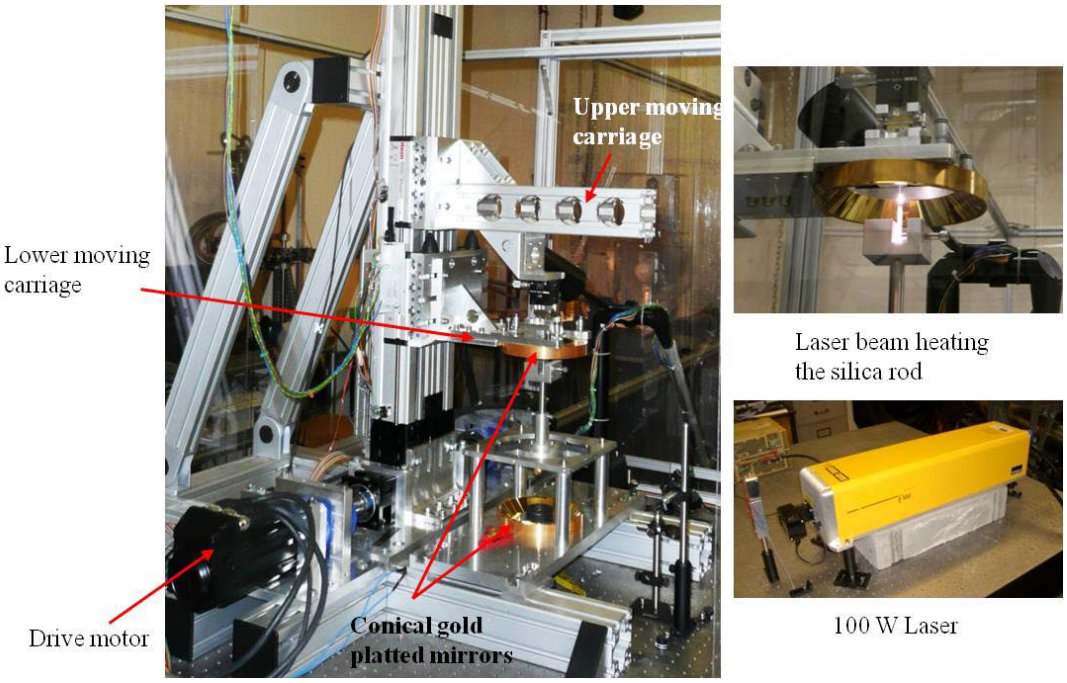

Figure 3.12 CO_2 laser pulling machine used for the fabrication of thin silica fibres of circular cross sections, in Glasgow.

3.5.2 Strength testing of the fibres

The laser pulled silica fibres were measured for their strength through destructive testing. A strength-testing machine was used for this purpose. The fibres to be tested are clamped in the strength tester and the tension in the fibre is gradually increased using drive motors, until the silica fibres breaks. The tension in the fibre is measured via a load cell attached to the

set-up. The silica fibres gave an average breaking stress of 4.08±0.05 GPa (±0.05 is the statistical error), which gives a factor of safety of 5 as the stress on each fibre is around 800 MPa. Once pulled, a fabricated fibre is first proof tested by loading a mass of 2 kg for five minutes to eliminate any damaged or weak fibres. The fibres are then stored in special cabinets, in order to protect them from dust and humidity. The fibres are pulled and stored in Glasgow and can then be shipped in a container to the GEO site in Germany for welding. A special cylindrical container was designed to store and transport the fibre as shown in figure 3.13. A fibre was shipped to Germany and back to Glasgow to test the durability of the container. A strength test was performed on this fibre and the results suggested that the integrity of the fibre was not compromised. Before using a fibre for cutting/welding a second proof test is performed on the stored fibres to eliminate touched or damaged ones.

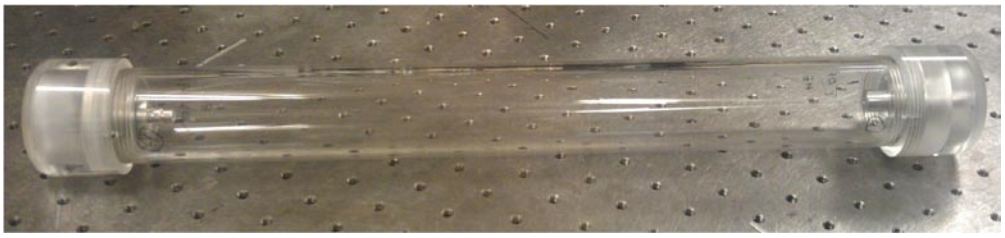

Figure 3.13 Transport tube used for shipping the silica fibres to the GEO site in Germany.

3.5.3 Welding procedure

The repair scenario of the suspension system will involve welding of the silica fibres to silica ears using a hydrogen-oxygen torch, which is a standard GEO welding technique. CO_2 laser welding [99] which has been developed for the suspension system of the advanced LIGO detector cannot be incorporated due to lack of laser welding facilities at the GEO site. However the design of the tools to be used for the welding is a scaled down version of the tooling used for the fabrication of the advanced LIGO suspension system [99]. The fabricated fibres have a long stock used for clamping into the pulling machine, hence a fibre cutter is used to resize the stock length according to the requirement (10 mm in this case). The tooling includes a fibre cutter module, ceramic tip fibre holder and a three axis moving stage.

Figure 3.14(a) shows the fibre holder and the fibre cutter set-up. A proof tested fibre is placed between the metal clamps and the distance between the clamps is adjusted to suit the length of the fibre (28.5 cm for GEO). The fibre holder's ceramic end is then used to grasp the stock as shown in fibre 3.14(b). The fibre holder has a set of zirconia (ceramic) tipped tweezers to clamp the stock of the fibre. A diamond tipped scribe is used to cut and break-off the excess stock. Figure 3.14(b) shows the resized silica fibre stock region, held by tweezers. Figure 3.15 shows the metal prototype of the GEO suspension along with the fibre holder attached, to be used for welding and testing.

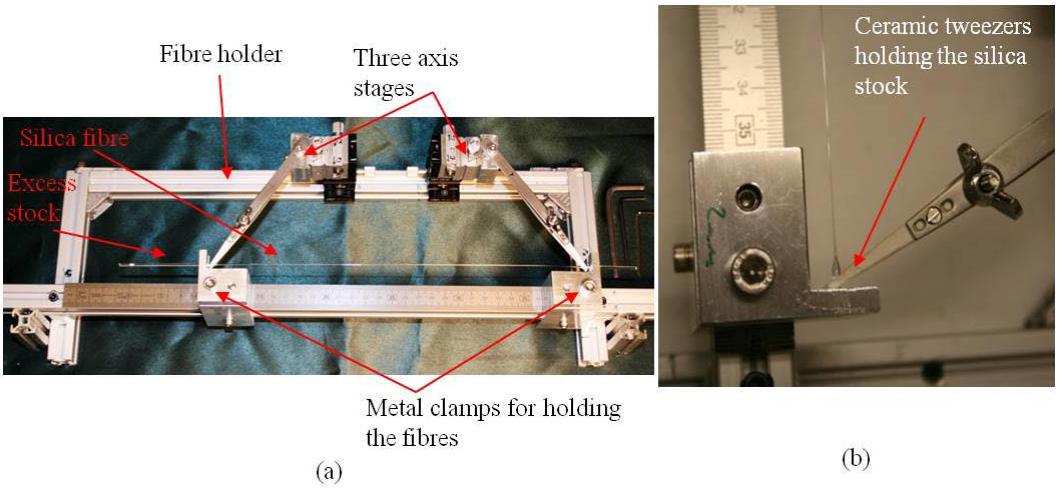

Figure 3.14 (a) Fibre cutter and holder setup used for cutting the excess stock, using a diamond tipped scribe. The fibre holder is also used for transporting the fibre to the suspension. (b) resized fibre clamped by the tweezers.

The fibre can then be transported using the fibre holder and then attached to the metal frame of the suspension. The position of fibre holder is carefully adjusted within the metal frame until the fibre stock is aligned to the silica ear. The three-axes stage in the fibre holder can be adjusted in the 'xyz' directions such that the silica fibre is at a perfect alignment with the flat tip of the horns of the silica ear. One end of the fibre is aligned with the ear and the remainder of the fibre is relaxed (while making sure that the fibre doesn't touch any part of the metal frame).

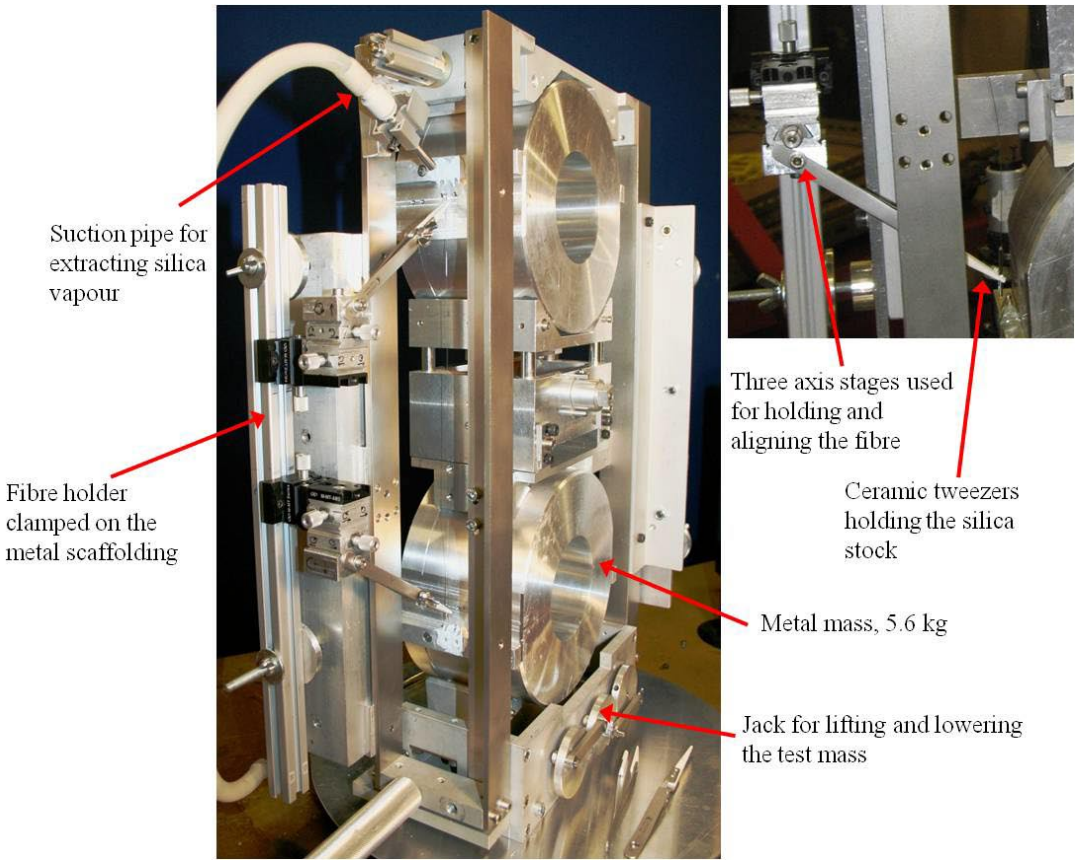

Figure 3.15 Metal prototype of the GEO suspension setup for welding. The fibre holder is attached to the metal frame of the suspension and the three-axes stage is used for positioning the fibre.

The electrolytic burner (*Aquarius-200*) is then used to heat the fibre stock region and the horns of the silica ear until molten. The molten stock is then fed into the silica horns to fuse them together. The high viscosity of fused silica allows the welding to be possible as the molten glass does not flow and thus maintains shape. The other end of the fibre is welded in a similar fashion. The weld region is roughly 2 mm long on each end and is precisely accounted for while initially cutting the fibre stock. Figure 3.16 shows the flame welding of the silica fibres. The silica vapour produced while welding is extracted using a suction pipe and HEPA filtered vacuum cleaner, and is prevented from depositing on the surface of the silica fibre. The vapour can damage the surface of the fibre and potentially increase the surface loss [100]. The weld and the stock region are finally annealed using the flame. Annealing helps in de-stressing or removing any misalignment between the stock and the ear horns. This is achieved by slowly heating the horns after

putting the fibres under small amount of tension by lowering the mass. This is done until the welded stock is well aligned with the ear horns. The metal frame caging the suspension has an inbuilt jack to slowly release the mass, which is then suspended on four silica fibres. The silica fibres welded to the two horns of GEO ear are shown in figure 3.16.

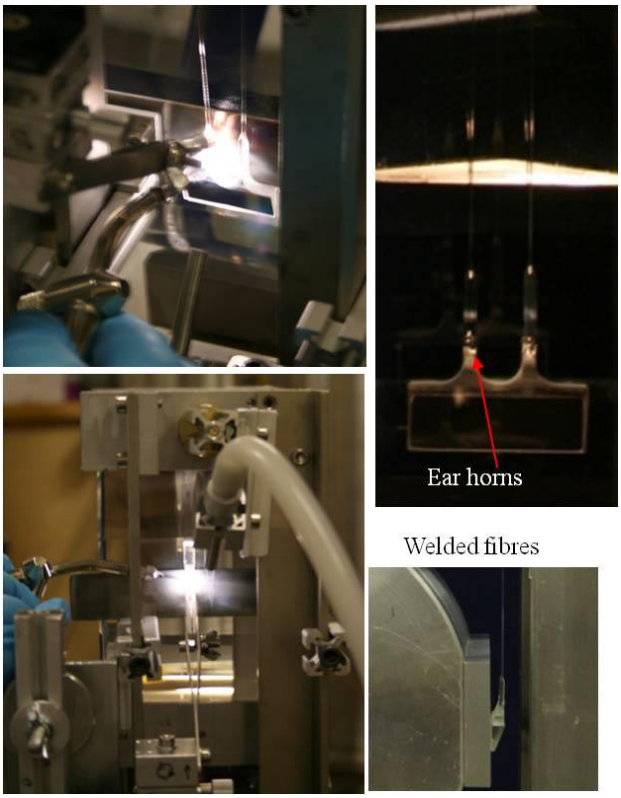

Figure 3.16 Flame welding of the silica fibres. The welded fibres can be seen on the right.

Initially three prototype test hangs involving metal masses and fused silica fibres/ears were successfully built. The outer dimensions of the metal mass used were identical to the silica test mass in GEO. The test hang had silica ears bonded to a metal disk using epoxy (epoxy was used only for the case of the prototype test hang) and were then attached to the sides of the metal masses.

A monolthic suspension involving polished fused silica masses and silica fibres was then fabricated in 2011. In this case silica ears were bonded to the flat sides of silica masses (both test mass and intermediate mass) using the hydroxide-catalysis bonding technique [101, 102]. The bonds were cured for

4 weeks before use. A metal heat shield was used to protect the silica mass from the flame while welding the fibres. Figure 3.17 shows the fabricated monolithic fused silica suspension, employing four silica fibres welded to the silica ears at the sides.

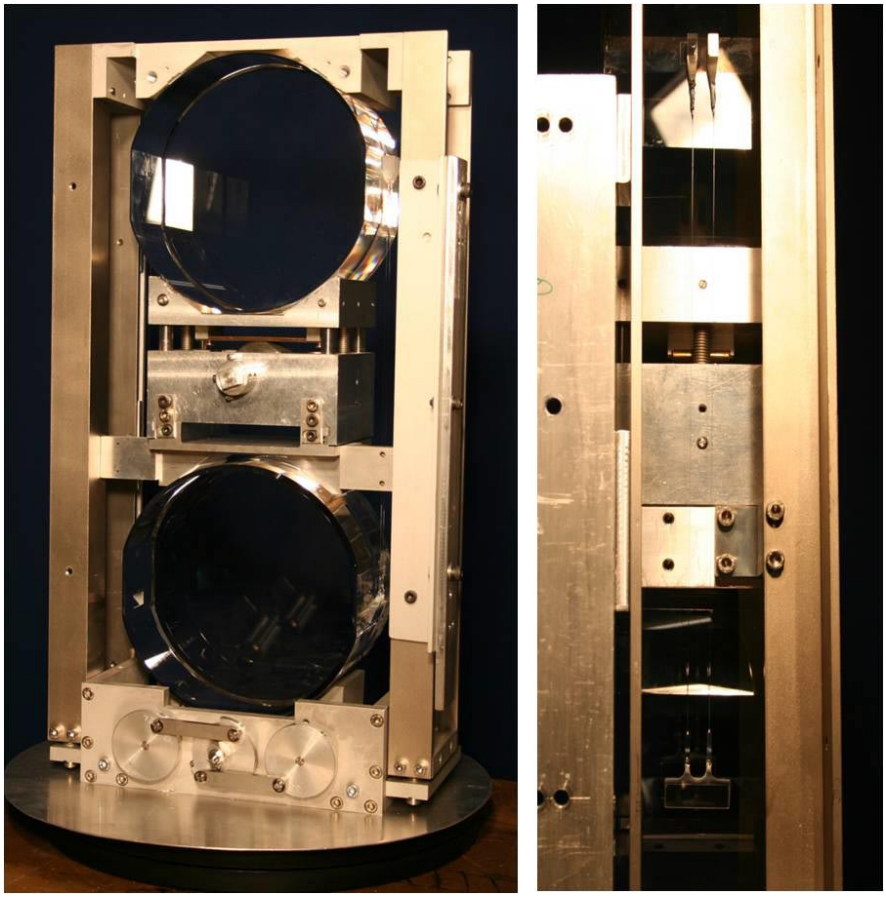

Figure 3.17 Monolithic fused silica suspension fabricated in Glasgow (2011) with four silica fibres suspending the silica test mass. The fibres were flame welded to the horns of silica ears attached to the sides of the test mass (and the intermediate mass) using the hydroxide catalysis bonding technique.

3.6 Conclusions

Currently GEO 600 is undergoing an upgrade to GEO-HF by employing advanced technologies, which would improve the sensitivity of the detector above 1 kHz. The planned upgrade requires access to the vacuum tank, which could damage the fibres of the monolithic suspension. To minimise the downtime of the detector in the event that a silica fibre breaks, a

suspension repair scenario has been developed. The repair scenario has given us a chance to incorporate a new fibre design with optimised geometry. The optimised silica fibre has a diameter of 150 μm at the thinnest cross section for the fundamental violin mode frequency to resonate above 1 kHz. Based on the stress of 800 MPa (due to the 5.6 kg test mass) on each fibre, a special cross-section having a diameter of 300 μm for thermoelastic noise cancellation was included in the geometry. Using the techniques developed in FEA, three different suspension designs having an original GEO fibre, the optimised fibre and the ideal design were studied. The energy stored in the fibre due to bending and the dissipation dilution factor of the suspension was estimated. When compared, the original and the optimised fibre had similar values of the dilution factor, however, the ideal design was higher by a factor of 4.

The total diluted mechanical loss of the suspension fibre design was predicted using the values of the elastic energy estimated from the FEA model. The mechanical loss of the optimised fibre was found to be lower than the original GEO fibre by a factor of 4. The results show that the thermal displacement noise of the optimised fibre performs better than the original fibre by a factor of 1.8. The ideal design gives a further improvement of 2.4.

The optimised fused silica fibres will be fabricated using a CO_2 laser pulling machine. The laser pulled fibres are highly reproducible unlike the flame pulled fibres used in the original suspension. The precise geometry of the optimised fibre will enable better control of the suspension and a violin mode spread of less than 1 Hz. A robust tooling and welding procedure for the fabrication of the monolithic fused silica suspension has been developed. The fused silica fibres were fabricated and strength tested to obtain a breaking stress of 4.08±0.05 GPa, which gives a factor of safety of 5. Three prototype test suspensions involving metal masses and fused silica fibres were successfully fabricated. Finally the fused silica monolithic suspension was fabricated in Glasgow, demonstrating the ability to repair the original GEO suspension.

Chapter 4 Introduction to photoelasticity and birefringence

4.1 Introduction

Second generation gravitational wave detectors such as Advanced LIGO will utilise multiple pendulums to suspend the test mass mirrors [93]. The final stage monolithic suspension will be fabricated using fused silica in order to minimise the thermal noise. The silica fibres will include residual thermal stress at the attachment points due to laser welding and mechanical stress in the fibres due to the applied load. The residual stress in an isotropic material such as fused silica changes the refractive index and induces anisotropy or birefringence [103]. Using the technique of photoelasticity one can analyse the stress in the material by measuring the retardation between the polarisation states of the incident light. The residual (thermal stress) [104] and mechanical stress in the suspension elements will allow the study of correlations between the loss in the material and the stress, in addition to annealing methods to reduce the thermal stress in fused silica.

4.2 Polarisation of light

The electromagnetic behaviour of light is made up of two components – electric and magnetic fields which are mutually perpendicular to each other and to the direction of propagation. The characteristic feature of natural (white) light is that the transverse vibration patterns are not inherently directional or rotational in nature. The vibrating waves in an ordinary light have fluctuating amplitudes and varying azimuths. However when the waves in a beam of light are constrained to vibrate in a systematic manner in

planes normal to the direction of propagation then it is said to be polarised [105].

There are three different forms of polarised light – plane, circularly and elliptically polarised light. Plane and circularly polarised light are the special cases and elliptical polarisation describes the general condition of the polarised light. Plane polarised light is obtained when the electromagnetic field is constrained to vibrate in a parallel plane such that the orientation of the electric field vector is constant (ignoring the magnetic field as it is always perpendicular and proportional to the electric field). In circular polarisation the amplitude of the electromagnetic field remains constant while the orientation of the electric field vector changes uniformly so that the tip of the vector traces out a circle. In elliptically polarised light there is a constant change of amplitude and the tip of the electric field vector traces out an ellipse. Figure 4.1 shows the schematic of plane polarised, right-circularly and right-elliptically polarised light. Left or right-handed polarisation depends upon the direction the electric vector rotates (and also depending upon the point of view of the observer).

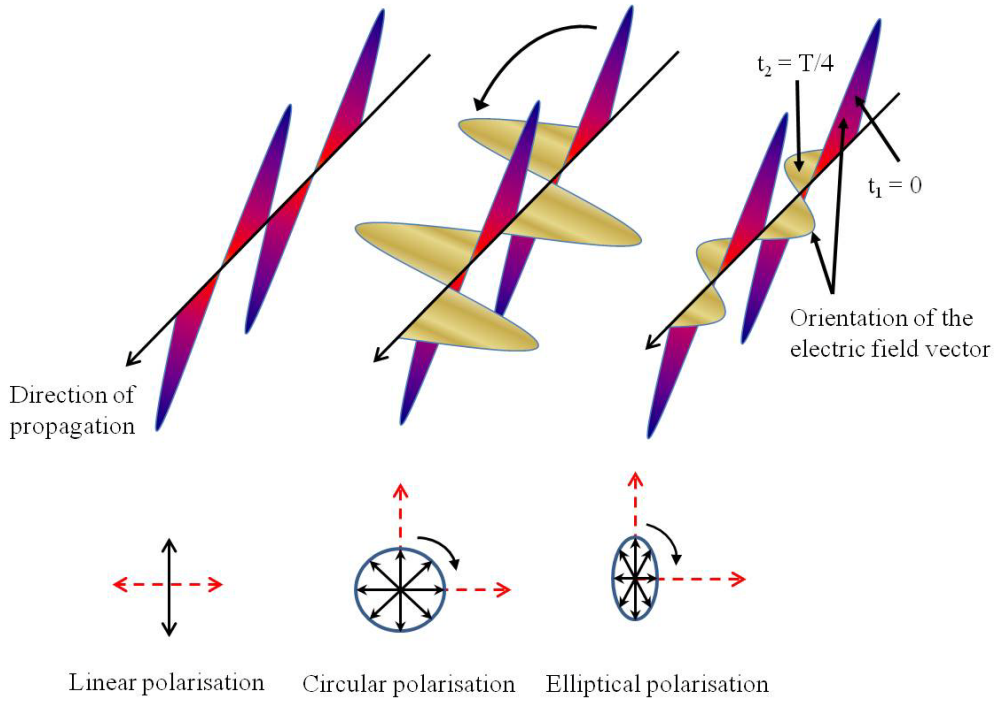

Figure 4.1 Schematic of plane (linear), circular and elliptical polarisation of light. The arrow below indicates the orientation of the tip of the electric field vector for various polarisations. Time t_1 and t_2 signifies the changing orientation of the same electric field vector to form circular or elliptical polarisation.

4.3 Transmission of light through crystals

4.3.1 Birefringence or double refraction

Birefringence or double refraction can be described as a phenomenon in which a ray of light passing through certain crystals splits into two on entrance and is then transmitted in different directions [106]. These rays are called ordinary (O) rays and extraordinary (E) rays. Figure 4.2 shows a schematic of transmission of light through a birefringent material such as a calcite rhomb. The refractive index and velocity of transmission are different for these two rays. The ordinary (O) rays obey the laws of refraction and travels without deviation whereas the extraordinary (E) rays are deviated in the crystal and suffer a lateral displacement (path difference) and phase difference on emergence. The extraordinary (E) rays do not obey Snell's law [107]. Birefringence is observed in all crystals expect the cubic class [106]. If the rhomb is rotated (with (O) rays being the axis of rotation) then the (E) rays describe a circle around (O) (as shown in figure 4.2). This shows that the direction of propagation of the (E) ray is dependent (and the (O) ray is independent) on the orientation of the crystal [108].

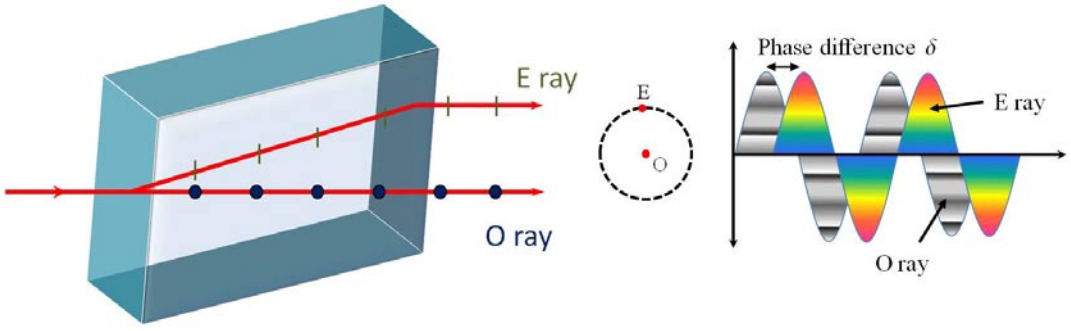

Figure 4.2 Transmission of light through a principal section of a birefringent material such as a calcite rhomb.

The emergent rays (both (O) and (E) rays) are plane polarised in mutually perpendicular planes (the E rays will vibrate along the principle section and the (O) rays in a plane perpendicular to it) if observed through a polariser. However the (O) and (E) components of light are transmitted with the same velocity and in the same direction if the transmission of rays is along the optic axis or principal crystallographic axis. Crystals having only one optic axis are called uniaxial crystals, however there are many crystals with two optic axes and they are known as biaxial crystals.

An optically isotropic non-crystalline transparent material becomes anisotropic and shows optical characteristics similar to crystals when an external stress is applied. This phenomenon is known as temporary or artificial birefringence and was first observed by Brewster [109]. These effects can be transient or permanent depending upon the type of load being applied. The study of photoelasticity is based upon the physical characteristic of these materials.

4.3.2 Plane polariscope

Polarisers are optical elements or filters which absorb the component of the light vector which is perpendicular to the axis of the polariser and transmit the parallel component [109]. Modern polarisers are made up of a polaroid H-sheet which is a transparent material (made up of polyvinyle alcohol) with iodine doping and oriented molecules. The quality of a polariser is defined by the transmission ratio, typical values are 10,000:1 and low absorption. Modern polarisers are made up of silver nanoparticles having very high transmission ratio (100,000:1) and very low absorption, typically 1.5% [110].

A plane polariscope consists of a light source and polariser/analyser set-up, schematic of which is shown in figure 4.3. There are two basic arrangements in a plane polariscope – the crossed and parallel polariser set-up. In a crossed polariser set-up the polarising axes of the polariser and the analyser are at 90^0 to each other to produce a dark field image. If the polarising axes of the polariser and the analyser are set parallel then a bright field can be obtained. A bright field set-up can be used to accurately align the photoelastic sample with the polarisers.

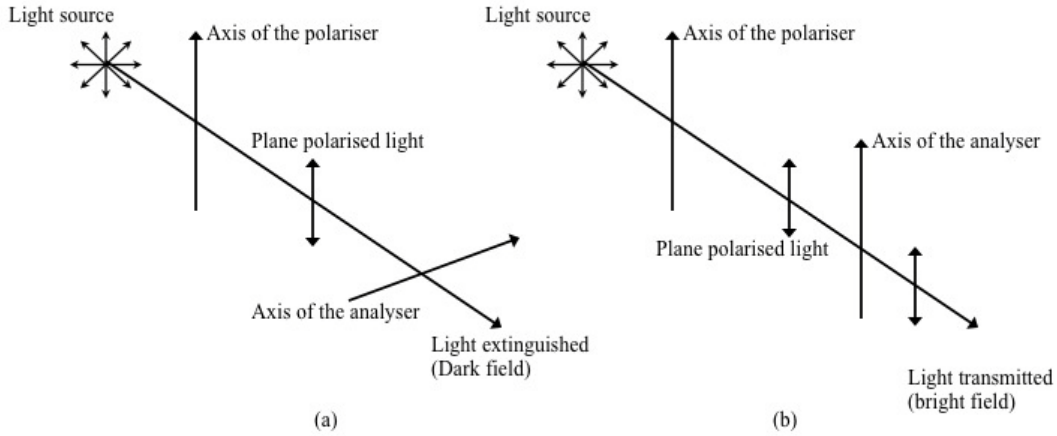

Figure 4.3 Schematic of the plane polariscope set-up (a) crossed polarisers - dark field, (b) parallel polarisers - bright field set-up.

A Polariscope set-up can be used to measure the relative retardation or phase difference produced, when plane polarised light passes through a stressed sample. The polariser converts the natural light from the source into a field of plane polarised light. The analyser, which is basically another polariser, resolves the component waves emerging from the sample into one plane so that the effects produced by the sample can be measured via the intensity of the emerging light. A dark field set-up is used for observing fringes obtained when a stressed sample is introduced and also for measurement, and is discussed in section 4.5.

4.3.3 Wave plates or retarders

Wave plates or retarders transform the polarisation states of light. They can be defined as an optical element that, without altering the intensity or degree of polarisation of a polarised monochromatic beam, resolves the light vector into two orthogonal components and then transmits each of the components at different velocity.

Ideally wave plates are 100% efficient, which means that there is no change in the intensity of the light on passing through the wave plates. Wave plates can be used in conjunction with polarisers to produce circularly or elliptically polarised light. The techniques of photoelasticity are based upon the analysis of light using these wave plates or retarders [106].

4.3.4 Circular polariscope

Quarter-wave plate

A quarter wave plate is used to convert a plane polarised light into circularly polarised light and vice versa. These plates are made of mica sheets or other non-crystalline material such as glass, cellophane or plastics. The thickness of the quarter-wave plate (which is cut parallel to the optic axis) is such that the phase difference between the (O) and the (E) rays at the exit is equal to $\lambda/4$ for the particular wavelength of monochromatic light used. A quarter wave plate has two axes – fast and slow. The phase velocity of light is higher for polarised light passing through the fast axis as compared to the slow axis.

To study the effect of quarter wave plates between two polarisers, consider a plane polarised wave emerging from a polariser, which is represented by vector OP in figure 4.4. This can be expressed as,

$$x = 0, \tag{4.1}$$

$$y = \sqrt{2}a \sin \omega t, \tag{4.2}$$

The light enters the quarter wave plate whose principal axis is at an angle 45^0 with respect to OP. OM and ON are the fast and slow axes of the quarter wave plate respectively.

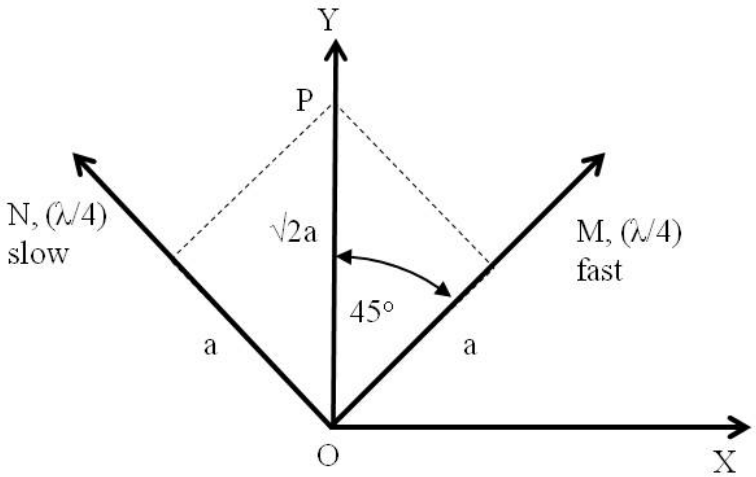

Figure 4.4 Schematic of plane polarised light on entering a quarter wave plate.

Here the light splits into two components of equal magnitude in the direction ON and OM as given below,

$$M = a \sin \omega t \tag{4.3}$$

$$N = a \sin \omega t \tag{4.4}$$

However the quarter wave plate introduces a phase difference between these two components such that on emergence,

$$M = a \sin\left(\omega t + \frac{\pi}{2}\right) = a \cos \omega t, \tag{4.5}$$

$$N = a \sin \omega t. \tag{4.6}$$

These equations represent a circular motion for the light vector and hence the quarter wave plate converts the linear polarisation to circular polarisation.

When a circularly polarised light is incident on another quarter wave plate (fast axis coinciding), the light on emergence is given by,

$$M = a \cos\left(\omega t + \frac{\pi}{2}\right) = -a \sin \omega t, \tag{4.7}$$

$$N = a \sin \omega t. \tag{4.8}$$

The resultant is a plane polarised wave along the axis of the analyser (X) and is given by,

$$X = \sqrt{2} a \cos\left(\omega t + \frac{\pi}{2}\right), \tag{4.9}$$

$$Y = 0. \tag{4.10}$$

where the amplitude of the wave is $\sqrt{2}a$ vibrating in the horizontal plane. When the quarter wave plates are in series (i.e. when the corresponding axes are parallel) they behave as a half wave plate, thus rotating the plane of polarisation through 90^0. The various arrangements to obtain dark or bright field images using a circular polariscope are shown in table 4.1. In a crossed polariscope set-up, when the fast and slow axis of the first and second quarter wave plates are at 45^0 to the polariser then a dark field is obtained. However if the fast axes of the two quarter wave plates are aligned (yet they remain at 45^0 to the polariser) then a bright field is obtained.

Polariser angle	First quarter wave plate angle	Second quarter wave plate angle	Analyser angle	Image obtained
0^0	45^0 (fast axis)	45^0 (slow axis)	90^0	Dark field
0^0	45^0 (fast axis)	45^0 (slow axis)	0^0	Bright field
0^0	45^0 (fast axis)	45^0 (fast axis)	90^0	Bright field
0^0	45^0 (fast axis)	45^0 (fast axis)	0^0	Dark field

Table 4.1 Various arrangements of the circular polarsicope set-up to obtain a dark field or bright field image.

4.4 Stress optic law (in two dimensions)

The principal axes of stress at any point in a stressed sample become the fast and slow axes of the sample. Initially when a material is in an unstressed state they exhibit an index of refraction, n_0, which is the same at all the points in the sample. However when an external stress is applied, this leads to a change in refractive index. The relationship between the stress and changes in the index of refraction was first studied by Maxwell [106, 108]. The changes in the indices of refraction are linearly proportional to the stresses induced in the model as shown below [106],

$$\begin{aligned} n_1 - n_0 &= c_1\sigma_1 + c_2\sigma_2 \\ n_2 - n_0 &= c_1\sigma_2 + c_2\sigma_1 \end{aligned} \tag{4.11}$$

where n_0 is the index of refraction in the unstressed state, n_1, n_2 are the indices of refraction along the two principal axes associated with stresses σ_1 and σ_2 respectively, and c_1 (direct) and c_2 (transverse) are the stress optic coefficients.

If the two equations shown in 4.11 are subtracted to eliminate n_0 then,

$$n_1 - n_2 = (c_1 - c_2)\,(\sigma_1 - \sigma_2). \tag{4.12}$$

The retardation, δ, or phase shift between the two components emerging from a wave plate is given by,

$$\delta = \frac{2\pi d}{\lambda}(n_1 - n_2), \tag{4.13}$$

where d is the thickness of the sample. Hence substituting $n_1 - n_2$ from equation 4.12 gives,

$$\delta = \frac{2\pi d}{\lambda}(c_1 - c_2)\,(\sigma_1 - \sigma_2), \tag{4.14}$$

where the retardation is expressed in Brewsters (1 Brewster = 10^{-12} m^2/N) and λ is the wavelength of light. If $c_1 - c_2$ is set equal to c, where c is the relative stress optic coefficient then the relative retardation is given by,

$$\delta = \frac{2\pi dc}{\lambda}\,(\sigma_1 - \sigma_2). \tag{4.15}$$

Equation 4.15 can be re-written in terms of fringe order N (which is the relative retardation in terms of a complete cycle of retardation, 2π),

$$N = \frac{\delta}{2\pi} = \frac{dc}{\lambda}\,(\sigma_1 - \sigma_2), \tag{4.16}$$

or

$$(\sigma_1 - \sigma_2) = \frac{N\lambda}{dc}. \tag{4.17}$$

Hence using equation (4.17) the stress difference at each point in a two dimensional photoelastic model can be determined if the relative retardation N can be measured.

4.5 Effects of a stressed sample in a plane polariscope

The crossed or open combination of polarisers can also be used to study the relative retardation and phase difference produced when polarised light passes through a stressed photoelastic sample [111].

Figure 4.5 shows a set-up comprising a polariser, analyser and a stressed sample. The light source is a He-Ne laser. The stressed sample considered here is a temporary doubly refractive transparent material (e.g. a fused silica under load). The birefringent sample behaves like a wave plate and the principal stress difference can be determined once the retardance at each point is measured. Figure 4.5b shows the resolution of the light vector in the stressed sample. As the polarised light emerges from the polariser and enters the sample, the principal stress direction makes an angle θ with the axis of the input polariser (along the y axis).

Plane polarised light emerging from the polariser vibrates in a vertical plane with amplitude a and angular frequency ω is given by [106],

$$\begin{aligned} x &= 0, \\ y &= a \sin \omega t \end{aligned} \tag{4.18}$$

The light vector entering the stressed sample is then resolved into two components Ox_1 and Oy_1 as given below [106],

$$x_1 = y \cos\theta = a \cos\theta \sin \omega t \tag{4.19}$$

$$y_1 = y \sin\theta = a \sin\theta \sin \omega t \tag{4.20}$$

These two components of light propagate at different velocities within the sample. As a result of which, once they emerge out of the sample they are out of phase with each other. If Ox_1 is the fast axis then the phase difference α between the two components is given as,

$$x_1 = a \cos\theta \sin(\omega t + \alpha), \tag{4.21}$$

$$y_1 = a \sin\theta \sin \omega t. \tag{4.22}$$

These equations represent an elliptical vibration and therefore the stressed sample converts the plane polarised light into elliptically polarised light. The resultant vibration emerging from the sample is then incident upon the analyser which transmits only the component parallel to its axis.

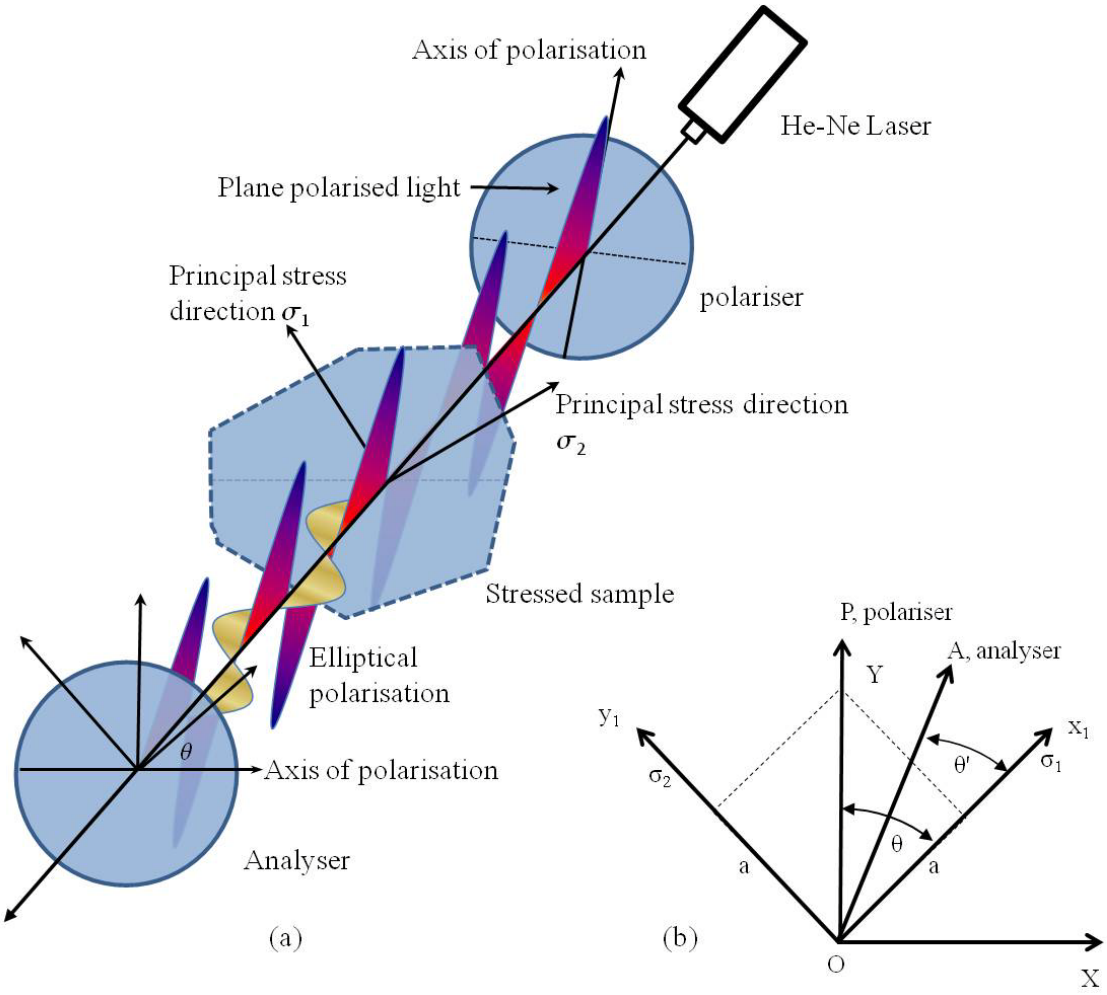

Figure 4.5 (a) Schematic of a photoelastic stressed sample in a plane polariscope set-up. (b) The resolution of light vector passing through a stressed sample in a plane polariscope. A photograph of the experimental set-up is shown in chapter 5, figure 5.1.

4.5.1 Isoclinic and Isochromatic fringes

When a stressed sample is viewed through a crossed polariscope then a continuous band of bright and dark lines is observed under monochromatic light. These fringes are due to the constructive and destructive interference of the light emerging through the analyser. Figure 4.6 shows the superimposed and separated isoclinic and isochromatic fringes in a stressed lexan sheet. The light source used is a He-Ne laser. The continuous curves or lines are called isoclinic fringes. The isoclinic fringes (hereafter denoted

isoclinics) are the loci of points where the principal stress direction (either σ_1 or σ_2 as shown in figure 4.6(a) coincide with the axis of the polariser). Hence they are useful in obtaining the direction of principal stress at any point in the sample. The other types of fringes observed in a plane polariscope are isochromatic fringes. The isochromatics give the magnitude of the stress tensor and they are classified as lines along which $\sigma_1 - \sigma_2$ equals a constant depending upon the order of the fringe. In a plane polariscope these two fringes are superimposed on each other and special techniques need to be employed for their separation [107]. The isoclinics can be removed using a circular polariscope, leaving behind only isochromatics as shown in figure 4.6(b). If white light is used in a polariscope then the isochromatics can be easily distinguished from isoclinics as the former are coloured (except the zero fringe order) and the latter appear as black bands. In monochromatic light both the fringes look black, however the isochromatics are much more sharply defined than isoclinics [106].

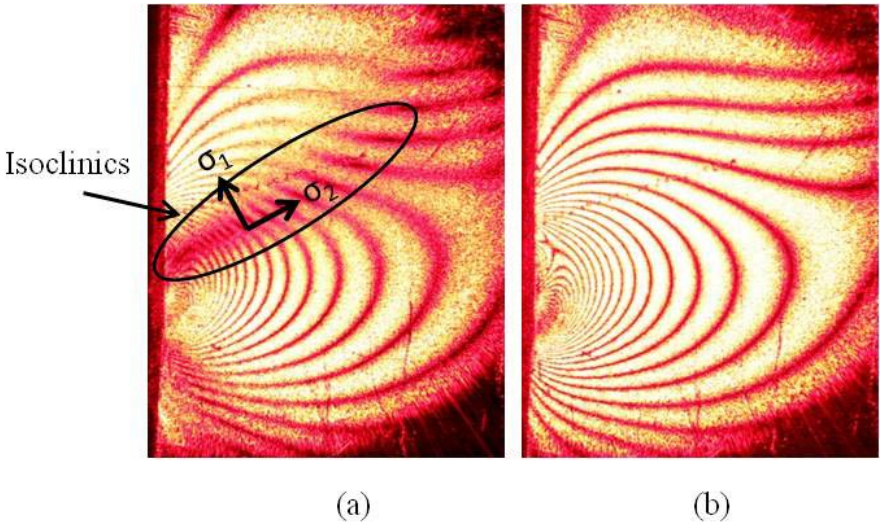

Figure 4.6 (a) A stressed lexan sheet observed under a plane polariscope using a He-Ne laser as a light source. The isoclinics (encircled) and isochromatic fringes are superimposed on each other. One of the principal stress axis (σ_2 in the figure) coincides with the isoclinics. (b) Using a circular polariscope set-up (discussed in section 4.6) the isoclinics are removed, leaving behind the isochromatic fringes which are sharply defined.

The other way to distinguish between the two fringes is through applying a static or varying load on a sample and observing through a crossed polariscope. Under a static load, and while rotating the polariscope, the isoclinic pattern changes while the isochromatics remain unchanged. However on varying the load and keeping the polariscope fixed, the isochromatics change while the isoclinics remain unchanged.

4.6 Effects of a stressed sample in a circular polariscope

A plane polariscope can be converted into a circular polariscope by inserting two quarter wave plates between the crossed polarisers. In the set-up, the principal axes of the quarter waves plates are crossed with each other and are at 45^0 to the polariser. There are two axes in a quarter wave plate – the fast and the slow axis as shown in figure 4.7(a). When the fast and the slow axes of the quarter wave plate are aligned with each other then extinction can be obtained when the analyser is crossed to the polariser. This is called a dark field arrangement or a standard circular polariscope arrangement. However when the axis of the quarter wave plates are aligned then a bright field is obtained. A bright field is useful for alignment purposes [106, 108].

The quarter wave plates convert plane polarised light into circularly polarised light and vice versa. One of the major advantages of using a circular polariscope is that it eliminates the isoclinic fringe patterns while it maintains the isochromatic fringe pattern. A photoelastic stressed sample can be studied using a circular polariscope set-up. Figure 4.7(a) shows the arrangement of a circular polariscope set-up to investigate thermal or mechanical stress induced in a sample. In figure 4.7(b) the axis of the polariser is represented by OB, and the principal axes of the two quarter wave plates as OX' (fast axis) and OY'(slow axis).

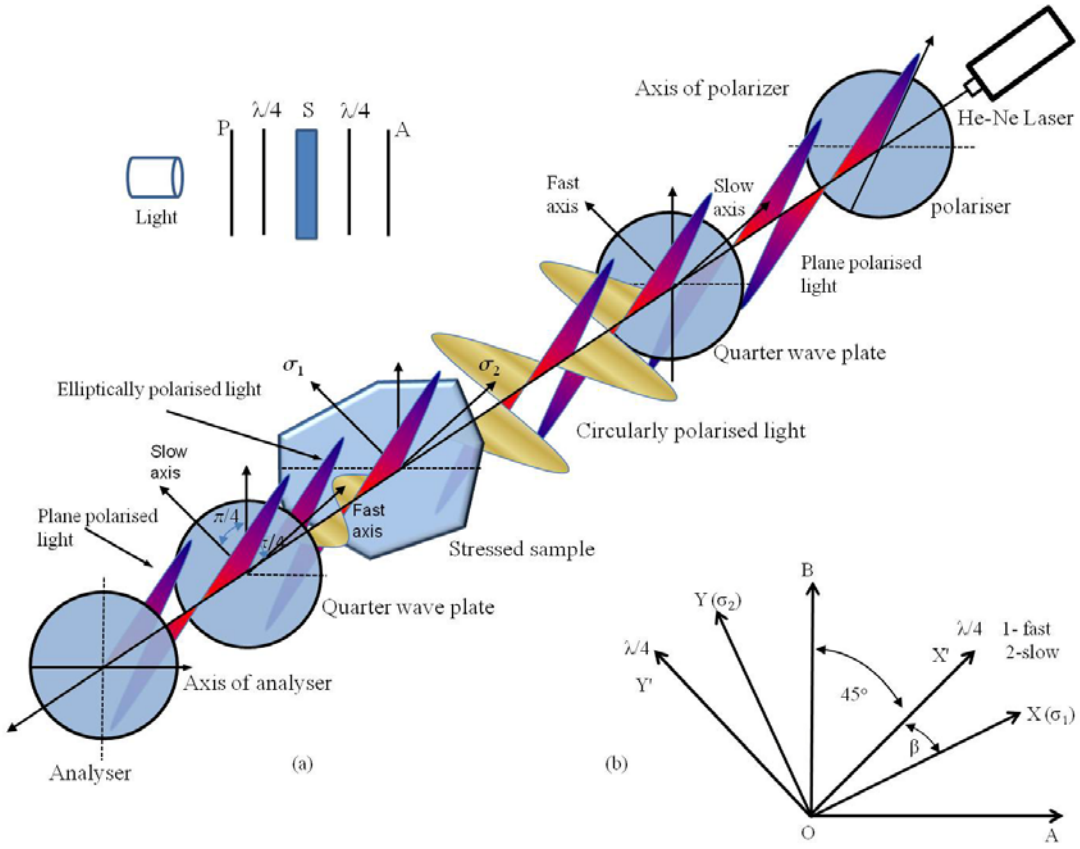

Figure 4.7 (a) Schematic of a stressed sample inserted within a circular polariscope arrangement using a He-Ne laser as a light source. (b) Resolution of the field components through the stressed sample.

The wave emerging from the first quarter wave plate (which is 45^0 to the polarising axis) will be circularly polarised as discussed in section 4.3.4. The circularly polarised light then enters the photoelastic sample and splits into two components vibrating in the directions OX, OY of the principal stresses $\sigma_1$and σ_2. The two components of light entering the sample can be expressed as,

$$X = \frac{a}{\sqrt{2}}\cos \omega t, \tag{4.23}$$

$$Y = \frac{a}{\sqrt{2}}\sin \omega t. \tag{4.24}$$

If OX is the fast axis then a phase difference is introduced between the two components due to the principal stress difference $(\sigma_1 - \sigma_2)$, which can be

represented as α. The light leaving the sample will be elliptically polarised and can be expressed as,

$$X = \frac{a}{\sqrt{2}}\cos(\omega t + \alpha), \tag{4.25}$$

$$Y = \frac{a}{\sqrt{2}}\sin \omega t. \tag{4.26}$$

The elliptically polarised light then enters the second quarter wave plate whose axes are given by OX' and OY'. Including the angle β with the principal axes of stress leads to,

$$X' = X\cos\beta + Y\sin\beta, \tag{4.27}$$

$$Y' = Y\cos\beta - X\sin\beta. \tag{4.28}$$

Considering OY' as the fast axis of the second quarter wave plate, the emergent light is,

$$X' = \frac{a}{\sqrt{2}}[\cos(\omega t + \alpha)\cos\beta + \sin \omega t \sin\beta], \tag{4.29}$$

$$Y' = \frac{a}{\sqrt{2}}\left[\sin(\omega t + \frac{\pi}{2})\cos\beta - \cos(\omega t + \frac{\pi}{2} + \alpha)\sin\beta\right],$$

$$= \frac{a}{\sqrt{2}}[\cos \omega t \cos\beta + \sin(\omega t + \alpha)\sin\beta]. \tag{4.30}$$

The light emerging from the second Quarter wave plate will be plane polarised when $\alpha = 0$ or 2π. This condition is only true for certain points of interest (where measurements are to be taken) in the sample which is aligned with the fast or slow axis of the quarter wave plate. This is further discussed in section 4.7.2. Circular or elliptical polarisation can be observed at other points in the sample. Equation (4.29) and (4.30) will be further used in section 4.7.2, describing the Tardy method of compensation to measure the retardance of light.

4.7 Compensation technique for the measurement of retardance

There are various techniques used in industry to measure retardance in a sample. However only two such methods will be discussed in this thesis. The

Babinet-soleil compensation method and compensation using quarter wave plates – the Tardy method. These two techniques were employed to measure the residual stress in fused silica which is discussed in the next chapter.

4.7.1 The Babinet-Soleil compensators

Retardation at any point in a sample can be measured to a high degree of accuracy by means of an instrument known as a compensator. One such type is a Babinet-Soleil compensator, which is a variable wave plate, which can be inserted into the field of the polariscope with the fast axis oriented along the principal stress direction. Figure 4.8 shows a schematic of the optical layout along with the photograph of the Babinet-soleil compensator (Thorlabs: SBC-VIS). It is made up of a quartz plate of uniform thickness and two quartz wedges. One of the quartz wedges can be moved in and out using a micrometer screw. The optical axis of the quartz in the plate and the wedges are orthogonal to each other. Quartz is a naturally doubly refracting material; hence by adjusting the thickness of the two wedges one can vary the birefringence in the material. The retardance produced is uniform over the whole field of view of the compensator [112].

To measure the retardance at a point in a stressed sample, the compensator is calibrated at the operating wavelength of the He-Ne laser (633 nm). Firstly the Babinet-Soleil compensator is placed between crossed polarisers. The fast axis of the compensator is aligned with the polarising axis of either of the two polarisers which leads to extinction of light when viewed through the analyser. The compensator is then rotated by 45^0 which leads to some light being transmitted through the analyser. The compensator micrometer is then adjusted until extinction at the analyser is achieved. This gives the first of the two null points which are used as a full wave reference. The micrometer reading is then zeroed at this point. The micrometer is further adjusted such that the laser light is visible again and is then extinguished (i.e moving from a bright to dark field). This gives the second null point. Recording the micrometer reading (in terms of distance, mm) at this point corresponds to the calibration distance equal to one full wave of retardance at 633 nm. The step by step procedure for calibrating the compensator is discussed in the instrument manual [113].

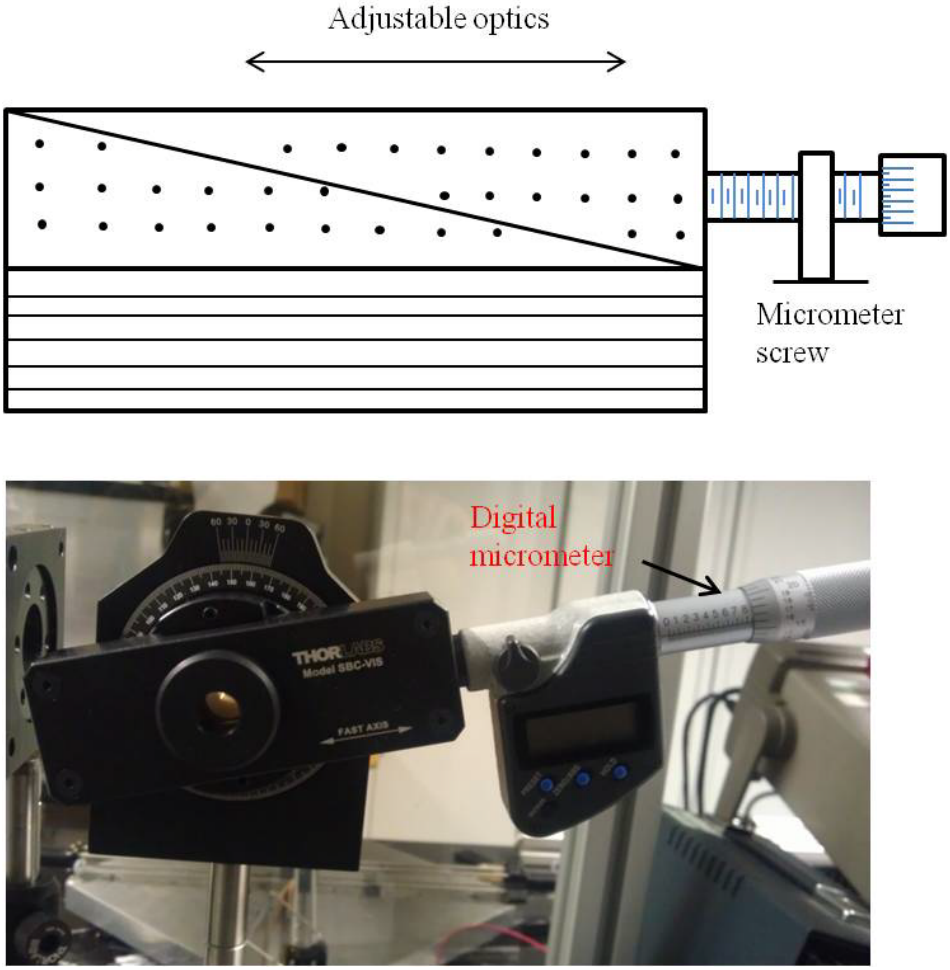

Figure 4.8 Schematic of the optical layout (quartz plate and wedges) inside a Babinet-Soleil compensator. The photograph at the bottom shows the Babinet-Soleil compensator (Thorlabs SBC-VIS) set-up in the lab.

To measure the unknown retardance in a sample the compensator is again placed between the crossed polarisers such that a dark field is obtained at the analyser [114]. Next the sample (in a rotation mount) is inserted before the compensator, which should produce some light at the analyser due to the birefringence of the sample. The sample is rotated such that the laser spot is again extinguished. The sample along with the compensator is then further rotated by 45^0. The micrometer is adjusted to obtain a dark field and the reading is recorded and used to calculate the value of retardance from the previous calibration [113]. It is important to note that the compensator needs to be calibrated each time when used (unless it is not taken out of the set-up). This is to avoid calibration error, which could give large deviations in the measured retardance.

4.7.2 The Tardy method of compensation

The tardy method of compensation is achieved via the use of two quarter wave plates and two polarisers. This method is employed to determine the order of fringe, N, at any point on the sample. Using this technique retardance can be measured to a high degree of accuracy using the normal equipment of a polariscope [106, 115, 116].

The arrangement of the polariscope and quarter wave plate is similar to that shown in figure 4.7 for operating a circularly polariscope. A point of interest (POI) is marked on the sample for the measurement of stress. Firstly the axis of the polariser is set parallel to one of the principal axes of stress in the model at the POI where the retardance is to be measured. This is achieved through rotating the sample such that an isoclinic passes through the POI. The two quarter wave plates are then inserted such that their axes are crossed and at 45^0 to those of the polarisers and the principal axes of the model.

Now the state of polarisation at exit from the second quarter wave plate is given in the equations (4.29) and (4.30). As $\beta = 45^0$ in the Tardy method, these equations become [106],

$$X' = \frac{1}{2}a[\cos\ (\omega t + \alpha) + \sin\ \omega t], \tag{4.31}$$

$$Y' = \frac{1}{2}a[\cos\ \omega t + \sin\ (\omega t + \alpha)]. \tag{4.32}$$

If the axis OX' of the analyser is inclined at an angle θ'' to the crossed position OX in figure 4.9, then the component transmitted is

$$X'' = X'\cos\left(\frac{\pi}{4} - \theta''\right) - Y'\sin\left(\frac{\pi}{4} - \theta''\right) \tag{4.33}$$

$$= \frac{a}{2\sqrt{2}}\{[\cos(\omega t + \alpha) + \sin\omega t][\cos\theta'' + \sin\theta'']$$

$$-[\cos\omega t + \sin(\omega t + \alpha)]\,[\cos\theta'' - \sin\theta'']\},$$

which reduces to,

$$X'' = \frac{a}{\sqrt{2}}\sin\left(\theta'' - \frac{\alpha}{2}\right)\left[\sin\left(\omega t + \frac{\alpha}{2}\right) + \cos\left(\omega t + \frac{\alpha}{2}\right)\right]. \tag{4.34}$$

The amplitude of this wave is given by $\frac{a}{\sqrt{2}}\sin\left(\theta'' - \frac{\alpha}{2}\right)$. The intensity of the light transmitted by the analyser will be zero when $\sin\left(\theta'' - \frac{\alpha}{2}\right) = 0$.

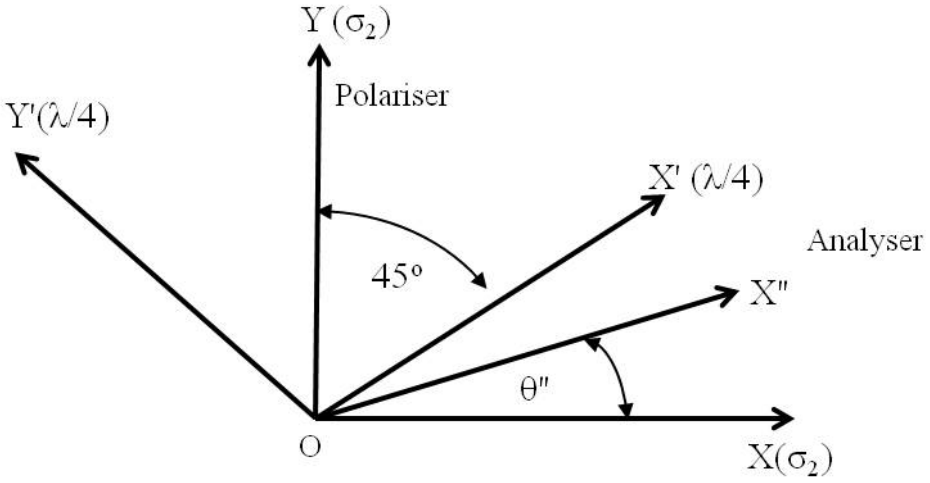

Figure 4.9 Resolution of light vector through the quarter wave plate.

To produce extinction at the point of interest the analyser must be rotated clockwise or anticlockwise. This is called angle of compensation and can have values between $+\pi$ and $-\pi$. In practice, extinction is obtained at any angle by rotating the analyser in one direction or through the complimentary angle in the opposite direction. The phase difference is given by $\alpha = 2n'\pi + \Delta\alpha$, where $2n'\pi$ and $\Delta\alpha$ represent the integral and fractional parts and n' is the integral fringe order whose values are zero or any integer. The integral fringe order can be obtained by counting from the point of the zero order fringe towards the higher order fringe. If m is the compensation angle measured in the direction which causes the fringe of lower order n' to move to the observed point then the phase difference is $\alpha = 2n'\pi + 2m$

At this point the retardation in wavelength is given by,

$$R = n = \frac{\alpha}{2\pi} = n' + \frac{m}{\pi} = n' + \frac{m^0}{180^0}. \tag{4.35}$$

For measuring the complimentary angle we use $n = (n' + 1) - \frac{180^0 - m}{180^0}$.

4.8 Conclusions

The photoelastic birefringence techniques presented in this chapter can be useful for the measurement of mechanical and thermal stress in materials such as fused silica. The different forms of polarisation, their production and subsequent use have been discussed. The plane polariscope can be used to observe the thermal or mechanical stress in a sample, through the isoclinic and isochromatic fringe patterns. The direction of the principal stress can be determined through the study of isoclinic fringes. Using wave plates, such as a quarter wave plate, circularly polarised polarised light can be generated. Birefringence in a material can be studied using wave plates or retarders in a circular polariscope set-up. The general condition of light passing through a plane and circular polariscope has been discussed. The effect of the polarised light passing through a stressed sample in a plane and circular polariscope has been shown. Also the various possible arrangements of the polariscope to obtain a bright or dark field have been discussed. Isochromatic fringes obtained using two quarter wave plates between polarisers can be used for determining the magnitude of stress in the sample (by estimating the retardance of the light). Using the stress optic law, the stress difference at each point in a two dimensional photoelastic model can be determined once the relative retardation is measured. Different methods of compensation techniques for the measurement of relative retardation have been discussed. These techniques include the use of Babinet-Soleil compensator and the Tardy method of compensation. The set-up and protocol required for using these two compensation techniques has been shown.

The photoelastic birefringence technique discussed in this chapter has been used to study and characterise the mechanical and thermal stresses developed in fused silica, and is further discussed in chapter 5.

Chapter 5 Study of mechanical and thermal stress in fused silica

5.1 Introduction

The techniques discussed in the previous chapter on photoelascitiy can be employed to measure mechanical and thermal stress induced in a body. Fused silica is the material used in the construction of suspension elements of the aLIGO detector. The test mass suspensions have silica fibre ends laser welded to the horns of the silica ears. During the process of laser welding the fibres are subjected to high temperature and temperature gradients especially at the stock and ear-horn region. The thermal gradients could lead to residual thermal stress once the material cools down to room temperature. During destructive testing of the silica fibres they are usually found to be broken at their stock region where it is believed that the residual thermal stresses are higher due to laser heating. Having high thermal stress in the horns of the ears is also not desirable as the ears cannot be easily repaired/replaced once damaged. Hence it is important to study and estimate the thermal stress induced in the material when subjected to high temperature gradients.

The experiments discussed in this chapter study the mechanical and thermal stress in a fused silica slide. Mechanical stresses were studied to test and understand the working of the birefringence techniques (using the Tardy method of compensation and the Babinet-Soleil compensator) discussed in the previous chapter. The mechanical stress measured in a body of planar geometry can be verified using theoretical calculations and finite element analysis. The experimental techniques can then be employed to measure more complicated cases like the thermal stresses in a body due to

laser heating. The results from the photoelasticity measurements can then be analysed and compared with modelling techniques developed in FEA via which the temperature profile, thermal gradient and the resulting stress can be estimated.

5.2 Mechanical stress in fused silica

5.2.1 Silica Cantilever

A plane polariscope was set up consisting of a He-Ne (633 nm) laser as a light source to measure retardation caused by applying a mechanical load on a fused silica sample. The polariscope consisted of two plane polarisers and two quarter wave plates for the production of plane and circularly polarised light (as described in chapter 4). Figure 5.1 shows the experimental set-up used for observing and estimating stress in a sample. A ground glass type diffuser (from Thorlabs N-BK7) was used for expanding the laser beam diameter to approximately 1 inch. A short focal length collimating lens was placed in front of the diffuser to produce collimated light. A digital SLR camera (Canon 600D) with a macro lens (60 mm Canon) was used to record the images.

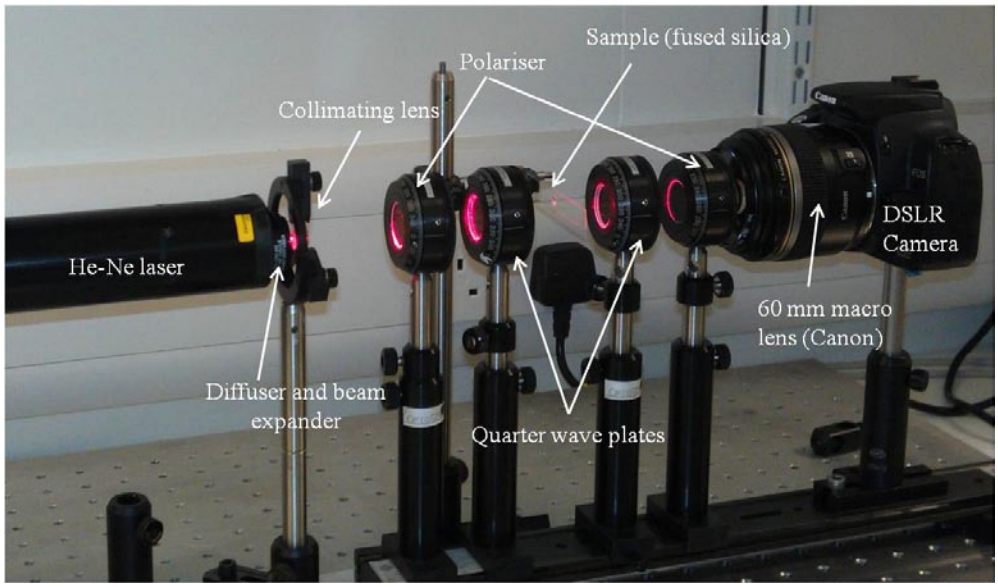

Figure 5.1 Set-up of a polariscope for studying stress in the sample, consisting of two polarisers. The set-up also has two quarter wave plates inserted between the polarisers to form a circular polariscope. The light source used is a 1mW He-Ne laser.

A silica slide of dimensions 50 mm by 10 mm and thickness 1 mm was used as a cantilever as shown in figure 5.2, and a mass of 1.2 kg was loaded at one end to induce temporary birefringence in the material. Mechanical stress creates anisotropy in fused silica (which is normally isotropic) by changing the refractive index of the material and thus leads to double refraction, which can be observed in a plane polariscope with a dark field set-up (i.e. axes of polarisers crossed to each other).

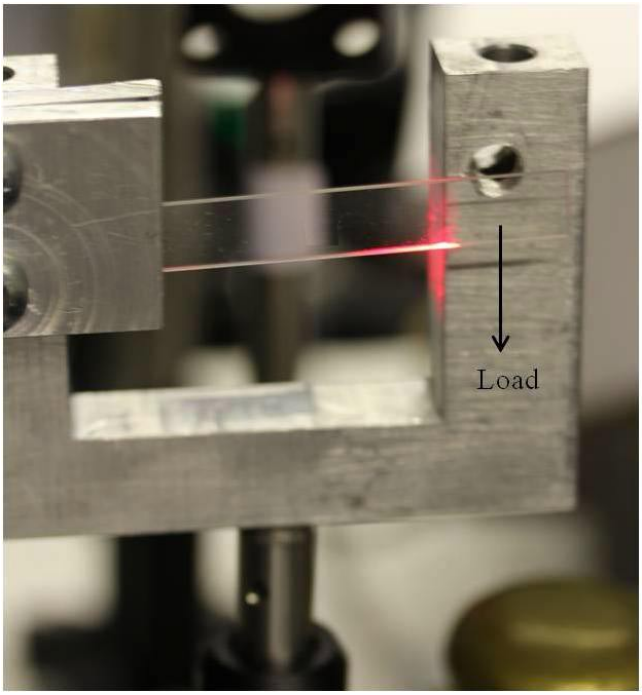

Figure 5.2 Fused silica cantilever clamped from one end and a mechanical load is applied at the free end to induce temporary anisotropy in the material.

The sample under mechanical load was first studied under a plane polariscope (schematic of the setup shown in chapter 4, figure 4.5) to observe the stress patterns. Figure 5.3(a, b) shows the fringes obtained in a plane polariscope for a silica slide under load. The black line at the centre is the neutral axis and also an isoclinic fringe. The position of the isoclinic fringe can be moved up or down by rotating the crossed polariser clockwise or anticlockwise. To measure the relative stress, a point of interest (POI) was marked as a black dot, which is shown in the figure 5.3. The nearest

isoclinic fringe is then used to extinguish (by superimposing the isoclinic on the POI to make it appear dark) the POI as shown in figure 5.3(b). The trajectory of one of the principal stress axes now coincides with the POI. Once the direction of the principal stress is aligned with the POI the magnitude of the stress can be measured by employing a circular polariscope. The magnitude of the stress can be measured using the information from the isochromatic fringes, which are hidden within the isoclinic patterns in a plane polariscope. Hence two quarter wave plates with their fast axes crossed are inserted between the crossed polarisers as described in chapter 4. The fast axes of the quarter wave plates are at 45^0 with the crossed polarisers. Under this set-up of a circular polariscope the isoclinics disappear leaving only isochromatic fringes. Figure 5.3(c) shows the isochromatics obtained under a circular polariscope. Now on rotating the analyser while keeping the rest of the set-up fixed, the POI can be extinguished for the second time, which is shown in figure 5.3(d). The angle rotated by the analyser is defined as θ. The measured value of θ can be used in equation (4.35) to estimate the retardation in wavelength of the He-Ne laser. The stress optic law can then be used to determine the relative principal stress using, $(\sigma_1 - \sigma_2) = \frac{N\lambda}{dC}$, where $N = \frac{\theta}{180}$, which is discussed in chapter 4 (equation 4.17). The value of the stress optic coefficient (C) of fused silica is given by 3.55×10^{-12} m^2/N [117], and is required in equation (4.17) for estimating the relative stress. The stress at two other points on the sample was measured in a similar way. The experimental results were then compared to a FEA model in ANSYS. The FEA model was solved for static structural analysis to obtain the stress results. Figure 5.4 shows the FEA model of the silica cantilever, which is clamped from one end, and a load of 12 N applied at the free end.

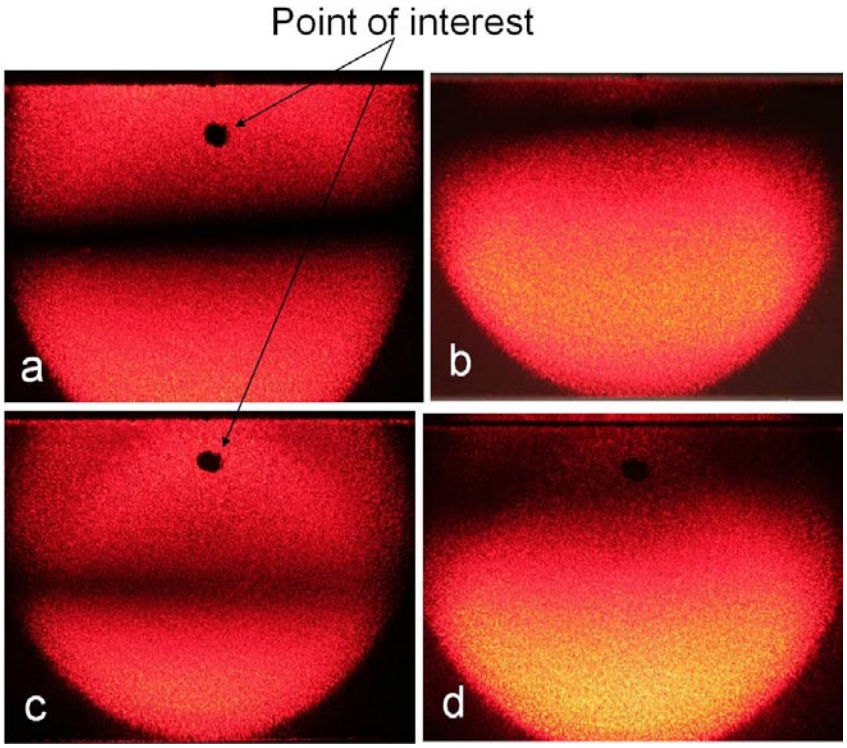

Figure 5.3 (a, b) – Isoclinic fringes observed under a plane polariscope with crossed axes (dark field), for a silica cantilever under mechanical load. (c, d) – isochromatic fringes observed in a circular polariscope set up.

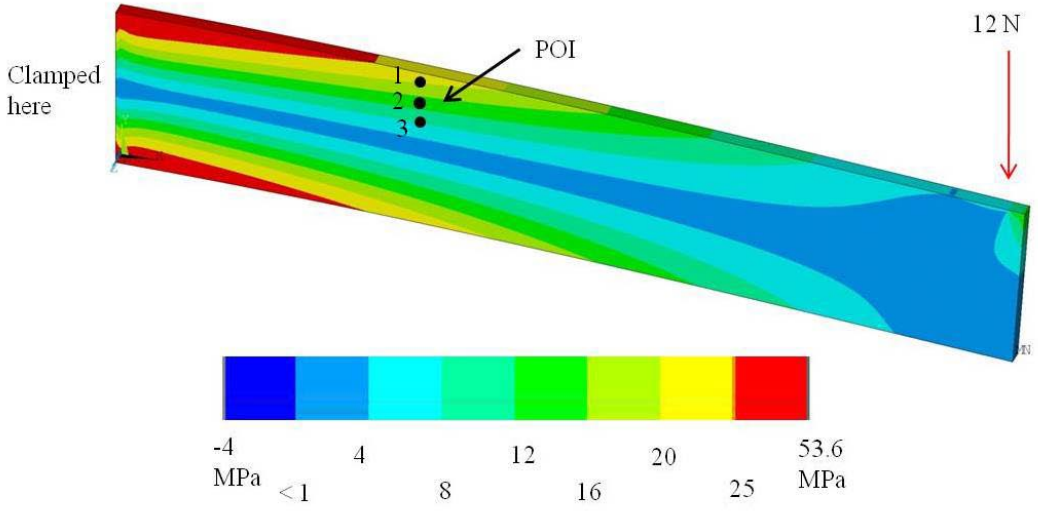

Figure 5.4 FEA model of a silica cantilever clamped from one end and under a load at the free end, showing the mechanical stress gradients.

Table 5.1 compares the relative principal stress estimated using the photoelasticity measurements and ANSYS (FEA) modelling. The statistical error of the experimental stress values were estimated by taking a ratio of the standard deviation and the square root of the number of measurements. The relative stress values estimated from the experiments agree with the FEA model, with ≅ 5% of difference.

Point of interest	Stress, (Experimental) MPa	Stress, (FEA) MPa
1	18.82±0.13	17.9
2	14.85±0.14	14.2
3	10.89±0.24	10.6

Table 5.1 Principal stress measured using photoelasticity and compared with results obtained from FEA for a silica cantilever under a bending load. The errors in the experimental values are the statistical errors, the systematic errors of the measured values is ±1 MPa*.*

5.2.2 Silica slide under axial tension

A second case was studied for a silica sample under axial tension; the sample used was identical to that used in the previous section $(50 \times 10 \times 1\ \text{mm})$. The axial tension on the sample was applied by suspending a 10 kg metal mass. Figure 5.5(a) shows the schematic of the experimental setup. The sample under axial tension was then observed under a plane polariscope setup, which is shown in figure 5.5(b). Temporary anisotropy in the sample under tension induces birefringence. Since the tension applied on the sample is acting uniformly, the observed brightness is also uniform at all points as shown in figure 5.5(c). Measurements were done at several POI's using the techniques of photoelasticity and a relative stress of 10.49±0.25 MPa was estimated. The estimated errors are the standard deviation of the measured values. A theoretical calculation gives a stress of 9.81 MPa (for a 1 mm by 10 mm cross section), which agrees well with the experimental value.

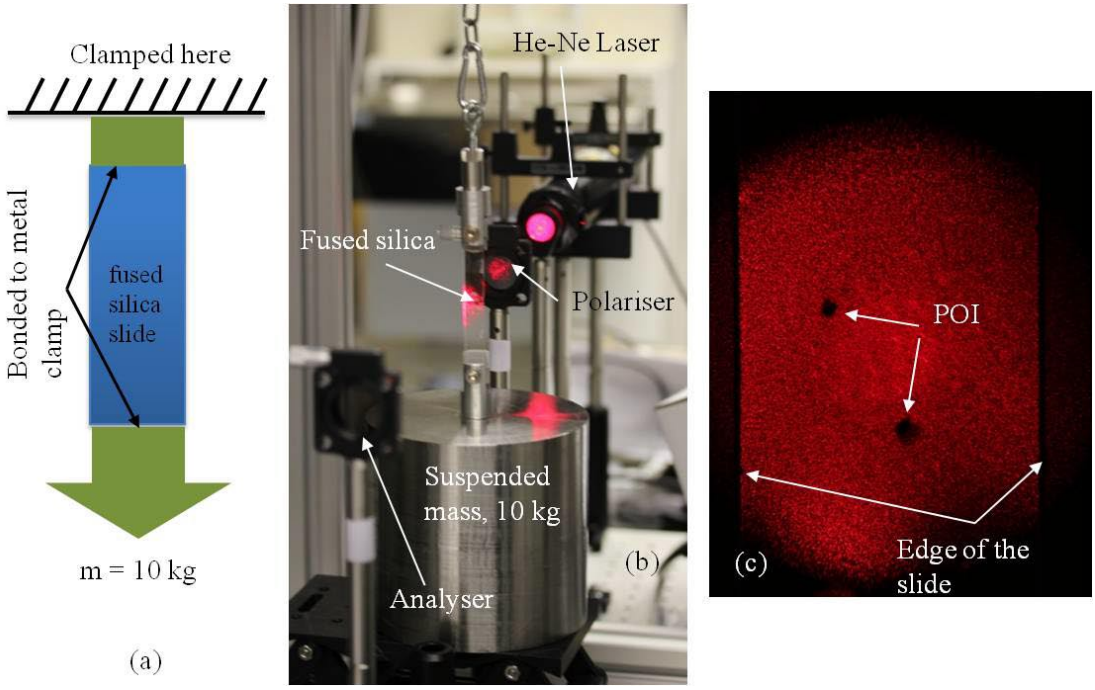

Figure 5.5 (a) Schematic of a silica slide suspending a 10 kg mass, (b) photograph showing the experimental setup (c) Image of the silica slide when viewed through a plane polariscope with crossed axis.

By measuring two different cases, where temporary birefringence has been induced in the fused silica by applying an external load, a method to successfully observe and measure the stress has been demonstrated. The measured stress in these cases has been verified theoretically with FEA. Hence more complicated cases, which involve residual thermal stresses are discussed in the next section.

5.3 Thermal stress in fused silica

Thermal stresses arise from temperature effects, which lead to rapid thermal expansion or contraction in a body. If a body is subjected to a slow uniform heating and the boundary surfaces are unrestrained then the entire body will expand uniformly in all the directions leading to thermal strain. However it will exhibit no thermal stresses despite showing thermal strain. The body will still be isotropic in nature and will show no double refraction in a photoelastic model [118].

If however there is a non-uniform rate of change of temperature then there will be a temperature gradient within the body. The temperature gradient will cause thermal expansion or thermal strain at hotter sections. The cooler areas will resist any thermal expansion. This combination of expansion and contraction leaves residual thermal stress in a body. This residual thermal stress remains stationary with time and hence is often referred to as frozen stress. The magnitude of the stresses will depend upon the material properties, temperature distribution and the degree of freedom the body has for free expansion [119].

The three dimensional thermal stresses are often difficult to analyse as the magnitude of stress integrates along the length of the sample. However, for thin planar samples (thickness less than 1 mm) the thermal stresses can be studied using the photoelastic procedures discussed in the previous chapter. A body of non-planar geometry, like a cylindrical rod is difficult to study and for such complicated cases the techniques developed in FEA can be used. Further complications arise due the fact that the material properties of the body often change with the rising temperature, hence for an accurate modelling of thermal stress in FEA these changes must be taken into account.

5.3.1 Heating of fused silica by applying a CO_2 laser beam

Fused silica (SiO_2) has a melting point of around 1700^0 C and has an extremely low thermal expansion coefficient of 5.5×10^{-7} $/^0$C (20 – 300 ^{0}C) [120]. The extremely low thermal expansion coefficient of fused silica makes it an ideal material for various applications involving high temperature operation. Figure 5.6 shows a plot of the viscosity of fused silica as a function of temperature [121]. Viscosity is the measure of the resistance to flow of a material when under shear stress. The annealing point in fused silica is at 1100 ^{0}C, where the internal stress at this temperature in relieved within 15 minutes. The softening point is between 1500 ^{0}C to 1700 ^{0}C and at this point the material becomes malleable and starts to flow. A full list of thermal properties of fused silica as a function of temperature is given in [122].

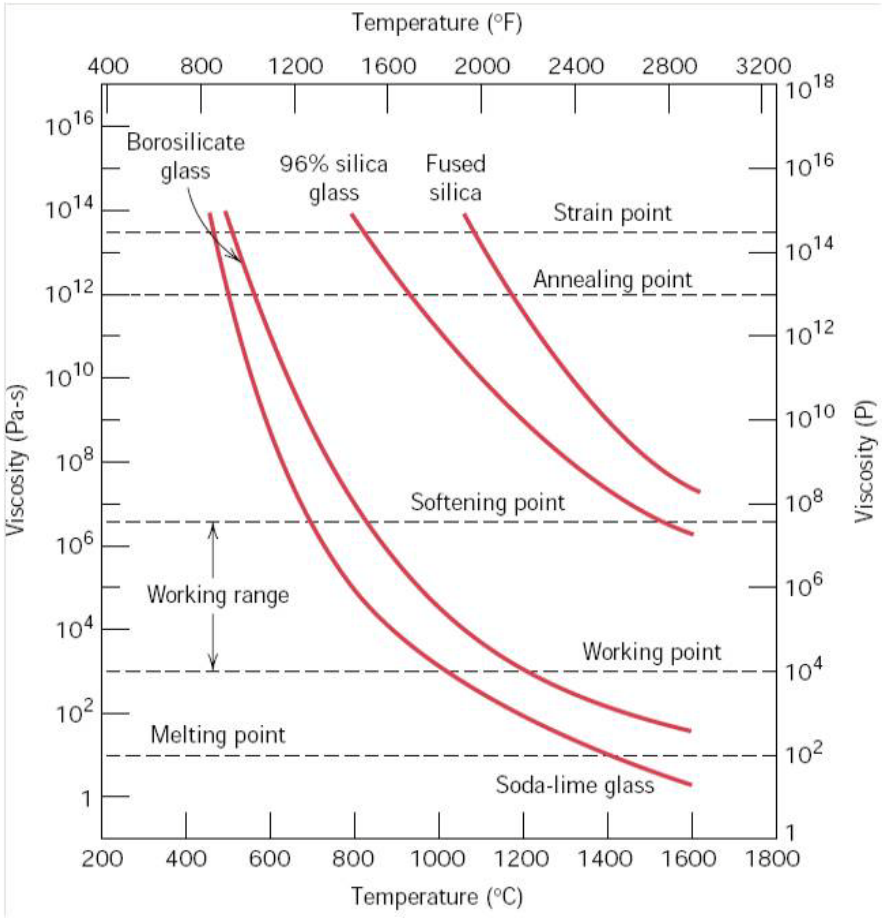

Figure 5.6 Plot showing viscosity of fused silica compared to other materials, as a function of temperature[121].

A 1 mm thin silica slide of planar geometry was used to study the thermal stresses induced in fused silica (Suprasil 2, grade A). The width of the silica slide was 10 mm, length 50 mm and was supplied by Heraeus. A 100 W CO_2 laser whose power can be varied was used to heat the sample. Initially to understand the relationship between laser power and the surface temperature of silica, the sample was heated by varying the power from 5 W to 40 W.

The surface temperature of the silica sample was measured using a platinum resistance thermometer. The thermometer used was a PT 100 with a temperature range of 0 to 900^0 C and the calibrations of resistance were obtained from Farnell, UK [7]. To measure the temperature above 1000 ^{0}C a Raytek made infrared pyrometer (Marathon MR series) was used. The operating range of the pyrometer was from 1000 ^{0}C to 3000 ^{0}C with an

emissivity of 0.9 for fused silica. The data from the pyrometer could be acquired using a software interface supplied by Raytek. Figure 5.7 shows the setup of the sample heated by the laser beam and the thermometer/pyrometer subsequently measuring the temperature.

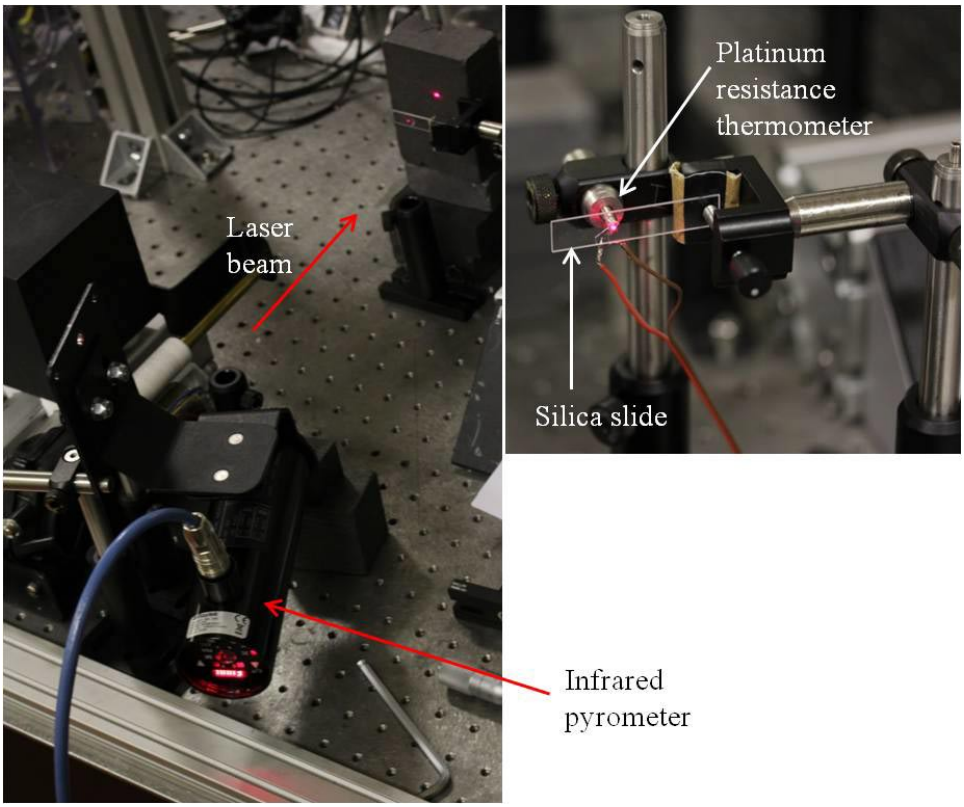

Figure 5.7 Fused silica sample (1 mm thick) heated by a CO_2 laser beam. The sample was monitored with a platinum resistance thermometer between 0 ^0C to 900 ^0C and an infrared pyrometer for measuring the temperature above 1000 ^0C.

The sample was clamped from one end and the platinum resistance thermometer was attached such that it was in contact with the rear face of the sample. A CO_2 laser beam having a diameter of 3 mm to 4 mm ($1/e^2$ width Gaussian profile) was used to heat the front face of the silica sample. The plot of temperature vs. laser power, which includes measurements from the thermometer and pyrometer, is shown in figure 5.8. The maximum temperature recorded by the pyrometer was around 1500 ^{0}C at 40 W after which the sample started to melt (the melting point of silica is around 1700

^{0}C). The average time taken for the surface temperature to reach 1500 ^{0}C and then stabilise was about 5-7 seconds.

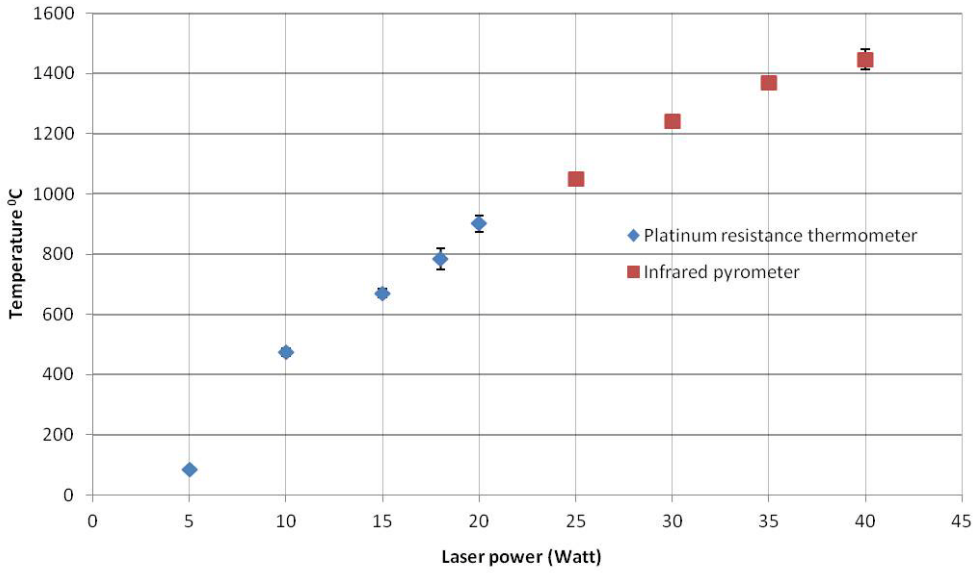

Figure 5.8 Plot of temperature vs. laser power for a silica slide heated by a laser beam, measured using a platinum resistance thermometer and an infrared pyrometer.

To observe and study the thermal stress in fused silica, another sample was heated using a 25 W CO_2 laser beam for 10 seconds. The laser power was kept relatively low to prevent melting of the sample, however it was high enough to induce anisotropy by changing the refractive index in the area where the heat was applied. The sample was then observed under a plane polariscope setup where the axis of the polariser and analyser were kept crossed to obtain a dark field image (as discussed in chapter 4). Figure 5.9 shows the isoclinic fringes obtained when the silica slide was observed under a crossed polariscope set-up similar to that shown in figure 5.1 (without the quarter wave plates), the light source used was a He-Ne laser. The thermal stress observed in the figure is analogous to a four-fold symmetric of petals in a flower, with a central circular core region where the laser beam was applied. This central circular region formed is approximately 4 mm in diameter, which is similar to the Gaussian ($1/e^2$) laser beam diameter. The black lines coming out of the circular pattern are the isoclinic lines. The direction of the principal stress coincides with the isoclinic pattern. The

difference in the intensity of the light signifies the varying retardation of light at different positions. The area just outside the inner circular region looks particularly bright as compared to other areas.

The sample was then rotated from 0^0 to 110^0 (with respect to the crossed axis of the polariscope) to observe the changing pattern of the isoclinic fringes. Figure 5.10 shows the fringes observed after every 10^0 of rotation. During this rotation the central circular region goes from bright to dark. The isoclinic fringes also appear to rotate in a circular fashion with the loci at the centre which signifies radial stress going outwards (from the point where heat was applied).

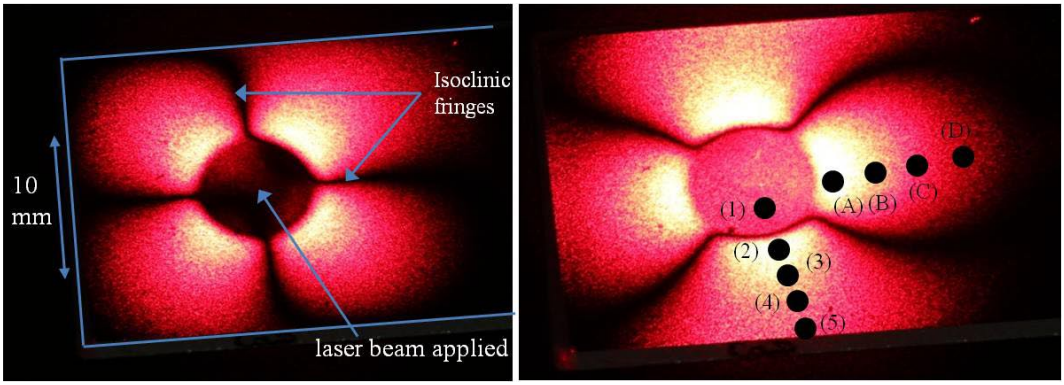

Figure 5.9 The isoclinic fringes observed for a silica slide heated by a 25 W laser beam for 10 seconds. The laser beam was applied at the centre of the petal shaped structure. The blue outline shown in the image on the left signifies the boundary of the silica slide which is 10 mm wide. The photograph on the right shows the various points of interest marked on the sample for measurement.

Figure 5.11 shows the isochromatic fringes due to thermal stress in silica observed under a circular polariscope set-up by inserting two crossed quarter wave plates between the crossed polarisers. The black dots (marked and unmarked ones) shown in the sample are the POI used for experimental measurements. The magnitude of the thermal stress was measured using the circular polariscope set-up. The isochromatic fringes were used to extinguish the intensity of light at the POI by rotating the analyser and the angle compensated is used to determine the retardation and ultimately the value of relative stress. A Soleil-Babinet compensator [7] was also employed to

measure the stress and compare the results between the two techniques. The procedure for using the compensator is discussed in the previous chapter. Several points of interest were marked at different places on the sample to measure the retardation and hence the magnitude of the stress. By taking measurements at several points, the distribution of stress as a function of distance could be obtained.

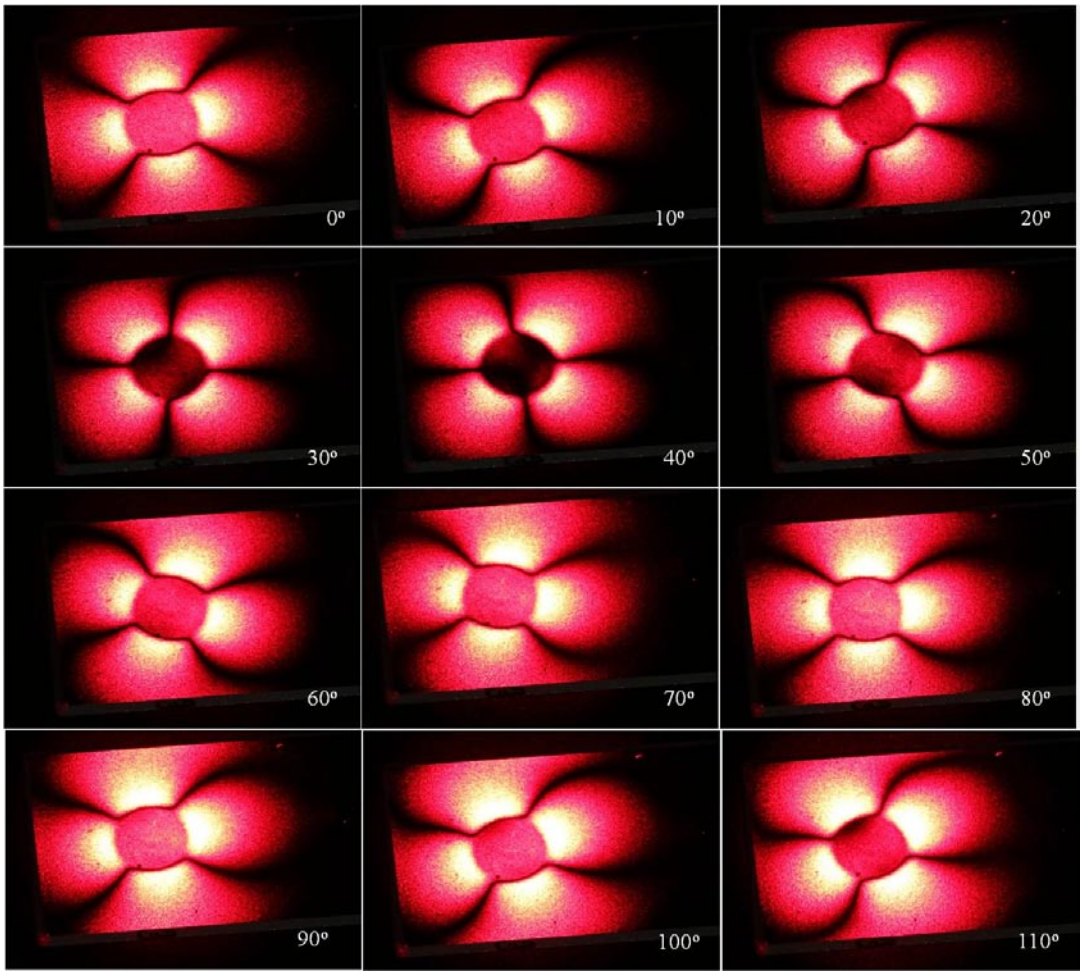

Figure 5.10 Thermal stress in a fused silica slide observed under a crossed polariscope which is rotated for different angles (from 0 to 110^0) to observe the changing isoclinic fringes.

Figure 5.12 shows the thermal stress measured as a function of radial distance, starting from the central circular region where the heat flux was applied. The stress measured within the central circular region is close to 2 MPa and this was found to be constant from the centre to 2 mm radial

distance. Maximum retardation was measured at points just outside the central circular region. These points correspond to POI - (A), (B), (2) and (3) which lie within the brighter areas having maximum intensity as seen in figure 5.9. The relative stress (with statistical errors) measured at these points varied from 13±0.23 MPa to 22±0.23 MPa. At a distance 4 mm to 6 mm away from the centre, the measured stress gradually decreases from 10±0.75 MPa to around 4±0.23 MPa. POI (5) which is 6 mm away from the centre and is near the edge of the silica slide shows higher stress by a factor of 2 as compared to POI (D) located at a similar distance (but in the middle of the sample). Looking at figure 5.10 POI (5) and (D) were measured to have a stress of 8 MPa and 4 MPa respectively.

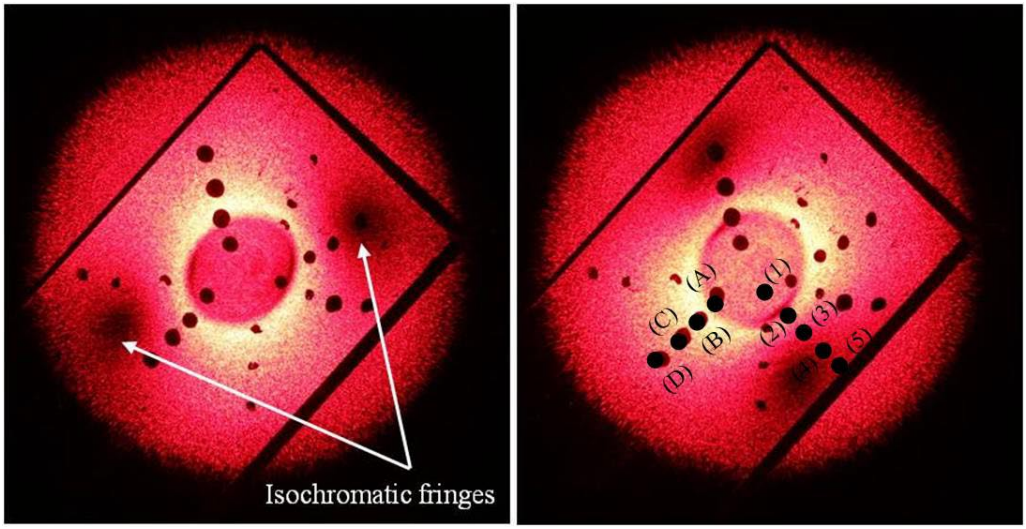

Figure 5.11 Isohromatic fringes obtained for a fused silica sample heated by a laser beam, observed under a circular polariscope setup. The black dots (numbered as well as non-numbered) are the points of interest where the measurements were taken. The sample was inverted (when compared with figure 5.9) while taking the image, hence POI (A) to (D) is in opposite direction.

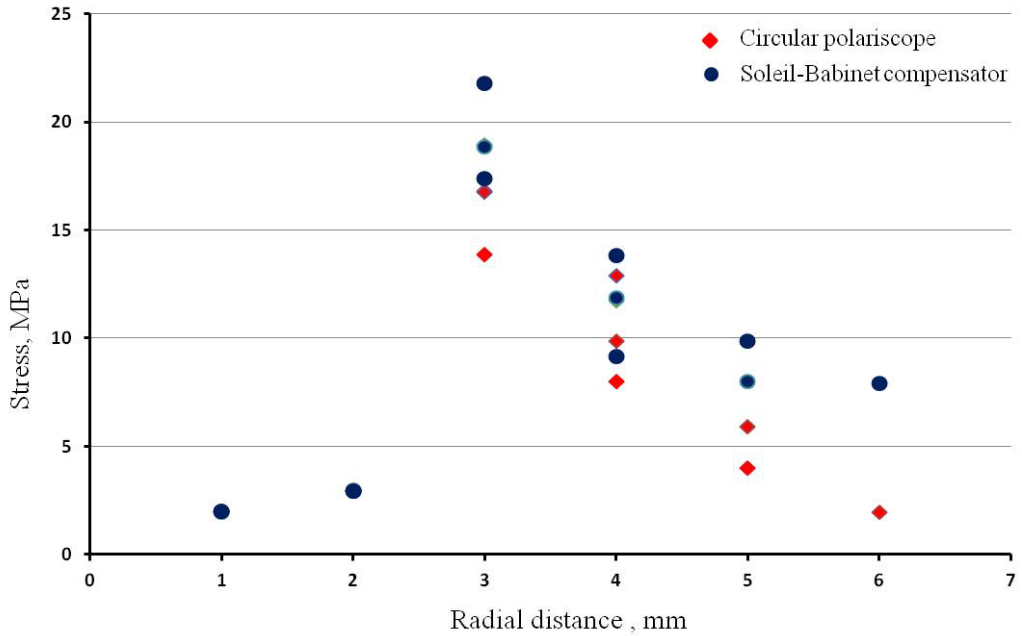

Figure 5.12 Thermal stress as a function of radial distance measured for a fused silica slide using a circular polariscope and Soleil-Babinet compensator.

5.4 Thermal modelling using finite element methods

FEA techniques were used for the thermal modelling of the fused silica slide to compare with the experimental results obtained from photoelasticty measurements. For the cases where the geometry of the sample will make it difficult to directly measure the thermal stress, an FEA model will help predict the temperature gradients and the resulting stress. However, it is also important to test FEA modelling on simpler planar geometries. A 'coupled field analysis' was used in ANSYS that combines two different analyses. Figure 5.13 shows a schematic of the steps involved in modelling a coupled field analysis in ANSYS [123]. The first step is to estimate the temperature distribution and thermal gradients in the body based on the loading condition applied. The model is then solved using a transient thermal analysis where the time is varied from zero to a few seconds. Next a transient structural analysis is used which requires a change in element type from thermal to structural elements. The temperature distribution obtained after solving the thermal analysis is re-applied on the body as a loading condition, to solve a structural analysis, thus giving thermal stress results.

A rectangular slide of dimensions - thickness = 1 mm, width = 10 mm, length = 50 mm was designed in ANSYS using solid element type (solid 95, which signifies 95 nodes per element). The model was finely meshed to obtain convergence of the results (< 1% difference). Figure 5.14 shows the finely meshed ANSYS model of the fused silica slide. The temperature dependent material properties of fused silica are required in the FEA model for accurate predictions. These include density; Young's modulus, Poisson's ratio, thermal conductivity, heat capacity and thermal expansion coefficient. The material properties used in ANSYS varied with the changes in temperatures, ranging from 25 ^{0}C to 1500 ^{0}C. To simulate radiation effects (between the hot body and the surrounding air) the radiosity solver method (RS solver) was adopted in ANSYS. A radiosity solver method is used to define radiation options in thermal analyses [124]. An additional element type called SURF 152 (2D), which is a surface element type, was specifically used to simulate radiation effects. Once meshed, ANSYS creates a new set of radiosity elements and nodes over the existing mesh (thus creating two different mesh types - surface mesh and body mesh). The radiation effects are dependent upon the Stefan Boltzmann constant and emissivity of fused silica, which was also provided.

A Gaussian beam of diameter 4 mm and power 25 W was used in ANSYS to simulate an equivalent heat flux generated from a CO_2 laser beam. The model was then solved for a transient thermal analysis for a time period of 10 seconds, with a time interval of 0.5 seconds. Using a small time sub-step of 0.5 seconds, the loading conditions are slowly applied on the model, which improves the convergence of the results. A large sub-step can result in large deformation (beyond the boundary set in ANSYS) and triggers a solution failure. The change in temperature of the solved model as a function of time was then studied using a '*time history post processing*' function in ANSYS and is shown in figure 5.15. The varying temperature with time was measured at the point where the heat flux was applied. The plot shows that the system reaches at a steady state within 10 seconds, as the temperature doesn't change significantly beyond that time.

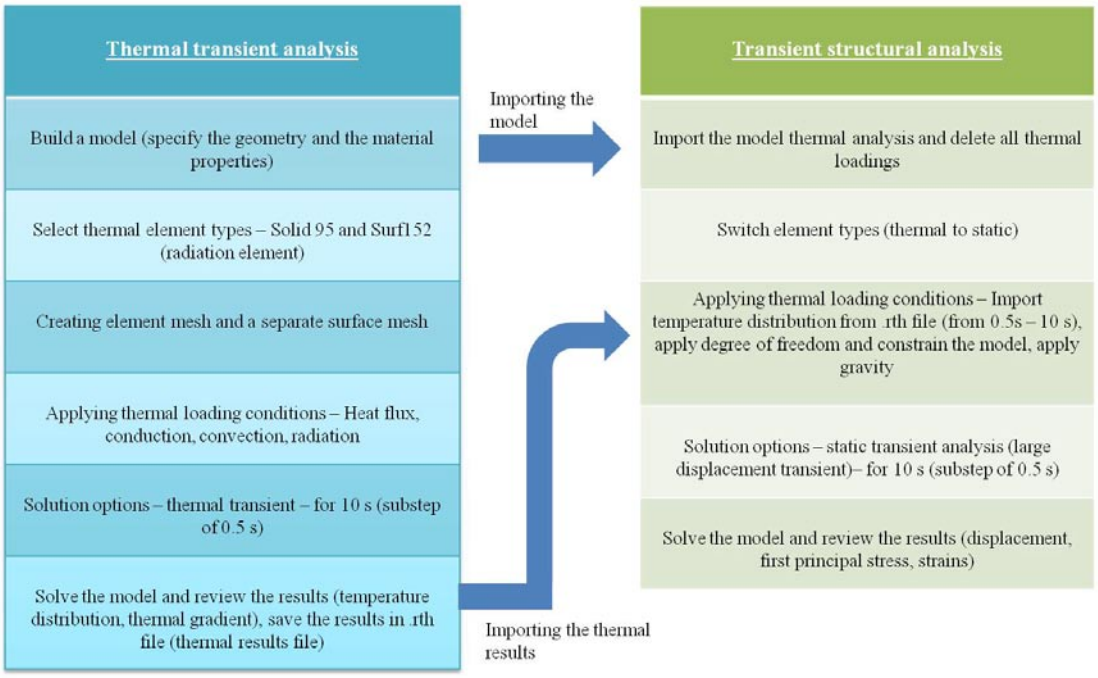

Figure 5.13 Schematic of the steps involved in solving a coupled field analysis in ANSYS.

The temperature profile of the body is estimated in ANSYS using the Fourier law of conduction. It states that the rate of change of heat flux through a body is directly proportional to the area, at right angle to the direction of heat flow and to the negative temperature gradient along the path of heat flow. The heat flux q is expressed as [119, 125],

$$q_{heat\ flux} = -KA\frac{dT}{dx}, \tag{6.1}$$

where A is the cross sectional area through which the heat flows, K is the thermal conductivity of the material and dT/dx is the temperature gradient. The negative sign ensures the heat flows down the temperature gradient.

The radiation contributes a negative term to the heat flow because it decreases the energy in the body. The amount of radiation depends upon the temperature of the body and the emissivity. The rate of heat flow due to the radiation emitted by a body is given by,

$$q_{radiation} = e\sigma AT^4 \tag{5.2}$$

where $\sigma = 5.67 \times 10^{-8}\mathrm{Wm^{-2}K^{-4}}$ is the Stefan-Boltzmann constant.

The temperature distribution within the body depends upon the rate of heat generation (q_{gen}), the heat capacity and rate of thermal conduction to its boundaries and surrounding environment. The heat generation q_{gen} within the body is also roughly equal to the heat flux applied and the heat loss due to radiation effects. This is determined by the equation, which is expressed as [119],

$$\frac{d^2T}{dx^2} - \frac{1}{\kappa}\frac{\partial T}{\partial t} = -\frac{1}{k}q_{gen} \tag{5.3}$$

where $\partial T/\partial t$ is the rate of change of temperature at a point over time and κ is the thermal diffusivity which describes the rate at which heat diffuses through a body. κ is dependent upon the thermal conductivity k and specific heat capacity c. The thermal diffusivity (unit- m/s^2) increases with thermal conductivity as the heat will be able to conduct quickly across the body. However a higher heat capacity will lead to heat being stored as an internal energy within the body instead of being conducted thus lowers the thermal diffusivity. Mathematically this is given by [125],

$$\kappa = \frac{k}{\rho c} \tag{5.4}$$

where ρ is the density of the material.

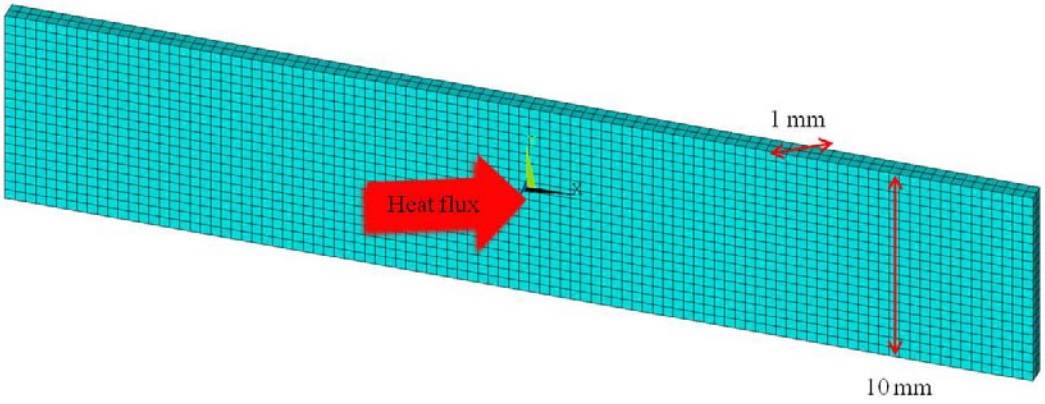

Figure 5.14 ANSYS model of a meshed fused silica slide, showing the position of the applied heat flux.

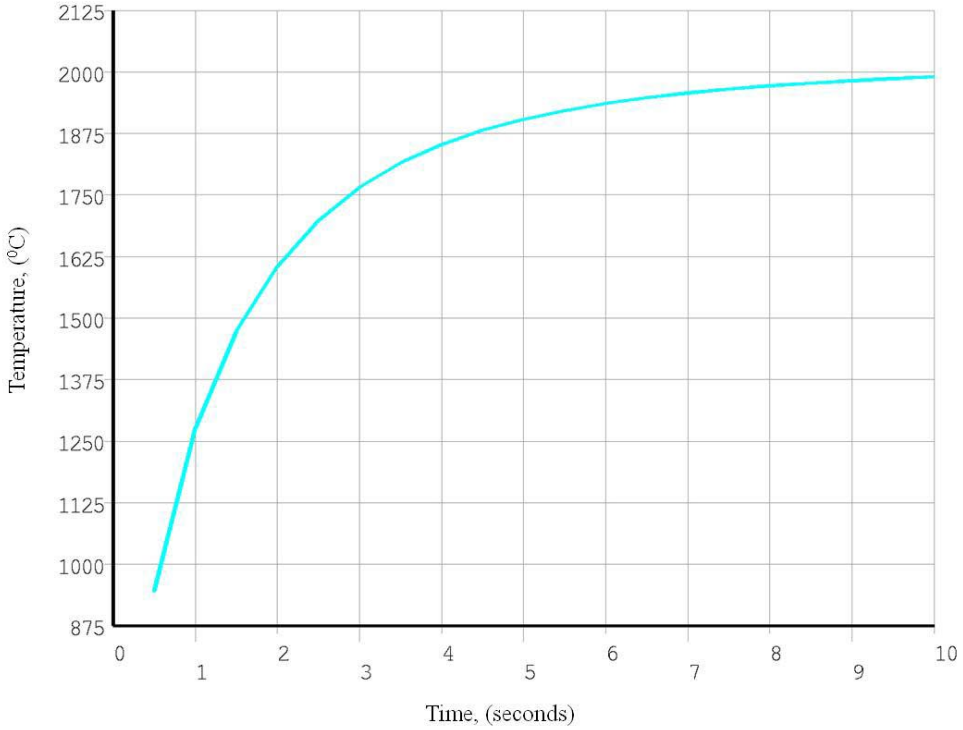

Figure 5.15 A plot from ANSYS showing the temperature vs. time measured at the centre of the fused silica slide, where the 25 W laser beam was applied.

Figure 5.16 shows the time varying (from 1 sec to 10 sec) temperature profile in the body obtained after solving the model in ANSYS. The region where the Gaussian beam was applied shows a maximum temperature of 2070^0 C after 10 seconds. At the same time the rear surface of the silica sample roughly attains a maximum temperature of 1600 ^{0}C within 10 seconds, which is shown in figure 5.17. Recalling, that the temperature at the rear surface of the fused silica measured using the pyrometer to be $\cong$ 1500 ^{0}C, which is close to what is estimated in the FEA model.

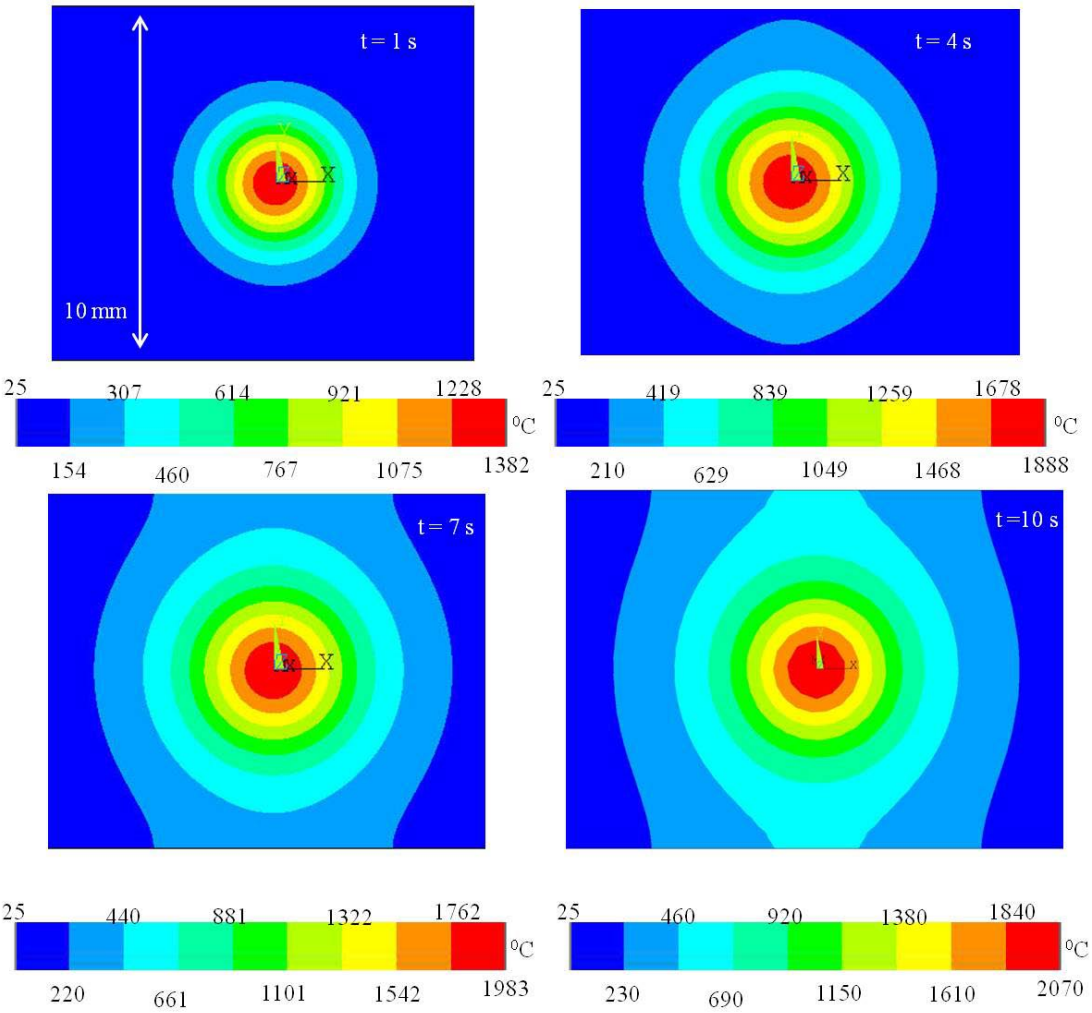

Figure 5.16 Temperature distribution at the front surface of the fused silica slide estimated from the FEA model, showing the time varying (1s to 10 s) distribution of temperature (in ^0C). The simulation was based on applying a 25 W Gaussian beam on the model for 10 seconds.

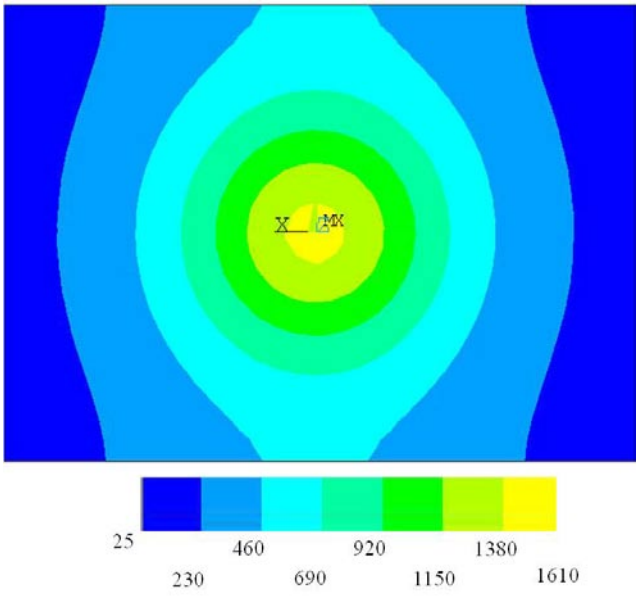

Figure 5.17 Temperature distribution at the rear surface (relative to the surface where the heat flux was applied) of fused silica due to laser heating (25 W) for 10 seconds.

The estimated thermal gradients in the x, y and z directions are shown in figure 5.18. The x and y axes are along the surface of the sample and z is perpendicular to the page (i.e. along the 1 mm thin axis of the sample). The thermal gradients plotted in red and blue contours (specifically in (a) and (b) of figure 5.18) are of similar magnitude but opposite in direction. The thermal gradient is minimum at the surface where heat flux was applied, which is shown in green. At distances 2-3 mm away from the source of heat flux the thermal gradient is maximum in the x and y directions.

Figure 5.18(c) shows the thermal gradient along the z axis, where most of the heat flux is getting absorbed within the sample. The magnitude of the thermal gradient in this case is higher as compared to the other two cases (x, y directions).

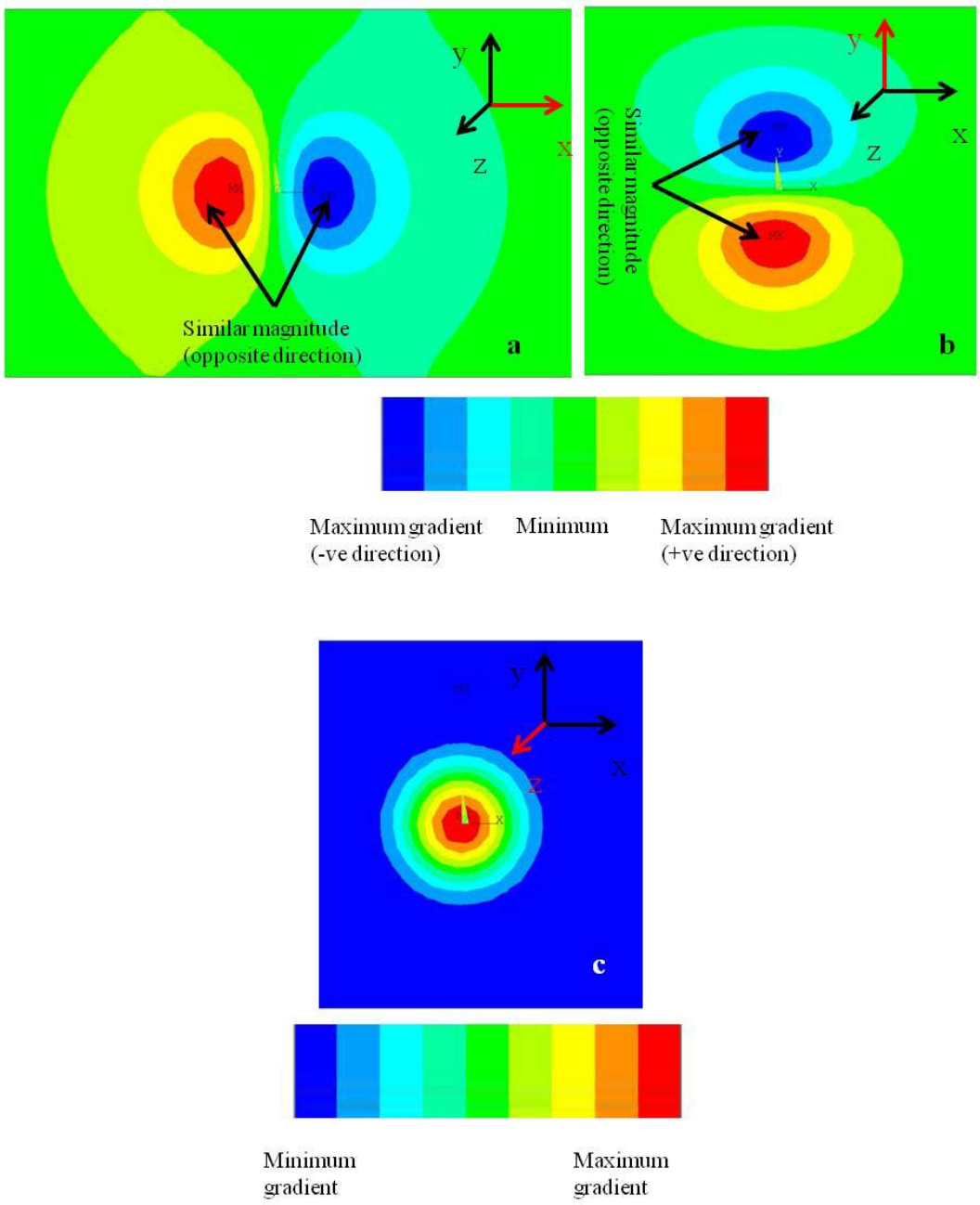

Figure 5.18 Thermal gradient in the fused silica slide on applying a 25 W laser beam. (a, b) thermal gradient in the x and y axes respectively, the contours shown (red-blue) are similar- in magnitude but in opposite direction, the contour in green indicates a minimum value, (c) thermal gradient along the z axis (perpendicular to the page) where the contour in red shows maximum values and blue is for minimum values.

Based on the results obtained from the transient thermal analysis a transient structural analysis was setup. The distribution of temperature in each element of the body was carried forward (from the thermal analysis) and applied as a loading condition for individual time intervals. Figures 5.19 and figure 5.20 shows the development of thermal stresses from 1s - 4 s and 7s - 10 s respectively, obtained after solving the transient structural analysis. The equivalent stress (Von Mises stress) and 1st principal stress developed in the body over 10 s has been compared in the same figure. Equivalent stress is the scalar stress value which is a combination of the three principal stresses. The equivalent stress can be used to estimate the yield stress of the material, exceeding them will result into failure (melting in the case of fused silica) of the sample. The development of the thermal stresses with time (in figure 5.19, 5.20) can be compared with their respective temperature profile from 1s to 10s (figure 5.16).

Figure 5.21 shows a comparison of the results obtained from the FEA model with those measured using the techniques of photoelasticity. The experimental relative stress should be compared only with the 1st principal stress estimated from FEA. In the area where the heat flux is applied (the inner circular contour in blue in figure 5.20) the 1st principal stress varies from – 1.17 MPa to 1.79 MPa at a time 10 sec. The negative sign signifies the direction of the stress component. Experimentally the stress in this area was measured to be approximately 2 MPa and is close to the estimated 1st principal stress. The corresponding equivalent stress at time 10 s varies from 22.5 MPa to 33.7 MPa, which is very high as compared to the measured value. The stress in the core region could be three dimensional in nature and should vary as a function of thickness. The temperature in this core region was estimated from FEA to be varying from 1150 ^{0}C to 2000 ^{0}C as shown in figure 5.16. Hence a large thermal gradient is observed at this point (figure 5.18). The temperature in this region is near the melting point of fused silica, hence the viscosity will change from 10^{14} Pa-sec to 10^7 Pa-sec. Under these circumstances the material is expected to soften and flow. To determine the correct stress in the core area will require a computational fluid dynamics (CFD) analysis in ANSYS [126].

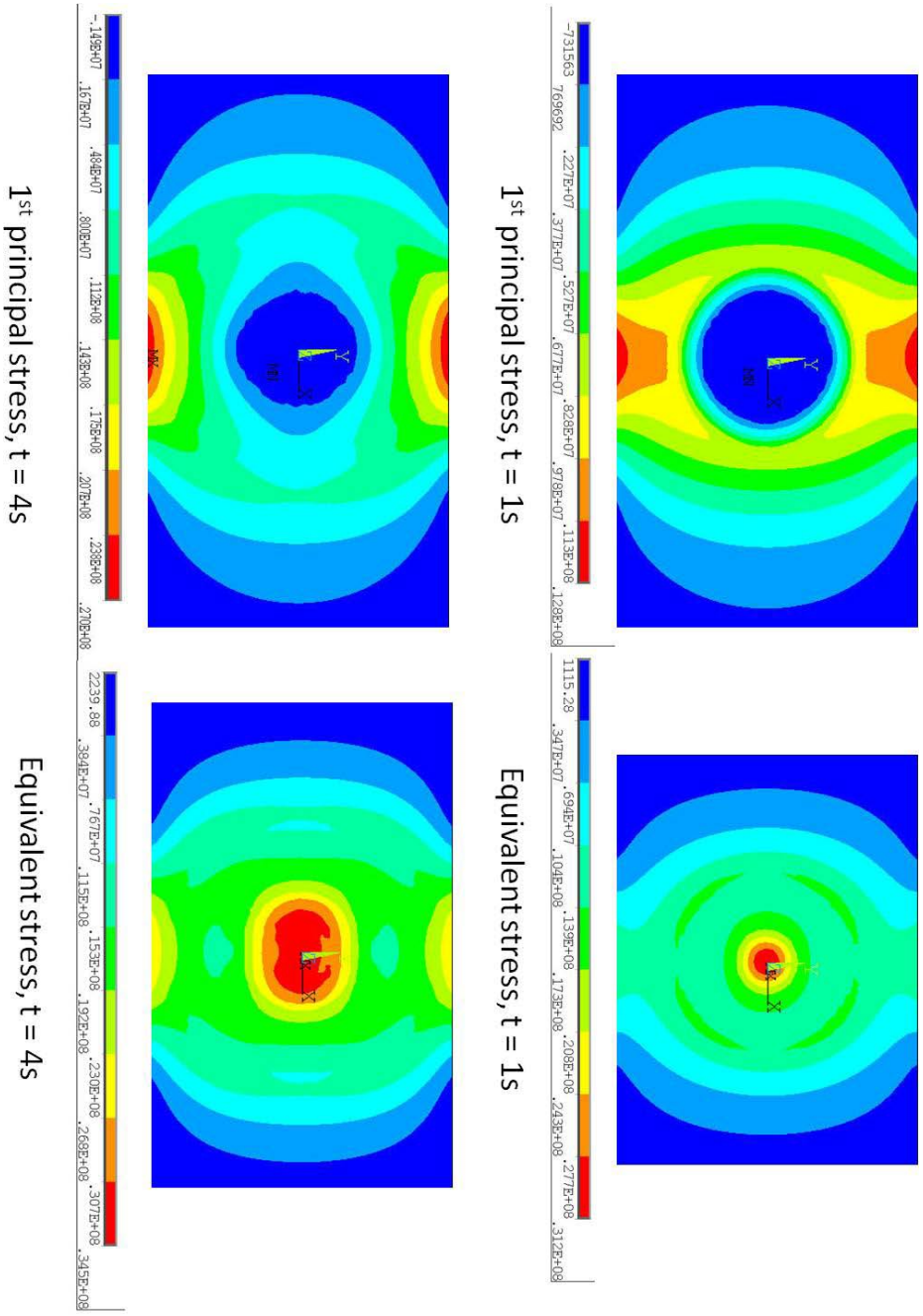

Figure 5.19 ANSYS modelling of a fused silica sample showing thermal stresses on applying a Gaussian heat flux (25 W laser beam). The stresses shown are the 1st principal stress and equivalent stress for times 1sec and 4 sec.

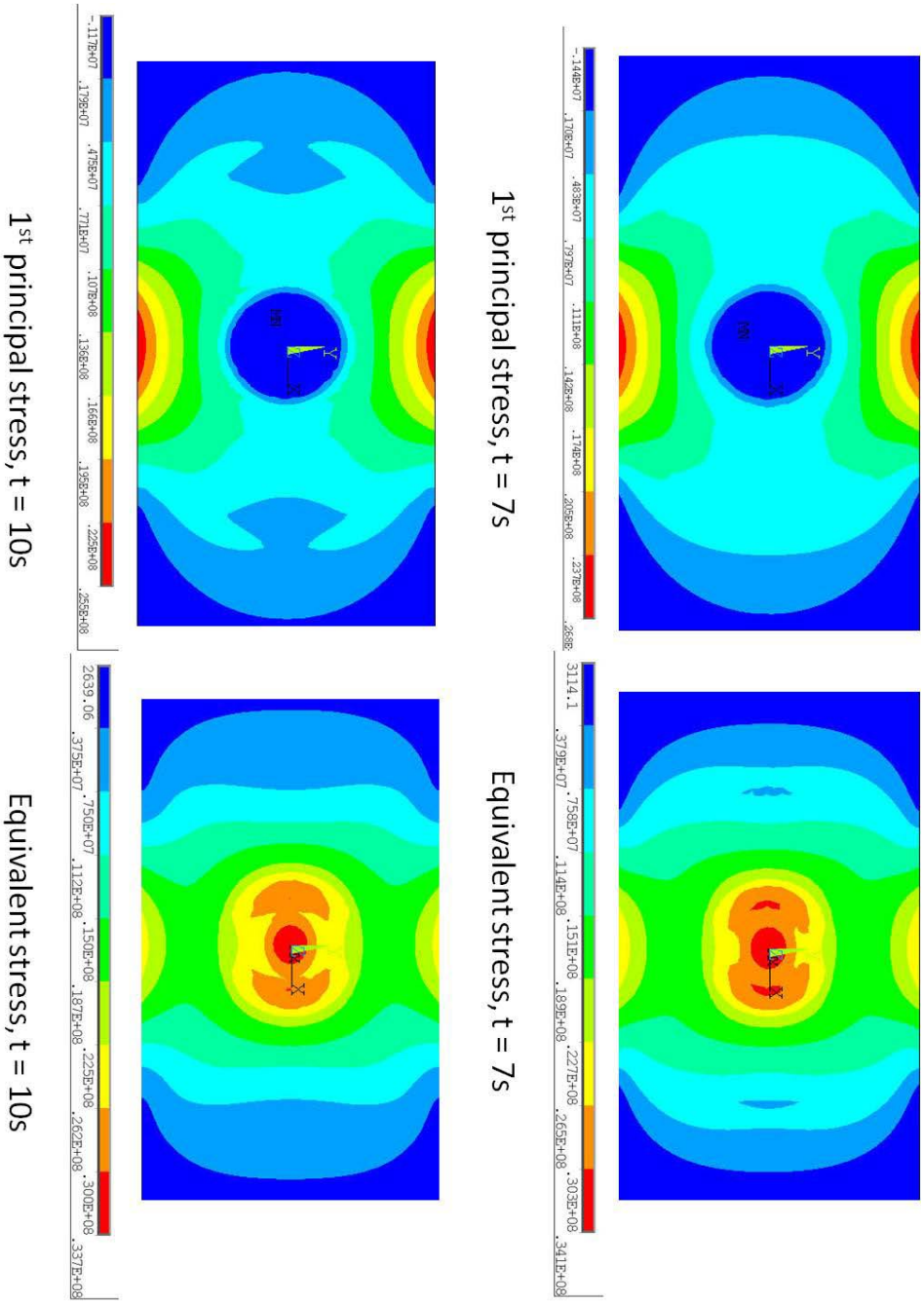

Figure 5.20 ANSYS modelling of a fused silica sample showing thermal stresses on applying a Gaussian heat flux (25 W laser beam). The stresses shown are the 1st principal stress and equivalent stress for times 7 sec and 10 sec.

However as heat is distributed around the body the equivalent stress gradually increases at the region outside the inner circle (radius 2 mm). At a distance 3 mm from the centre the equivalent stress was estimated to be 18.7 MPa with a variation of 5 MPa depending upon the radial position. These values agree closely to the value measured experimentally, which is 18 MPa.

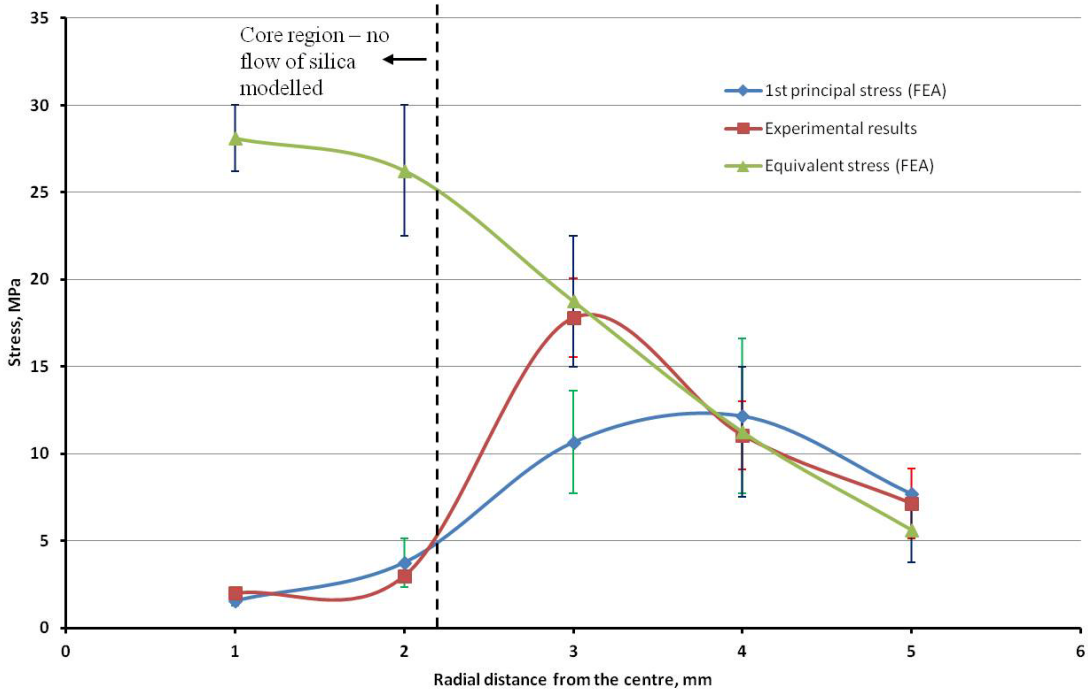

Figure 5.21 A comparison of the thermal stresses in a fused silica slide measured using photoelasticity and predicted with a FEA model. The values along the horizontal axis are the radial distance measured from the point where the heat flux was applied. The error bars represent the range of the stress values measured at several points located at the same radial (in x and y directions) distance.

5.5 Thermal stress in fused silica welds

The suspension systems in the advanced gravitational wave detectors such as aLIGO have fused silica fibres welded to silica attachment ears. The welding is done using a 100 W CO_2 laser beam. The weld region will contain residual thermal stress developed during this process. The stress in the welds may weaken the stock region of the fibre, which could reduce the breaking stress of the suspension. The stress in the weld region may also increase the weld loss [127, 128] which could increase the total mechanical loss and thermal noise of the suspension. In future detectors there are plans to use heavier test mass and thicker fibre stock to support the mass, which could involve welding using higher power laser. Keeping in mind these issues, the study of thermal stress is particularly important for the development of future detectors. However it is very difficult to directly observe and study the weld stress due to the complex geometries involved. Hence to investigate weld stress during laser welding two silica samples were welded together using a CO_2 laser beam. These samples have planar geometry (similar to the one used in the previous section) which makes it possible to directly observe and measure the stress around the weld region.

Figure 5.22 shows the set-up used for welding two fused silica samples together. The set-up includes a computer controlled (via LABVIEW interface) 'x-y' mirror galvanometer and an articulated arm for directing the laser beam into the galvanometer. The mirror galvanometers reflect the laser beam towards the silica sample, which will be welded. The movement of the galvanometers are computer controlled which allows the laser beam to move around in the horizontal and vertical directions on the sample.

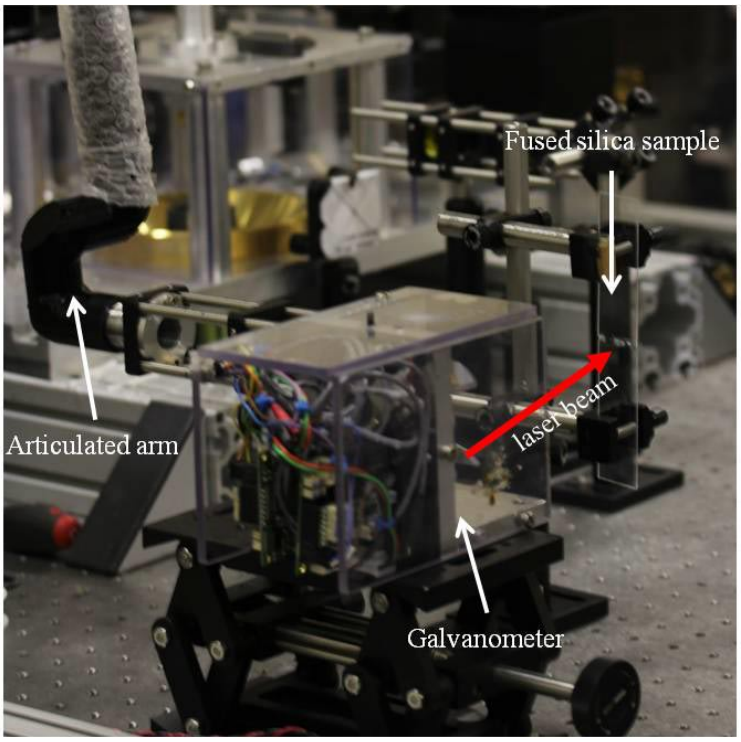

Figure 5.22 Set-up used for welding two fused silica samples together using a CO_2 laser beam. Mirror galvanometers, which are computer controlled, are used to direct the laser beam on to the sample.

The samples to be welded are held using ceramic tipped tweezers, which are attached to three axes stages (similar to one used for holding GEO fibres during flame welding as described in chapter 3). The laser power was varied between 30~60 Watts during the process of welding. The silica sample softens on applying the laser beam for a few seconds and the two samples are then gently pushed towards each other to form a weld. It takes approximately 5 minutes of continuous laser power to weld a 10 mm wide silica sample. Figure 5.23 shows three fused silica samples (a, b, c) of different width, which were laser welded.

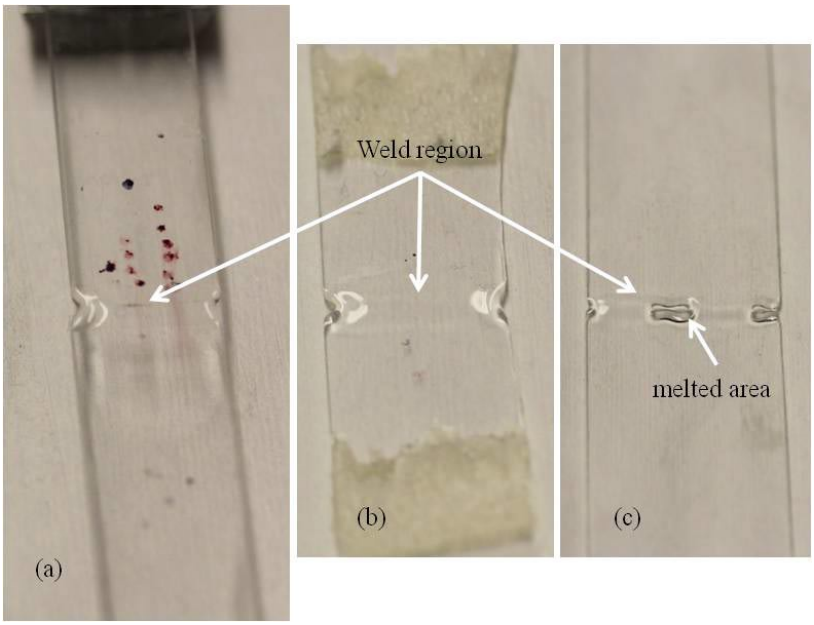

Figure 5.23 Fused silica samples welded together using a CO_2 laser beam. Sample (a) is 10 mm wide, sample (b) and (c) are 12 mm and 15 mm wide, respectively.

The welded samples were then placed in a crossed polariscope set-up to observe the thermal stress developed due to welding. Figure 5.24 shows the isoclinics obtained under a crossed polariscope for all three samples. The weld line remains dark for any angular rotation of the polariser. One reason for this could be due to the fact that the sample in this region might have annealed due to high temperature, hence might not be showing any sign of birefringence. The weld region is 4~5 mm wide (±2.5 mm from the weld line shown in figure 5.24). At the periphery of the weld region a distinctly sharp line can be seen (see figure 5.24). This line divides the hot (molten) and relatively cooler parts in the sample. Also a change in the refractive index is observed at either side of this sharp line. Outside the weld region, maximum intensity of light can be observed, which suggest that the light suffers maximum retardation in this region.

Figure 5.25 shows the changing pattern of the isoclinics obtained by rotating the sample (a) at every 10^0 interval in a crossed polariscope set-up. Several POI were marked on the sample and using the changing isoclinics, the principal stress direction was identified. The value of retardance was measured at marked POI using the Tardy method of compensation, to give an estimate of the thermal stress distribution in the sample.

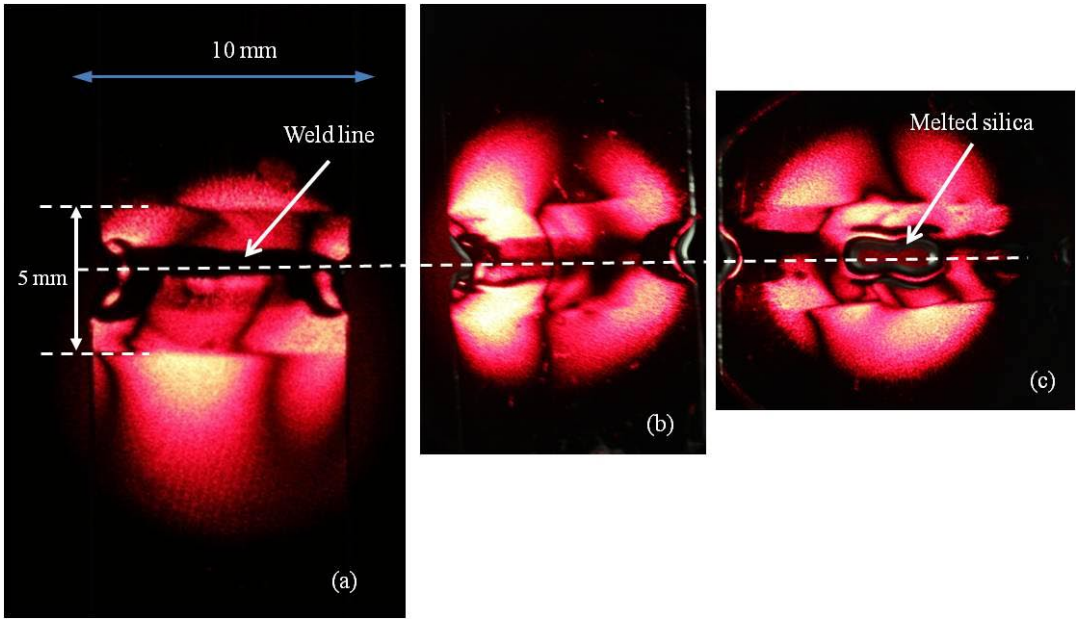

Figure 5.24 Thermal stress in fused silica samples (a, b, c) developed due to laser welding, observed under a crossed polariscope set-up. The weld region shown in sample (a, b, c) extends ±2.5 mm beyond the weld line in both directions.

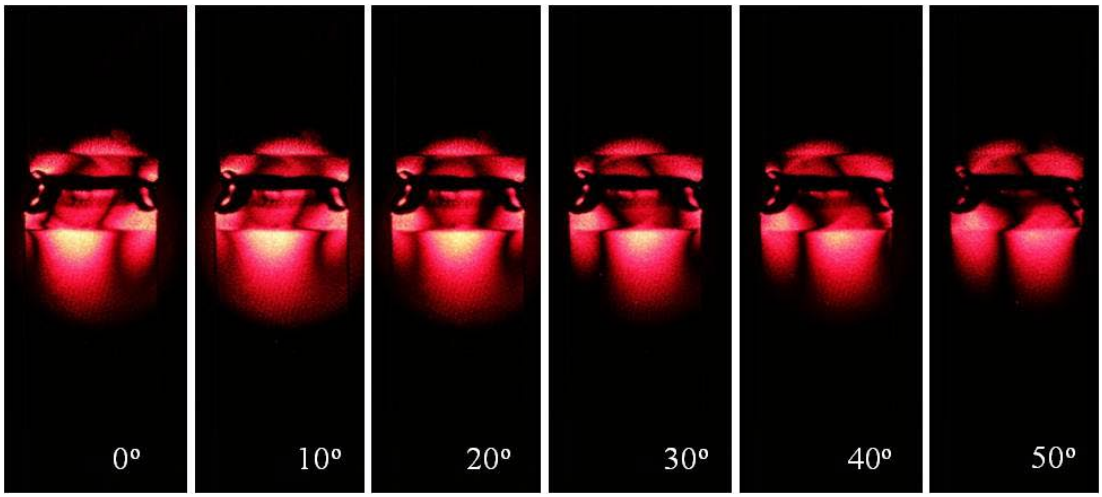

Figure 5.25 Sample (a) rotated at every 10^0 interval under a crossed polariscope to obtain changing isoclinic patterns formed due to thermal stress in the laser welded silica.

Figure 5.26 shows the retardance measured as a function of distance from the weld line. The weld line is at zero position in the plot and the line drawn on the plot is to identify the weld region. The photograph of the thermal stress in figure 5.26 is scaled (along the x axis) with the plot to show the position of the measured POI. The weld region shows a uniform retardance of 10 nm (for the 633 nm He-Ne laser). The retardance increases by a factor of 5 and peaks just outside the weld region.

Figure 5.27 shows the relative stress along the length of the sample, measured for sample (a) in the positive and negative direction from the weld line. The distribution of stress in both the directions shows a similar trend. The stress remains constant in the weld region and peaks just outside it, followed by a reducing trend along the length of the sample. The stress in the entire weld region varies between 3±0.2 MPa to 4±0.2 MPa. Maximum stress is observed just outside the weld region (3 - 4 mm away from the weld line) and was measured to be 15.85±0.42 MPa. The thermal gradient outside the weld region could be very high due to the interface of hot and cooler parts that leads to very high stress observed in this area. These results are interesting and further work is required to develop methods through which samples can be annealed. A welded sample can be placed in an oven and the annealing temperature could be set at 1100 ^{0}C. Isoclinic patterns of the annealed samples can be compared with the non-annealed ones. Measurement of relative stress in these samples could show a change in the distribution of stress.

It is important to note that the existing FEA models do not take into account the flow of silica. The model doesn't use the changing viscosity of fused silica, which is vital for the most accurate prediction of thermal stress in the weld region. Hence further techniques need to be developed which could simulate the flow of molten silica in the weld region, using computational fluid dynamics (CFD). This could involve solving for three different analyses: transient thermal, thermal fluid (CFD) and finally transient structural. The assimilated results from these analyses can give more insight into the flow dynamics of molten silica. These results could be useful for annealing the sample to reduce the residual thermal stress.

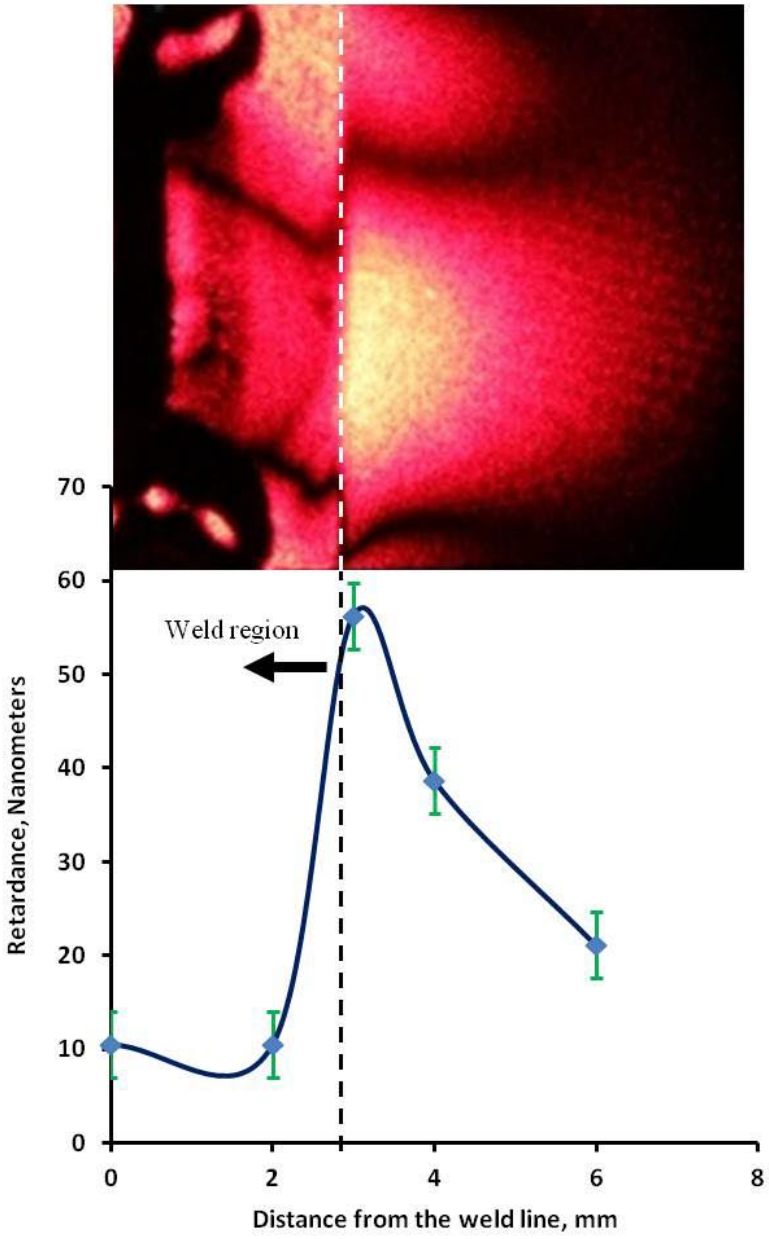

Figure 5.26 Plot of retardance as a function of distance from the weld line (at zero position) estimated for sample (a) using the Tardy method of compensation. The photograph of the thermal stress is scaled to the x-axis of the plot to show the position of the POI from the weld line.

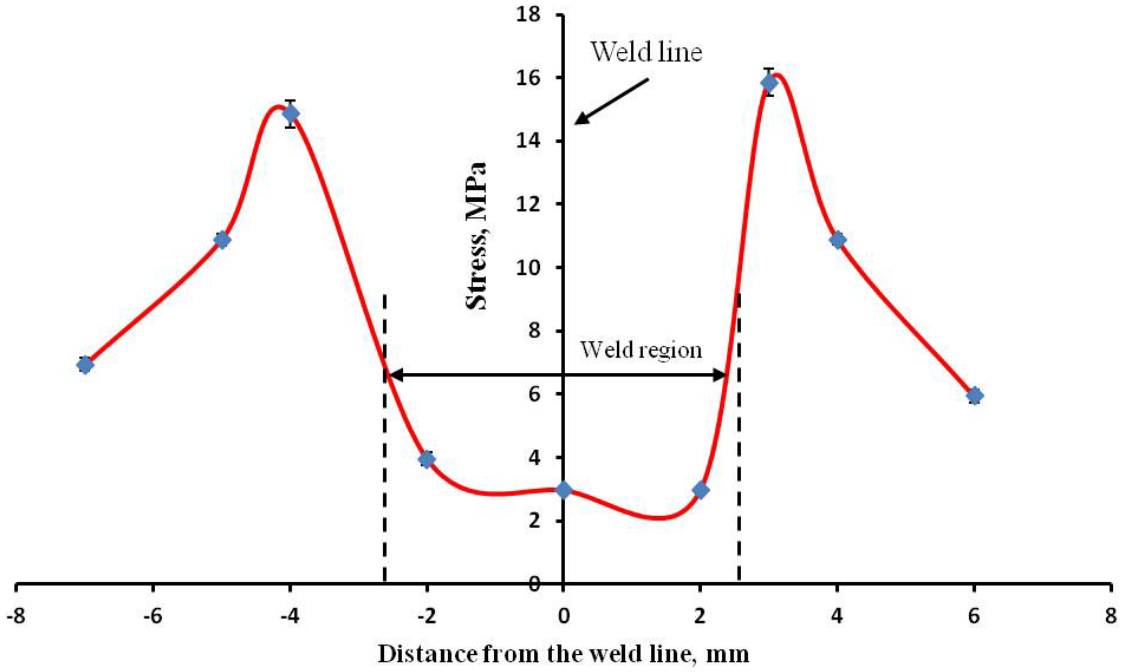

Figure 5.27 Plot of relative stress as a function of distance measured for the laser welded sample (a). The y-axis is also the weld line in the sample, the stress was measured in both the positive and negative directions from the weld line.

5.6 Conclusions

Fused silica being optically isotropic exhibits no birefringence when zero stress is applied. However temporary anisotropy can be induced in it by applying a mechanical load or by heating a sample. Mechanical bending load was applied on the fused silica cantilever to measure the retardance and estimate relative stress using the photoelastic stress analysis. Similarly a silica slide was loaded with a 10 kg mass and tensile stress was observed and measured at several points. The experimental results were then compared theoretically and using a FEA model. The photoelastic method gives a good method for determining stress values with a resolution of ±1 MPa.

The photoelastic stress analysis technique was then used to study and estimate the thermal stress in a fused silica slide. The silica slide was heated by applying a 25 W CO_2 laser beam. The rising temperature in the sample was measured using a platinum resistance thermometer and an infrared

pyrometer. The thermal stresses were observed under a plane polariscope and later under a circular polariscope set-up. Under a plane polariscope the changing isoclinic pattern was observed. The isoclinics were removed under a circular polariscope to obtain isochromatic patterns. The magnitude and directions of the stress were analysed using the Tardy method of compensation and a Babinet-Soleil compensator. A coupled field analysis (thermal + structural) in ANSYS was performed to estimate the distribution of temperature in the body and the thermal gradients. The temperature predicted by FEA model agrees with the values measured using the infrared pyrometer. The thermal solutions were then solved for a structural solution to obtain thermal stresses. Experimental results suggested a high degree of relative thermal stress in the sample at various points. This varied from 22 MPa to 2 MPa depending upon where it was probed. At a distance 3 mm to 5 mm from the centre the results from the experiments and FEA showed a good agreement with some degree of deviation.

The study of thermal stress encouraged further study of more complicated cases like weld stress. Two fused silica samples were welded using a CO_2 laser beam and the thermal stresses around the weld region were studied. The relative stress measured experimentally in the weld region was found to be comparatively lower than other areas. The relative stress values peaks at a distance 3 mm to 4 mm away from the weld line.

The currently used FEA model does not simulate the flow of molten silica. Hence the prediction of stress in the weld region using FEA requires further work, which could include a study of computational fluid dynamics. Modelling complex geometries like cylindrical rods requires more work in this area. These models could be vital in predicting the thermal stress in cylindrical silica stock laser welded to silica ears.

The work in this chapter has demonstrated an effective technique, which can be used to study the mechanical and thermal stress in fused silica. The experimental stress analysis and the thermal modelling in FEA could be further used to analyse stresses developed in the materials used for the construction of suspension elements in gravitational wave detectors.

Chapter 6 Incremental upgrades for improving suspension thermal noise in advanced LIGO

6.1 Introduction

The 4 km long advanced LIGO (aLIGO) detector is a 2nd generation gravitational wave detector, which is currently under construction at two sites in the USA [129]. The detector is expected to be online by 2016 and achieve the design sensitivity within 2-3 years. The design sensitivity of aLIGO is a factor of 10 better than the first generation LIGO detectors at frequencies less than 10 Hz [130]. This may result in the event rate of binary neutron star coalescences of approximately 40 per year [11]. This has been possible by using ultra low loss materials and monolithic fused silica suspension, optimised mirror coatings and advanced interferometer optics. These upgrades could lead to a first possible detection of gravitational waves in the next 4~5 years. However it is important to study the possibility of applying incremental upgrades to the second generation detectors by making small but significant changes to the suspension system. The work in this chapter discusses the various incremental upgrades possible in the current suspension design to further reduce the mechanical loss. This work could lead to improvement in the suspension thermal noise which will improve the sensitivity of the detector by a factor of ~3-4.

6.2 Overview of the aLIGO suspensions

The design of the aLIGO suspension is based on the suspension system used in the GEO-HF detector [131]. However the aLIGO detector has more stringent thermal noise requirements, especially at frequencies below 100 Hz. The details of the suspension design and fabrication procedure have been presented in [132, 133] . The baseline displacement sensitivity of the detector is 10^{-19} m/√Hz at 10 Hz. Any technical noise source should be 10^{-20} m/√Hz or lower at 10 Hz. The vertical mode frequency is expected to be 12 Hz or lower and the fundamental violin mode should be around 500 Hz. Hence the suspension technology from the GEO-HF detector has been further developed to meet these requirements. The main mirror suspension for aLIGO is designed as a quadruple pendulum having a monolithic fused silica final stage. Figure 6.1 shows the fused silica suspension installed in the LIGO Advanced System Test Interferometer, LASTI, MIT [134]. The LASTI monolithic suspension was essential for measuring the fundamental violin mode quality factors, which would provide a test of the FEA modelling techniques used to predict the mechanical loss. The violin mode was excited using magnetic actuators and the subsequent ring down was recorded in the cavity lock acquisition signal. The loss measured for the fundamental (1.6×10^{-9}, 516 Hz) and the first harmonics (2.2×10^{-9}, 1020 Hz) agreed within 7% and 19% respectively, with the FEA model (1.5×10^{-9} and 1.8×10^{-9} respectively) [133].

The quadruple pendulum design has four multiple pendulum stages, which are shown in figure 6.2. There are two metal masses suspended from cantilever springs made of maraging steel. The 40 kg fused silica penultimate mass hangs from the upper mass using steel wire in a loop. The final monolithic stage consists of another 40 kg fused silica test mass. The test mass is suspended from the intermediate mass using four fused silica fibres of length approximately 602 mm. These fibres have varying cross section and the thinnest section has a diameter of 400 μm. The fused silica fibres are welded to the horns of the silica ears using a CO_2 laser. The silica ears are bonded to the sides of the test/penultimate mass using a hydroxide catalysis bonding technique [101]. The sides of the test mass have a flat surface (polished to $\lambda/10$ (633 nm) especially for this purpose.

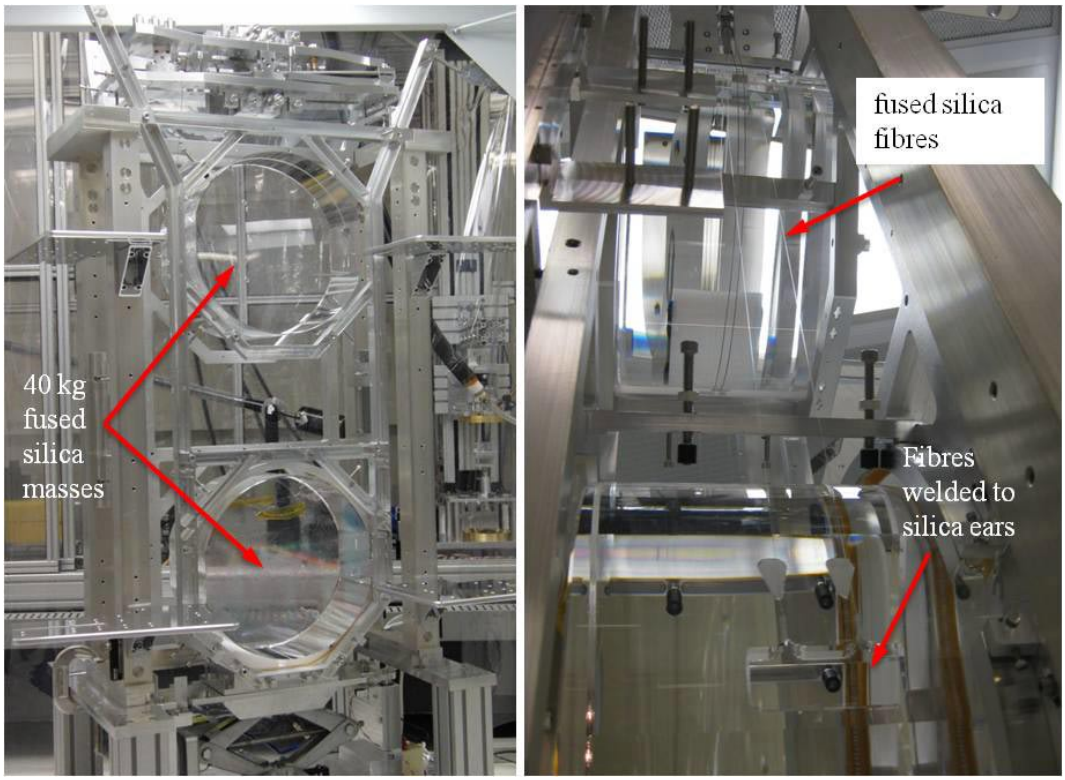

Figure 6.1 Quasi monolithic fused silica suspension of the aLIGO detector installed in MIT, USA. (Image courtesy - MIT, USA) [134]. The fused silica penultimate mass suspends from the upper mass using a steel wire in a loop. The final stage fused silica test mass suspends from the penultimate mass using 4 fused silica fibres of length 602 mm and diameter 400 µm.

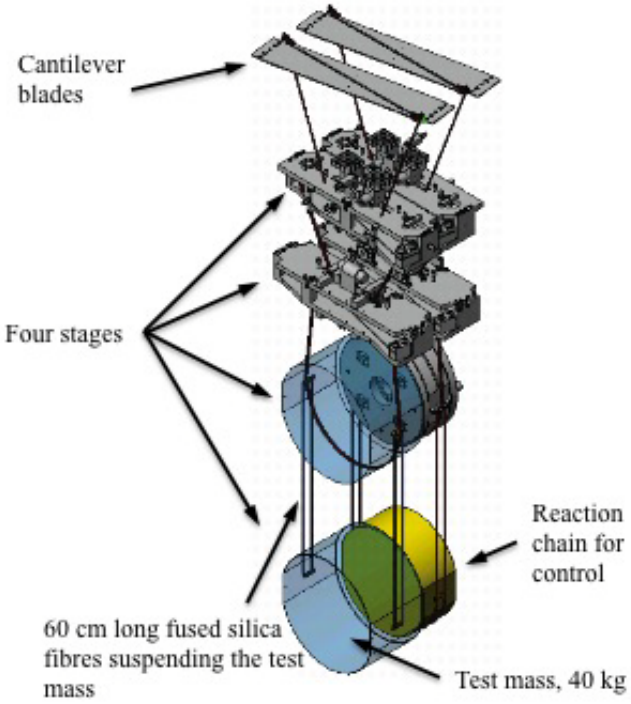

Figure 6.2 Schematic of the quadruple pendulum design of the aLIGO suspension. There are two upper masses suspended from cantilever springs, followed by the lower stage of the suspension (CAD diagram, courtesy - R Jones).

The silica fibres are fabricated from a 100 W CO_2 laser pulling machine [132], which is described in chapter 3.

6.2.1 Suspension fibre design

The fused silica suspension fibres used in aLIGO were originally designed by considering the resonant mode frequencies such as the pendulum mode, pitch/tilt modes, bounce mode and the fundamental violin mode [135]. The design specification required the pendulum mode to be around 0.64 Hz and vertical bounce mode to be below 12 Hz. The fundamental violin mode frequency was kept at 500 Hz. Based on the above parameters each fibre was designed to be 600 mm long and 400 micron in diameter at the thinnest section. The fibres on the same side of the mass are separated by 30 mm. Figure 6.3 shows a schematic of the fibre used in the aLIGO suspension. The fibres were fabricated from 3 mm in diameter fused silica rods. The 3 mm rod, also called the stock, is 10 mm long. The stock is used for holding the fibre during laser welding. The stock tapers down to 800 μm in

diameter, in order to provide thermoelastic cancellation, discussed in chapter 2. The diameter of the thermoelastic noise cancellation region is based on the static stress applied on each fibre (800 MPa). The 800 μm section further tapers down to the thinnest 400 μm section, which is approximately 60.2 cm long. The length of the taper varies from 7 mm to 10 mm [136].

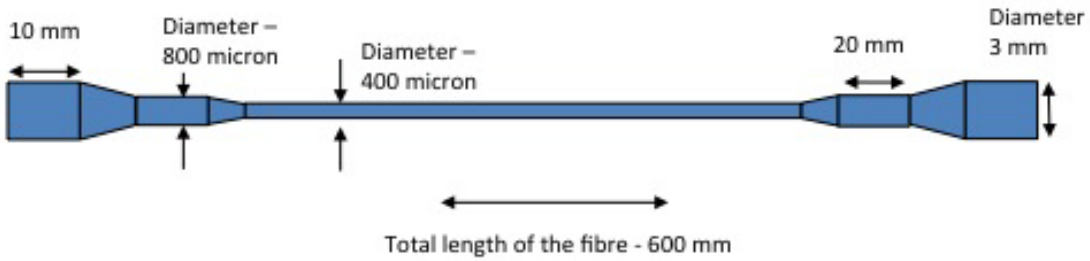

Figure 6.3 Schematic of the fused silica fibre design used for the aLIGO baseline suspension.

6.3 Incremental upgrades to the aLIGO suspension

The incremental upgrade to the aLIGO suspension is focused on two aspects. The first is to lower the total mechanical loss and the second is to improve the suspension thermal noise. The latter can be achieved by increasing the dissipation dilution factor and by further optimising the fibre geometry, which is discussed in the section ahead.

6.3.1 Increasing the dilution factor

The discussion on dissipation dilution factor has been dealt with in chapter 2. The dilution factor can be defined for a fibre of diameter, d, and cross sectional moment of inertia, I, as, $D = 2L\sqrt{\frac{mg}{YI}}$, where L is the length of the suspension, m is the suspended mass and g is the acceleration due to gravity. This equation is for an ideal case (theoretical) where one end of the fibre is assumed to have an infinite stiffness. The theoretical dissipation dilution factor for the aLIGO fused silica suspension (for a uniform cross section fibre) is estimated to be 312. However using FEA techniques, the tapered fibre gives a value of 91, as in a real situation the fibres are not

constrained to infinite stiffness. Hence FEA modelling is useful for predicting realistic values. The dissipation dilution factor is a function of length of the suspension. Hence by increasing the length by a factor of 2, the thermal displacement noise will be improved by a factor of $\sqrt{2}$. The height of the vacuum tank that will enclose the 60 cm long aLIGO suspension system has an additional vertical space to accommodate a suspension up to 100 cm long. Hence the design study undertaken for the incremental upgrade of the suspension, assumed the suspension length to be increased to 100 cm. Also a comparison study between the performance of 3 mm diameter silica stock vs. 5 mm diameter silica stock has been performed. Currently the silica fibres are pulled from a 3 mm thick stock material. However if a 5 mm thick stock material is used for fabricating the silica fibres then studies show that the dissipation dilution can be further improved. A thicker stock will be stiffer and will bend less and hence store less amount of strain energy. This will also decrease the loss occurring in the weld region of the stock. However having a long neck region is not desirable and an optimum neck length is vital for proper distribution of strain energy in the system. A stiffer stock with a longer neck will cancel one another out, resulting in no gain in the dilution factor.

An ideal fibre suspending a mass should store most of the bending energy in the neck region where the thermoelastic noise is not nulled. Studies show that the stock region of the fibre should not contain more than 20% of total energy as this would result in excessive weld loss. The rest of the fibre should contain almost negligible amount of bending energy. To study the effect of neck length on the distribution of energy in the fibre, a FEA model of single fibre (aLIGO design) suspending a 10 kg mass was built. In the aLIGO suspension, four silica fibres suspend a 40 kg test mass, hence the load on each fibre is 10 kg. The material properties of fused silica used to design the ANSYS model were identical to those discussed in chapter 3. The FEA model had a 3 mm thick stock region which tapers (neck) into a 800 μm thermoelastic cancellation region. The 800 μm section then transitions into 400 μm region. The total length of the fibre in this case was taken to be 60 cm. The neck length in this case was varied between 3 mm and 9 mm. The stock region was constrained for all six degrees of freedom and gravity was applied on the model. The FEA model was solved for static and modal analysis to obtain static displacement values and resonant mode frequencies.

The pendulum mode frequency is of most interest. The distribution of bending energy (strain energy) of the relevant mode was extracted from the ANSYS model. Figure 6.4 shows a plot of strain energy vs. length along the fibre for the pendulum mode frequency. The plot clearly shows that as we go from a shorter to a longer neck the distribution of strain energy along the length of the fibre increases over a wider region, or in other words the bending length increases. A large bending length is not desirable in a suspension from the control point of view. Secondly, the strain energy stored in the stock region increases linearly with the increase in neck length. This again will increase the weld loss and limit the sensitivity of the detector at frequencies around 10 Hz. Hence an optimum length of the neck needs to be considered which can be fabricated and is reproducible. In this case it can be between 3 mm to 7 mm, based on the ratios of energy in the neck and weld region.

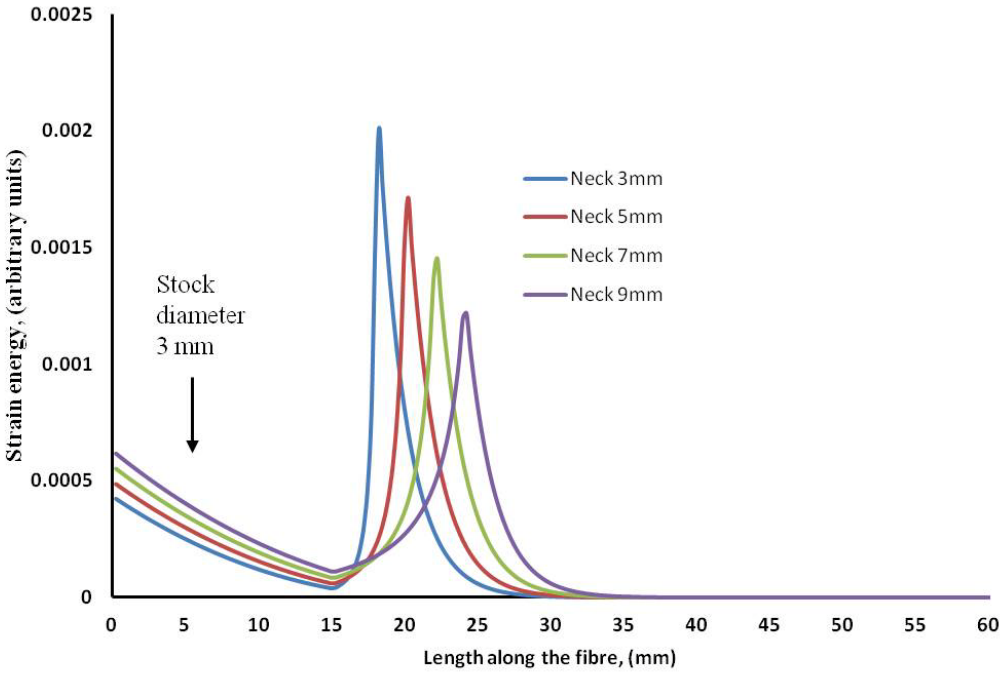

Figure 6.4 A comparison study of strain energy distribution along the fibre for various neck lengths. The stock diamter and stock length are constant in these models, while theneck length is vaired from 3mm to 9 mm. The total length of the fibre is 600 mm. This data is for the pendulum mode.

A second ANSYS model was built to study the effects of stock length on the energy distribution. The stock length was varied from 5 mm to 15 mm. The neck length in this case was kept constant at 5 mm. Figure 6.5 shows the strain energy distribution along the length of the fibre for the second model. The result suggests that the longer stock being softer will bend more than shorter stock. A shorter stock also pushes more energy in the neck region. Studies shows that the mechanical loss of the fibre having shorter stock length is lower than one with relatively longer stock. An optimum length of the stock is often based on the position of the strain energy peak and the distribution of the strain energy in the fibre. Hence a stock length between 5 mm and 10 mm is ideal for incremental upgrade for the aLIGO suspension.

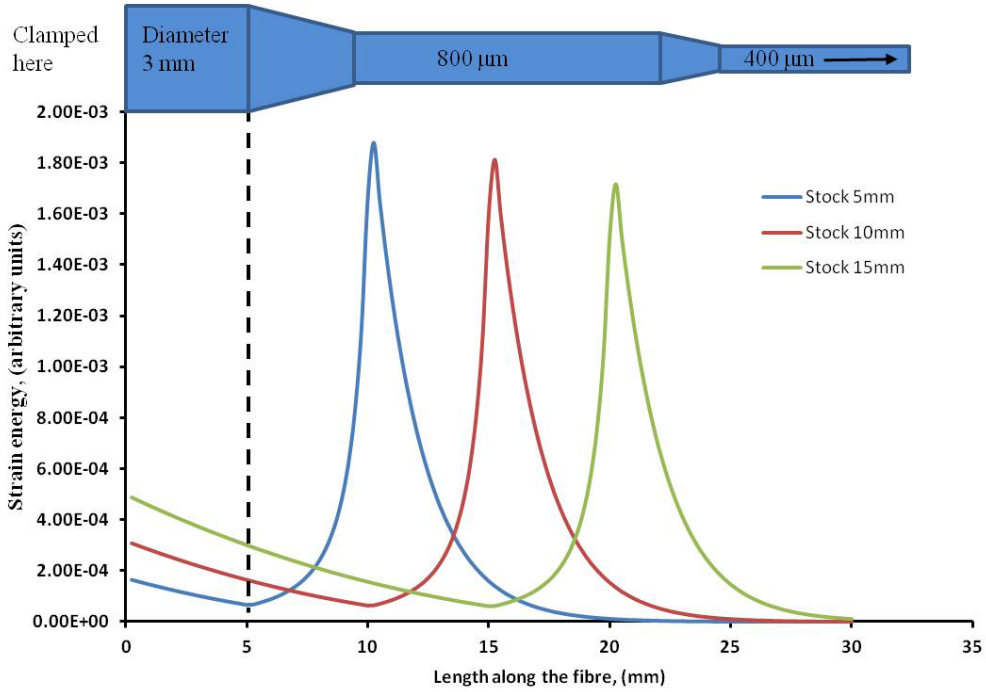

Figure 6.5 Strain energy along the fibre for various stock lengths (varied from 5 mm to 15 mm) and constant neck length of 5 mm. The stock diameter is 3 mm for all cases. This data is for the pendulum mode.

The first and the second FEA models give an optimum neck and stock length which can be used for the design study of the incremental upgrades for the aLIGO suspension system. Hence a third FEA model was built for this purpose. However the total length of the fibre in this case was increased to 100 cm (from 60 cm in the previous cases) and a comparative study between 3 mm/5 mm stock diameter was performed. The stock length was

kept constant at 5 mm. The neck in the model having 3mm/5 mm diameter stock was compared for two lengths - 2 mm and 7 mm. The suspended mass and other cross sections in the fibre remain unchanged. Figure 6.6 shows the energy distribution along the length of the fibre for the third ANSYS model. The optimum designs from this plot are the 3 mm and 5 mm diameter stock with 2 mm neck length (having green and purple legends respectively). These two designs haver a shorter bending length. The strain energy in these two models peaks at the neck region and the stock contains less than 10% of the total energy. In fact the 5 mm thick stock with 2 mm neck has the maximum stiffness among all the cases and thus the highest dilution.

The aLIGO baseline design has a stock length of 11 mm to compromise between the energy stored in the stock and the ease of holding the stock for laser welding. However with the development of suitable tooling the stock length could to reduced to 5 mm from the currently used 11 mm. This will help to improve the dissipation dilution factor and improve the total diluted mechanical loss. Based on the third ANSYS model the most optimum design was selected to estimate the mechanical loss as a function of frequency which is discussed in the next section.

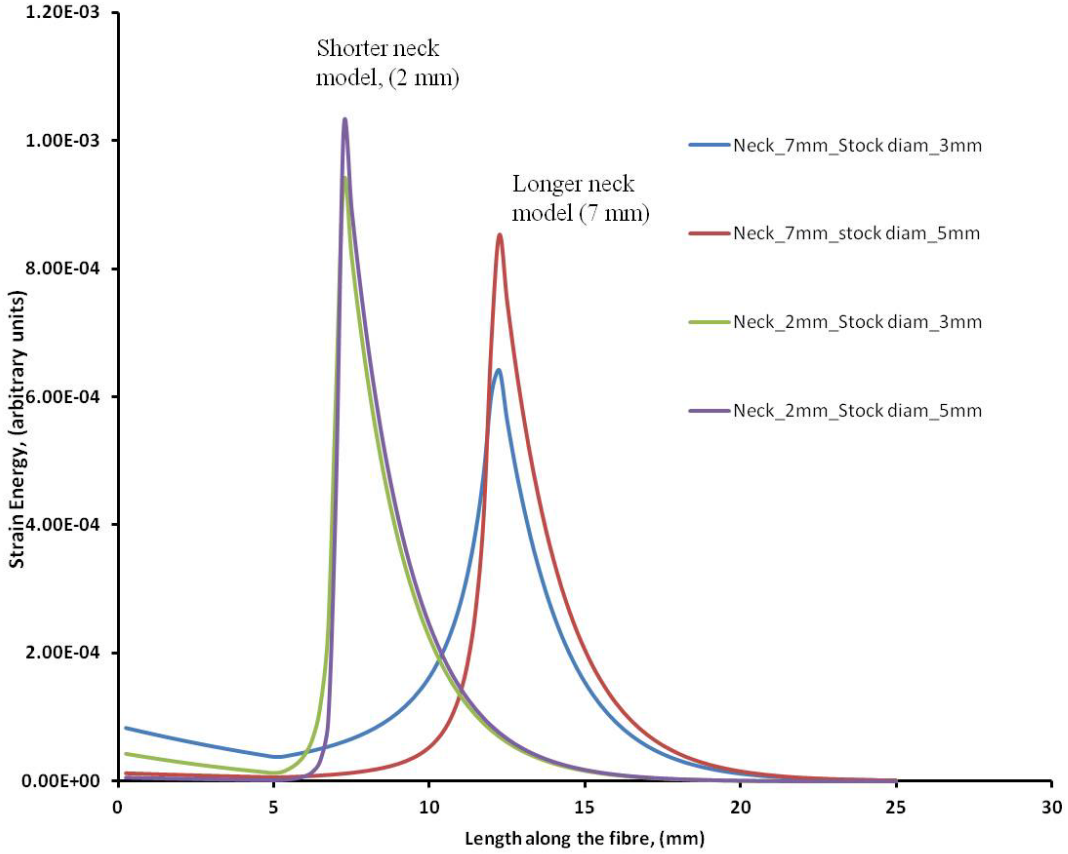

Figure 6.6 A comparison study of strain energy distribution along the fibre, for the pendulum mode frequency of a 100 cm long suspension. The neck length is varied from 2 mm to 7 mm and the stock diameter from 3 mm to 5 mm. The stock length is 5 mm for all the cases.

6.4 Mechanical loss and thermal noise

The prediction from the ANSYS model was used to compare two scenarios with the aLIGO baseline design. In option 1, the suspension had 3 mm diameter stock, 5 mm long stock, 2 mm neck long neck and 100 cm long fibres. In option 2, the suspension had 5 mm diameter stock, 5 mm long stock, 2 mm neck long neck and 100 cm long fibres. The aLIGO baseline design has 3 mm diameter stock, 11 mm long stock, 7 mm long neck and 62.30 cm long suspension fibre [134].

The dissipation dilution factor estimated from the FEA model for all the three options are 159/170/91 respectively. Option 1 and 2 when compared

with the aLIGO design, shows that using a longer fibre and optimising the stock/neck design helps to improve the dissipation dilution factor. Figure 6.7 shows the predicted mechanical loss as a function of frequency for all the three cases. The energy that leaks into the neck of the fibre and the non-zero thermoelastic cancellation due to larger diameter of the stock (>800 micron) results in low frequency peaks. The aLIGO baseline design peaks at 0.25 Hz. The thermoelastic peak for option 1 and option 2 can be seen at approximately 0.5 Hz and 0.9 Hz respectively. The magnitude of thermoelastic peak for option 1 and 2 is lower as compared to the aLIGO design due to less energy in the stock region. At frequencies greater than 20 Hz the mechanical loss flattens and is dominated by the surface and weld loss terms. The improved dilution and optimised fibre geometry leads to a reduction in the mechanical loss by 3.4/6.8 for option 1 and option 2 over the aLIGO baseline design at 10 Hz [137].

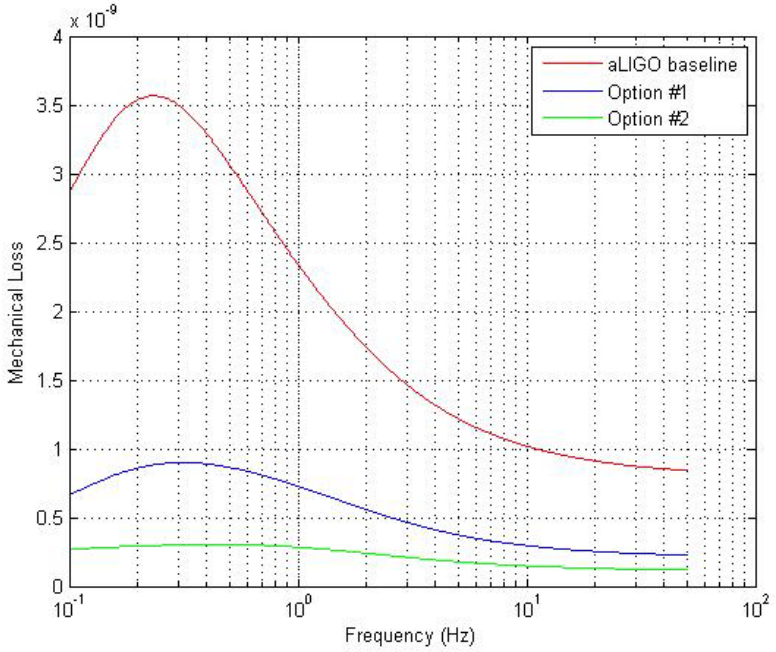

Figure 6.7 A comparison study of the total diluted mechanical loss as a function of frequency for the aLIGO baseline design and two incremental upgrades.

Figure 6.8 shows the thermal displacement noise for all the three cases estimated using equation (2.10), as discussed in chapter 2. At 10 Hz, option 1 and option 2 offers a factor of 2.5 to 3.7 improvement in thermal noise over the aLIGO [137] baseline. Based on the calculation made for these

incremental upgrades, the strain sensitivity is expected to improve by a factor of 2.5 for option 1. This could lead to a factor 15 increase in the event rate.

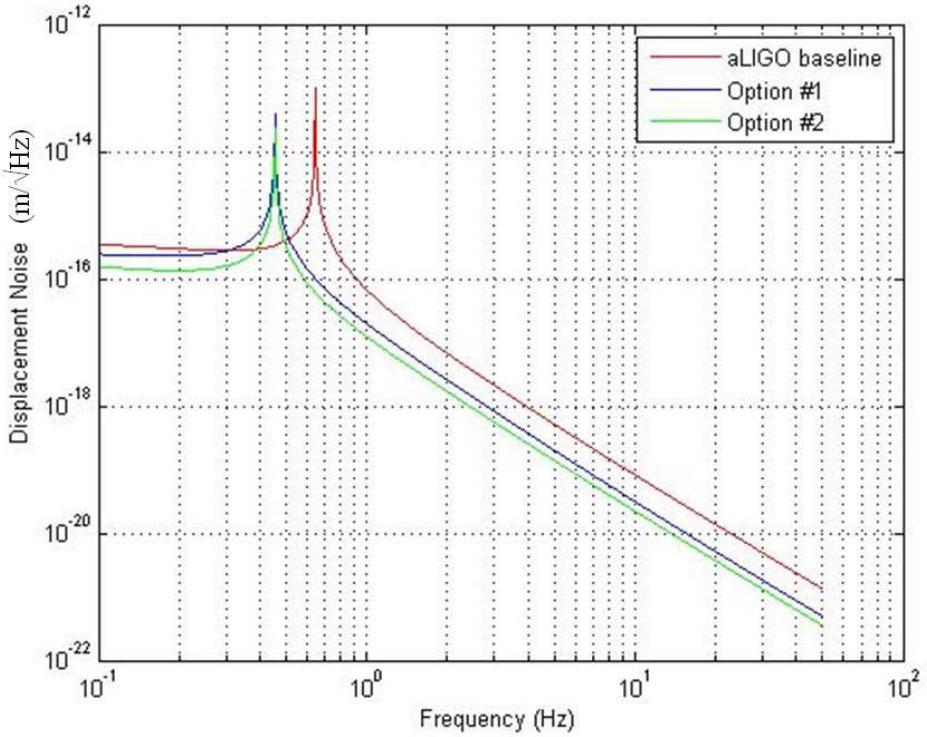

Figure 6.8 Thermal displacement noise as a function of frequency for aLIGO design, which is compared with the two incremental upgrade options.

6.5 Conclusions

There is a significant effort being made around the world to upgrade the status of the current network of gravitational wave detectors. Once online, the second generation of detectors will have improved sensitivity and sky coverage which could lead to the first detection of the gravitational wave signals from various astrophysical sources.

However there are still some scopes for incremental upgrades, which can be applied to these detectors, without making major changes to their existing infrastructure. The possibility of room temperature incremental upgrades, which can be applied to the aLIGO detector to further enhance the sensitivity has been discussed in this chapter. Using the techniques

developed in FEA, various models were analysed to improve the dissipation dilution factor of the pendulum. One suggested way is to increase the length of the current suspension from 60 cm to 100 cm. To improve the low frequency thermal noise, the energy in the suspension fibre needs to be carefully distributed. A comparison study between various neck length, stock length and stock diameter was undertaken. Longer neck and stock increases the bending length of the suspension and therefore should be avoided. A study of larger diameter stock (5 mm) showed an improvement in the dissipation dilution factor by a factor of 1.8, from the current values.

Based on the results from FEA, two models were further studied for their mechanical loss and thermal noise performance. These models have 3 mm and 5 mm diameter stock (stock length 5 mm) and a 2 mm neck. The improved dilution and optimised fibre geometry leads to a reduction in the mechanical loss by a factor of 3.4 and 6.8. At 10 Hz, which is the working frequency of the aLIGO detector. The thermal displacement noise showed an improvement by a factor of 2.5 to 3.7 for the two cases respectively. These incremental upgrades could lead to an improvement of the strain sensitivity by a factor of 2.5, which would increase the sky coverage and the event rate of the detector.

Chapter 7 Conclusions

A network of gravitational wave detectors currently exists around the world to detect the gravitational wave signal from various astrophysical sources. The science runs conducted by the first generation of detectors have placed upper limits on a variety of astrophysical sources after reaching their design sensitivity. The 1st generation of detectors is currently offline and efforts are ongoing to upgrade them to form the 2nd generation of detectors by employing new materials and technologies. The strain sensitivity of the 2nd generation of detectors is expected to improve by a factor of 10, which would increase the range of the detector by a factor of 1000. Once online by 2015-16, these detectors may lead to first detection of gravitational wave signals, and may open new avenues in the field of astronomy and astrophysics. However, continued research and development is required to develop the 3rd generation of detectors for precision gravitational wave astronomy, targeting sources at a range of frequencies. The future detectors could offer detailed measurements of the sources and their physical parameters.

The sensitivity of the current detectors is limited by various noise sources. At low frequency seismic and gravity gradient noise dominates and at lower to higher frequencies the detectors are limited by quantum noise. However in the mid frequency range ($\approx 100\,\mathrm{Hz}$), the coating thermal noise is one of the most dominant noise sources.

Suspension thermal noise results from the random vibrations of atoms in the test mass mirrors and suspension fibres affecting the sensitivity of the detector at frequencies $< 10\,\mathrm{Hz}$. Using the fluctuation dissipation theorem the thermal noise levels in the system can be predicted as well as reduced by adopting the relevant design changes. The mirrors in the detectors are in the form of multiple pendulums; thereby providing a low frequency seismic noise

isolation and most importantly reducing the thermal noise via the use of monolithic final stages of fused silica. A pendulum stores most of the energy in the lossless gravity. The loss mainly comes from the wires storing some amount of energy, which can be diluted by using the dissipation dilution factor. The thermal noise is dependent upon the quality factor (Q, inverse of the mechanical loss) of the pendulum design. The mechanical loss consists of various terms including thermoelastic loss, surface loss, bulk loss and weld loss. Hence the pendulum suspensions used in the detectors have to be carefully designed using ultra low loss materials like fused silica for reducing the diluted mechanical loss value.

GEO 600 is part of the international network of gravitational wave detectors, and a test bed for providing new technologies for future detectors. The GEO detector is currently undergoing an upgrade to GEO-HF, improving the sensitivity in the kilohertz region. Some of the improvements include light squeezing techniques and a DC read-out (Homodyne detection scheme) system. There is a possibility that the planned upgrade could damage the fibres of the GEO monolithic suspension as some of the vacuum tanks need to be opened. A robust procedure for repairing the suspension has been envisaged and the work has been presented in this thesis. An additional opportunity also exists to re-optimise the GEO suspension design, utilising the techniques gained from aLIGO. The repair scenario incorporates a new fused silica suspension fibre with optimised geometry and thermoelastic noise cancellation properties. These fibres will be fabricated using the CO_2 laser-pulling machine in Glasgow, giving high reproducibility and strength to the fibres. These fibres will also give better control to the suspension mirrors, reduced mode frequency coupling and a violin mode spread of less than 1 Hz, due to their optimised geometry. The design of the optimised fibre was achieved through extensive FEA modelling to study the distribution of elastic energy in the silica fibres and the dissipation dilution factor.

A study of mechanical loss of the optimised fibre design has been undertaken and the results have been compared with the original GEO fibre. The original GEO fibre has a thermoelastic peak at ~40 Hz, while the optimsed fibre peaks at less than 1 Hz. This is due to the inclusion of a 300 μm thermoelastic noise cancellation region in the optimised fibre. The total diluted mechanical loss of the optimised fibre shows an improvement over

the original GEO fibre by a factor of 4. The suspension thermal noise when predicted using the mechanical loss value, shows that the optimised fibre performs better than the original fibre by a factor of ~2.

The repair scenario of the GEO monolithic suspension requires the development of tooling and welding procedure. A scaled down version of aLIGO tools were used for this purpose. The strength test results of the fused silica fibres showed a breaking stress of 4.08±0.05 GPa. The stress in each fibre in a suspension would be around 800 MPa, hence providing a factor of safety of 5. Three prototype suspension test hangs using metal masses were performed and later a fused silica monolithic suspension was fabricated in Glasgow. This work has provided a robust repair scenario where the downtime of the GEO detector would be reduced. This will enable the GEO detector to conduct further science runs, especially at a time when other detectors are currently offline for upgrade work.

The monolithic fused silica suspensions used in aLIGO are fabricated using fused silica fibres welded to silica ears using a 100 W CO_2 laser. Laser welding causes high thermal gradients in the silica fibres and ears due to a non-uniform temperature distribution. Once the sample returns to room temperature, the refractive index of the sample changes permanently, and anisotropy or birefringence is observed. This condition leads to the development of residual thermal stress in fused silica. Using the techniques of photoelasticity, the birefringence in the sample can be observed and characterised. The study of photoelasticity requires the production and use of the three forms of polarised light: plane, circularly and elliptically polarised light. The stress in the material can be observed using a plane polariscope set-up. The isoclinic and isochromatic patterns observed under a plane polariscope have been discussed. A circular polariscope can be constructed by using two quarter wave plates along with two crossed polarisers. The relative stress in the sample can be measured in a circular polariscope set-up using the Tardy method of compensation and the stress optic law. Similarly, a Babinet-Soleil Compensator, which is a continuously variable retarder, was used in a plane polariscope set-up to measure the retardation in the sample.

To test the performance of the photoelastic birefringence setup, temporary birefringence was introduced in fused silica by applying a known mechanical

load. The fused silica sample used had a planar geometry and a thickness of 1 mm, hence the stresses were 2-dimensional in nature. The mechanical load was applied on the fused silica sample for two set-ups: firstly as a loaded cantilever and secondly by applying an axial tension. The experimental results were compared with the theoretical predictions and they agreed within 10% of difference. Hence more complicated cases like the study of thermal stress in fused silica samples were undertaken. A 25 W CO_2 laser beam was used to heat the fused silica sample for 10 seconds. The relative stress measured at different positions varied from 3±0.02 MPa to 20±0.41 MPa. In the region where the laser beam was applied, a uniform stress of 4 MPa was measured in the 2 mm radius. However just outside the 2 mm radius, the stress increased by a factor of ~5 (20±0.41 MPa), before declining to 2~3±0.02 MPa. The experimental results were compared with the thermal modelling performed using FEA. A 25 W Gaussian beam was applied as a heat flux on the FEA model of fused silica slide. The model was solved for transient thermal analysis to obtain the temperature distribution and temperature gradients. The results from the thermal analysis were used to solve a transient structural analysis to estimate the resulting thermal stress. The experimental results agreed within 10% when compared against the predicted equivalent stress (FEA) at a radial distance $> 2.5mm$ from the centre. The 1st principal stress (FEA) agreed within 5 %, when compared with the experimental values in the central region where no flow was modelled.

Further, two fused silica slides were welded together using a CO_2 laser beam, for measuring the resulting stress in the weld region. The stress in the 5 mm long weld region was measured to be 3±0.02 MPa. However, outside the weld region the relative stress increases by a factor of ~5. Accurate prediction of thermal stress in the weld region requires computer intensive fluid dynamics modelling, which includes the changing viscosity of the sample with rising temperature. The FEA results combined with photoelastic birefringence techniques can be useful for annealing a sample for reducing the residual thermal stress and possibly the associated mechanical loss.

A study of suspension thermal noise in the aLIGO detector for applying incremental room temperature upgrades has been presented in this thesis.

The incremental upgrades could be achieved through improving the dilution factor and by further reducing the diluted mechanical loss value. Using the FEA model, a study of elastic energy distribution in the stock and neck region of the fibre was undertaken. FEA results predicted that by using a stock of diameter 5 mm, neck of length 2 mm, while increasing the pendulum length to 100 cm, improves the dissipation dilution by a factor of 1.8, over the current aLIGO baseline design. In this case the diluted mechanical loss reduces by a factor of 3.4~6.8. The thermal displacement noise showed a gain of 2.5~3.7 times over the baseline design. Based on the proposed improvements, the sensitivity of the detector is expected to further gain by a factor of 2.5~3.7.

Various aspects of suspension design have been presented in this thesis. Methods to reduce the mechanical loss and improve the suspension thermal noise have been discussed. The techniques shown in the experimental photoelasticity chapter are generic in nature and can be adopted for studying various other aspects of the suspension design technology. A novel approach of modelling and measuring the thermal stress can be useful for the study of future detectors. These techniques can be utilised to measure stress in the suspensions used in cryogenic detector. This could also motivate the search for a correlation between thermal stress and weld loss for reducing the total mechanical loss and improving the suspension thermal noise.

With the increasing sensitivity and optimised designs the international network of gravitational wave detectors are continuously expanding their range. The first detection of gravitational wave signals looks to be possible in the near future. Distant sources could be within the reach of future detectors thus adding to the understanding of our Universe.

Bibliography

1. Einstein, A., *Die grundlage der algemeinen relativitatstheorie.* Annalen der Physik, 1916. **49**: p. 769.

2. Einstein, A. and N. Rosen, *On gravitational waves.* Journal of the Franklin Institute, 1937. **233**.

3. Weber, J., *Evidence for discovery of gravitational radiation.* Physical Review Letters, 1969. **22**: p. 1320.

4. Weber, J., *Anisotropy and polarization in the gravitational-radiation experiments.* Physical Review Letters, 1970. **25**: p. 180.

5. Pallottino, G.V. *The resonant mass detectors of the Rome group*. in *Eds. E Coccia G Veneziano and G Pizzella Gravitational Waves, Second Edoardo Amaldi Conference held in CERN*. 1998. Switzerland: World Scientific press.

6. Prodi, G.A. *Initial operation of the gravitational wave detector Auriga*. in *Eds. E Coccia, and G Veneziano and G Pizzella Second Edoardo Amaldi Conference held in CERN*. 1998. Switzerland: Edoardo Amaldi Foundation Series.

7. Hulse, R., *The discovery of the binary pulsar.* Reviews of Modern Physics, 1994. **66**: p. 699.

8. Taylor, J., *Binary pulsars and relativistic gravity.* Reviews of Modern Physics, 1994. **66**: p. 711.

9. Will, C.M., *Theory and experiment in gravitational physics*. 1993: Cambridge University Press Cambridge UK.

10. Saulson, P., *Fundamentals of interferometric gravitational wave detection*. 1994: World Scientific Singapore

11. Sathyaprakash, B.S. and B.F. Schutz, *Physics, Astrophysics and Cosmology with Gravitational Waves.* Living Reviews in Relativity, 2009. **12**.

12. Heptonstall, A., *Characterization of mechanical loss in fused ribbons for use in gravitational wave detector suspensions*, in *Department of Physics and Astronomy*. 2004, University of Glasgow.

13. Schutz, B. *The detection of gravitational waves*. in *Eds. J A Marck and J P Lasota in Proceedings of the Les Houches School on Astrophysical Sources of Gravitational Radiation*. 1996. Springer Berlin.

14. Abbott, B., et al., *Search for gravitational-wave bursts in LIGO data from the fourth science run.* Classical and Quantum Gravity, 2007. **24**: p. 5343.

15. Hough, J. and S. Rowan, *The search for gravitational waves.* Journal of Physics B: Atomic and Molecular Physics 2005. **38**: p. S497.

16. Abadie, J., et al., *Search for gravitational waves from binary black hole inspiral, merger and ringdown.* Phyiscal Review D, 2011. **83-122005**.

17. Abramovici, A., et al., *Gravitational Wave Astrophysics* in *Eds. E W Kolb and R Peccei in Proceedings of the 1994 Snowmass Summer Study on Particle and Nuclear Astrophysics and Cosmology*. 1994, Word Scientific Singapore: Colorado. p. 398.

18. Pitkin, M., et al., *Beating the spin-down limit on gravitational wave emission from the Crab Pulsar*. arXiv:0805.4758v2 [astro-ph], 2008.

19. Allen, B. and J.D. Romano, *Detecting a stochastic background of gravitational radiation: Signal processing strategies and sensitivities.* Phyiscal Review D, 1999. **59-102001**.

20. Hough, J. and H. Walther, *Proposal for a joint German-British Interferometric gravitational wave detector*, in *Max-Planck-Institut fur Quantenoptik Report 147 and GWD/137/JH(89)*. 1989.

21. Abbott, B., et al., *Searching for a stochastic background of Gravitational waves with LIGO.* The Astrophysical Journal 2007. **659**: p. 918.

22. Forward, R.L. and D. Zipoy, *Upper limit for interstellar millicycle gravitational radiation.* Nature, 1961. **189**: p. 473.

23. Gottardi, L., A.d. Waard, and O. Usenko, *Sensitivity of the spherical gravitational wave detector MiniGRAIL operating at 5K.* Physical Review Letters D, 2007. **76**(10).

24. Aguiar, O.D., L.A. Andrade, and J.J. Barroso, *The Brazilian gravitational wave detector Mario Schenberg: status report.* Classical and Quantum Gravity, 2006. **23**(239).

25. Forward, R.L., *Wideband laser-interferometer graviational-radiation experiment.* Physical Review D, 1978. **17**: p. 379.

26. Weiss, R., *Electromagetically coupled broadband gravitational antenna quarterly progress report*. 1972, Research Laboratory of Electronics MIT. p. 54.

27. Drever, R.W.P. and G. Ford. *Gravity-wave detector using optical cavity sensing in general relativity and gravitation*. in *Ed. E Schmutzer in proceedings of the 9th International Conference on General Relativity and Gravitation*. 1983. Jena Cambridge University Press UK.

28. Meers, B., *Recycling in laser-interferometric gravitational-wave detectors.* Physical Review D, 1988. **38**: p. 2317.

29. Drever, R.W.P., et al. *Gravitational wave detectors using laser interferometers and optical cavities: Ideas, principles and prospects*. in *Proceedings of the NATO Advanced Study Institute*. 1981. Germany: Plenum Press, New York, 1983.

30. Strain, K.A. and B.J. Meers, *Experimental demonstration of dual recycling for interferometric gravitational-wave detectors.* Phys. Rev. Lett., 1991. **66**.

31. Drever, R.W.P., *Interferometric detectors of gravitational radiation*, ed. N.D.a.T. Piran. 1983: North Holland Publishing Elsevier.

32. Matthew, P., et al., *Gravitational Wave Detection by Interferometry (Ground and Space).* Living Rev. Relativity, 2011. **14**(5).

33. Husman, M., et al., *Modeling of multistage pendulums: triple pendulum suspension for GEO 600.* Review of Scientic Instruments, 2000. **71(6)**: p. 2546.

34. Hughes, S. and K. Thorne, *Seismic gravity-gradient noise in interferometric gravitational-wave detectors.* Physical Review D, 1998. **58**: p. 122002.

35. Beker, M.G., et al., *Improving the sensitivity of future GW observatories in the 1–10 Hz band: Newtonian and seismic noise.* Gen. Relativ. Gravit., 2011. **43-623–656**.

36. Saulson, P., *Thermal noise in mechanical experiments.* Physical Review D, 1990. **42**: p. 2437.

37. Levin, Y., *Internal thermal noise in the LIGO test masses: A direct approach.* phyiscal Review D, 1998. **57**(659–663).

38. Harry, G., et al., *Thermal noise in interferometric gravitational wave detectors due to dielectric optical coatings.* Class. Quantum Grav., 2002. **65-897-917**.

39. Martin, I.W., et al., *Measurements of a low-temperature mechanical dissipation peak in a single layer of Ta2O5 doped with TiO2.* Class. Quantum Grav., 2008. **25**(055005).

40. Rowan, S., et al. *The design of low loss suspensions for advanced gravitational wave detectors*. in *Second Edoardo Amaldi Conference on Gravitational Waves*. 1998. Switzerland: World Scientific, Singapore.

41. Hough, J. and H.Walther, *Proposal for a Joint German-British interferometric gravitational wave detector*. 1989, Max-Planck-Institut fur Quantenoptik Report 147 and GWD/137/JH(89).

42. Edelstein, W.A., et al., *Limits to the measurement of displacement in an interferometric gravitational radiation detector.* J. Phys. E: Sci. Instrum., 1978. **11**(7): p. 710-711.

43. Loudon, R., *Quantum limit on the Michelson interferometer used for gravitational-wave detection.* Phys. Rev. Lett., 1981. **47**: p. 815-818.

44. Harry, G., et al., *Advanced LIGO: the next generation of gravitational wave detectors.* Class. Quantum Grav., 2010. **27**(084006).

45. Abbot, B., et al., *LIGO: the Laser Interferometer Gravitational-Wave Observatory.* Rep. Prog. Phys., 2009. **72, 076901**.

46. Lazzarini, A. and R. Weiss, *LIGO Science Requirements Document (SRD)*. 2008, California Institute of Technology, Pasadena, CA.

47. Rowan, S. and J. Hough. *Gravitational wave detection by interferometry (ground and space).* 2000; Available from: http://www.livingreviews.org/lrr-2000-3

48. Robertson, N., et al., *Advanced LIGO suspension system conceptual design.* Private communication LIGO DCC, 2005. **T010103-04-D**: p. 1.

49. Collaboration, G.M.H.a.t.L.S., *The next generation of gravitational wave detectors.* Classical and Quantum Gravity, 2010. **27**(8).

50. Abadie, J. and B.P. Abbott, *Predictions for the Rates of Compact Binary Coalescences Observable by Ground-based Gravitational-wave Detectors.* Classical and Quantum Gravity, 2010. **27**.

51. Kopparapu, R.K., et al., *Host Galaxies Catalog Used in LIGO Searches for Compact Binary Coalescence Events.* Astrophys. J., 2008. **675.** : p. 1459-1467.

52. Lobo, J.A. *Sources of gravitational waves*. in *Eds. G S Hall J R Pulhamin General Relativity: Proceedings of the Forty Sixth Scottish Universities Summer School in Physics* 1996. Aberdeen: CRC Press

53. Plissi, M., et al., *GEO 600 triple pendulum suspension system: seismic isolation and control.* Review of Scientic Instruments, 2000. **71**: p. 2539.

54. Torrie, C., *Development of suspensions for the GEO 600 gravitational wave detector*, in *Department of Physics and Astronomy*. 2000, University of Glasgow.

55. Gossler, S., et al., *The mode cleaner system and suspension aspects of GEO 600.* Classical and Quantum Gravity, 2002. **19** p. 1835.

56. Hough, J., et al. *GEO 600: Current status and some aspects of the design*. in *Eds. K TSubono M KFujimoto and K Kuroda TAMA International Workshop on Gravitational Wave detection* 1997. Japan: Universal Academy Press Inc Tokyo.

57. Gossler, S. and G. Cagnoli, *Damping and tuning of the fibre violin modes in monolithic silica suspension.* Classical and Quantum Gravity, 2004. **21** p. 923.

58. Khalaidovski., A., et al., *Status of the GEO 600 squeezed-light laser.* Journal of Physics: Conference Series, 2012. **363**(012013).

59. Acernese, F., et al., *Status of Virgo detector.* Class. Quantum Grav., 2007. **24**: p. S381–S388.

60. Acernese, F., et al., *Results of the Virgo central interferometer commissioning.* Classical and Quantum Gravity, 2004. **21**: p. S395.

61. Acernese, F., et al., *Search for gravitational waves associated with GRB 050915a using the Virgo detector.* Class. Quantum Grav., 2008. **25**(225001).

62. Kuroda, K., et al., *Status of LCGT.* Class. Quantum Grav., 2010. **27**(084004).

63. Ohashi, M., et al., *Status of LCGT and CLIO.* J. Phys.: Conf. Ser., 2008. **120**(032008).

64. Takahashi, R., et al., *Status of TAMA300.* Classical and Quantum Gravity, 2004. **21**: p. S403.

65. Danzman, K. *Gravitational wave observatory in heliocentric orbit* in *Eds K Tsubono M-K Fujimoto K Kuroda in Proceedings of the TAMA*

International Workshop on Gravitational Wave Detection. 1997. Japan: Universal Academy Press Inc. Tokyo.

66. Danzman, K., 2, and 3, *Laser Interferometer Space Antenna for Gravitational Wave Measurements.* Class. Quantum Grav., 1996. **13**: p. A247–A250.

67. Brown, R., *A brief account of microscopical observations made in the months of June, July and August, 1827, on the particles contained in the pollen of plants; and on the general existence of active molecules in organic and inorganic bodies.* Edinburgh New Philosophical Journal, 1828: p. 358.

68. Einstein, A., *Über die von der molekularkinetischen theorie der wärme geforderte bewegung von in ruhenden flüssigkeiten suspendierten teilchen.* Annalen der Physik, 1956. **322**: p. 549.

69. Callen, H.B., et al., *Irreversibility and generalized noise.* Physical Review B, 1951. **83**: p. 34.

70. Callen, H.B. and R.F. Greene., *On a Theorem of Irreversible Thermodynamics.* Physical Review, 1952. **86:**: p. 702-710.

71. Rowan, S., et al., *Thermal noise and material issues for gravitational wave detectors.* Physics Letters A, 2005. **347**: p. 25.

72. Twyford, S., *Development Towards Low Loss Suspensions for Laser Interferoemtric Gravitational Wave Detectors*, in *Physics and Astronomy*. 1998, University of Gasgow: Glasgow.

73. Quinn, T.J., et al., *Stress-dependent damping in Cu-Be torsion and flexure suspensions at stresses up to 1.1 GPa.* Physics Letters A, 1995. **198**(474).

74. Cagnoli, G., et al., *Damping dilution factor for a pendulum in an interferometric gravitational waves detector.* Physics Letters A, 2000. **272**: p. 39.

75. Willems, P. and V.Sannibale, *Investigations of the dynamics and mechanical dissipation of a fused silica suspension.* Physics Letters A, 2002. **297**: p. 37.

76. Zener, C., *Internal friction in solids.* Physical Review, 1937. **52**: p. 230.

77. Nowick, A.S. and B.S. Berry, *Anelastic relaxation in crystalline solids* 1972: Academic press New York and London.

78. Braginsky, V.B., et al., *Thermodynamical fuctuations and photo-thermal shot noise in gravitational wave antennae.* Phys. Lett. A, 1999. **264**.

79. Zener, C., *Elasticity and Anelasticity in Metals.* 1948: University of Chicago Press.

80. Penn, S.D. and A. Ageev, *Frequency and surface dependence of the mechanical loss in fused silica* Physics Letters A 2006. **352**: p. 3.

81. Gretarsson, A., et al., *Pendulum mode thermal noise in advanced interferometers: a comparison of fused silica fibers and ribbons in the presence of surface loss.* Physics letter A, 2000. **270**: p. 108.

82. Cumming, A., et al., *Finite element modelling of the mechanical loss of silica suspension fibres for advanced gravitational wave detectors. .* Class. Quantum Grav., 2009. **26**(215012).

83. Kumar, R., *Finite element analsysis of suspension elements for gravitational wave detectors* in *School of Physics and Astronomy*. 2008, University of Glasgow: Glasgow.

84. Cumming, A., *Aspects of mirrors and suspensions for advanced gravitational wave detectors*, in *Department of Physics and Astronomy*. 2008, University of Glasgow.

85. Logan, J., et al., *Aspects of the thermal motion of a mass suspended as a pendulum by wires.* Physics Letters A, 1993. **183**: p. 145.

86. Gonzalez, G. and P.R. Saulson, *Brownian motion of a mass suspended by an anelastic wire.* Journal of the Acoustical Society of America, 1994. **96**: p. 207.

87. Willke, B., et al., *Status of GEO 600.* Class. Quantum Grav., 2004. **21**: p. S417–S423.

88. Hild, S., *The status of GEO 600.* Class. Quantum Grav., 2006. **23**: p. S643–S651.

89. Willke, B., et al., *Stabilized lasers for advanced gravitational wave detectors.* Class. Quantum Grav., 2008. **25**(114040).

90. Willke, B., *The GEO-HF project.* Classical Quantum Gravity, 2006(23): p. S207–S214.

91. Rowan S, T.S.M., Hough J, Gwo D-H and Route R, *Mechanical losses associated with the technique of hydroxide-catalysis bonding of fused silica.* Phys. Lett. A, 1998. **246**(471-8).

92. Cagnoli, G., et al., *Effects of nonlinear thermoelastic damping in highly stressed fibers.* Physical Review B, 2002. **65** p. 174.

93. Robertson, N.A., *Update on Quadruple Suspension Design for Advanced LIGO.* Classical Quantum Gravity, 2012.

94. Shackleford, J.H. and A. W, *CRC materials science and engineering handbook*. 1999: 3rd ed. CRC Press, USA.

95. Barton, M., *Dissipation dilution.* Private communication LIGO DCC, 2008. **T070101-00**: p. 1.

96. Willke, B., et al., *GEO600: status and plans.* Class. Quantum Grav., 2007. **24**: p. S389–S397.

97. Heptonstall, A., et al., *CO2 laser production of fused silica fibers for use in interferometric gravitational wave detector mirror suspensions.* . Class. Quantum Grav., 2011. **82**(1).

98. Kumar, R., et al., *CO2 laser pulling machine for fabrication of fused silica suspension fibres,* in *LIGO DCC - T100239*. 2010.

99. Cumming, A., et al., *Design and development of the advanced LIGO monolithic fused silica suspension.* Class. Quantum Grav., 2012. **29**(3).

100. Penn, S.D., et al., *High quality factor measured in fused silica.* Review of Scientic Instruments, 2001. **72**(9).

101. Cunningham, L., et al., *Re-evaluation of the mechanical loss factor of hydroxide-catalysis bonds and its significance for the next generation of gravitational wave detectors.* Phys. Lett. A, 2010. **374-39**.

102. Haughian, K.A., *Aspects of materials research for advanced and future generations of gravitational wave detectors.*, in *School of Physics and Astronomy*. 2012, University of Glasgow: Glasgow.

103. Aben, H., *Photoelastic tomography for residual stress measurement in glass.* Optical Engineering, 2005. **44 (9)**.

104. Aben, H., L. Ainola, and J. Anton, *Integrated photoelasticity for nondestructive residual stress measurement in glass.* Optics and Lasers in Engineering, 2000. **33**: p. 49-64.

105. Shurcliff, W.A., *Polarized light*. 1962, London: Harvard University press, Oxford University press.

106. Kuske, A. and G. Robertson, *Photoelastic stress analysis*. 1974, London: John Wiley & Sons.

107. Frocht, M.M., *Photoelasticity* Vol. 1. 1964, New York: John Wiley & Sons, Inc.

108. Dally, J.W. and W.F. Riley, *Experimental stress analysis*. 1965, New York: McGraw-Hill.

109. Hecht, E., *Optics*. 2002: Addison-Wesley.

110. *Thorlabs - LPVISB050 - Ø12.5 mm Unmounted Linear Polarizer, 500 - 720 nm* http://www.thorlabs.com/catalogpages/V21/911.PDF.

111. Glazer, A.M., J.G. Lewis, and W. Kaminsky, *An automatic optical imagine system for birefringent media.* Proceedings The Royal Society, 1996. **452**: p. 2751-2765.

112. Wang, B. and W. Hellman, *Accuracy assessment of a linear birefringence measurement system using a Soleil_babinet compensator.* Review of Scientific Instruments, 2001. **72**(11): p. 4066.

113. Thorlabs, *SBC-VIS Soleil Babinet compensator user guide (6569-D02 Rev. B)*, http://www.thorlabs.com/Thorcat/6500/SBC-VIS-Manual.pdf, Editor. 2012.

114. *Optical retardation measurements with the soleil-babinet compensator*, in *Technical memorandum TM-8101*, Special Optics (http://www.specialoptics.com/).

115. Jessop, H.T., *On the Tardy and Sénarmont methods of measuring fractional relative retardations.* J. Appl. Phys., 1953. **4**: p. 138.

116. Redner, S., *Compensation Method Using Synchronized Polarizer--Analyzer Rotation and its application to the automated polariscope.* Society of Experimental Stress Analysis, 1975. **3**.

117. Sinha, N.K., *Normalised dispersion of birefringence of Quartz and stress optical coefficient of Fused silica and plate Glass.* Physics and Chemistry of Glasses, 1978. **19**(4): p. 69-77.

118. Burger, C.P., *Thermal modeling.* Experimental Mechanics, 1975. **15**(11): p. 430-442.

119. Benham, P.P. and R. Hoyle, *Thermal stress*. 1964, London: Pitman & sons Ltd.

120. White, G.K., *Thermal expansion of reference materials: copper, silica and silicon.* Journal of Physics D, 1973. **6**(17): p. 2070.

121. Shand, E.B., *Engineering glass, modern materials*. Vol. 6, New York: Academeic Press.

122. Spinner, S., *Elastic Moduli of Glasses at Elevated Temperatures by a Dynamic Method.* Journal of the American Ceramic Society, 2006. **39**(3).

123. *Coupled-Field Analysis guide*. 2009, ANSYS, Inc (www.ansys.com).

124. *ANSYS mechanical APDL thermal analysis guide (Volume 13)*. 2010, ANSYS, Inc. (www.ansys.com): Canonsburgh, PA, USA.

125. Chapman, A., *Fundamentals of heat transfer*. 1987, New York: Macmillan publishing company.

126. *Fluids analysis guide*. 2009, ANSYS, Inc (www.ansys.com): Canonsburg, PA (USA).

127. Heptonstall, A., et al., *Characterisation of mechanical loss in synthetic fused silica ribbons.* Physics letters A, 2006. **354**: p. 353-359.

128. Heptonstall, A., et al., *Investigation of mechanical dissipation in CO2 laser-drawn fused silica fibres and welds.* Class. Quantum Grav., 2010. **27**(035013).

129. Harry, G.M., et al., *Advanced LIGO: the next generation of gravitational wave detectors.* Class. Quantum Grav., 2010. **27**(084006).

130. Abbott, B.P., et al., *Predictions for the rates of compact binary coalescences observable by ground-based gravitational-wave detectors* Class. Quantum Grav., 2010. **27-173001**.

131. Plissi, M.V., et al., *Aspects of the suspension system for GEO 600* Rev. Sci. Instrum., 1998. **69-3055**.

132. Heptonstall, A., et al., *Investigation of mechanical dissipation in CO2 laser-drawn fused silica fibres and welds* Class. Quantum Grav., 2010. **27-035013**.

133. Cumming, A.V., *Design and development of the advanced LIGO monolithic fused silica suspension* Class. Quantum Grav., 2012. **29-035003**.

134. Robertson, N., et al., *Update on quadruple suspension design for Advanced LIGO* Class. Quantum Grav., 2012. **29 235004**.

135. Robertson, N., et al., *Quadruple suspension design for Advanced LIGO* Class. Quantum Grav., 2002. **19-4043-58**.

136. Cumming, A.V., et al., *Finite element modelling of the mechanical loss of silica suspension fibres for advanced gravitational wave detectors* Class. Quantum Grav., 2009. **26-215012**.

137. Hammond, G.D., et al., *Reducing the suspension thermal noise of advanced gravitational wave detectors.* Class. Quantum Grav., 2012. **29-124009**.